Agent-based modelling of tumour spheroid growth and treatment

Diploma thesis

Harald Kempf

Frankfurt Institute for Advanced Studies
Institute for Theoretical Physics
Johann-Wolfgang Goethe University
Ruth-Moufang-Str. 1
60438 Frankfurt am Main, Germany

August 29, 2008

Erklärung

Ich versichere hiermit, dass ich die vorliegende Arbeit selbständig verfasst, keine anderen als die angegebenen Hilfsmittel verwendet und sämtliche Stellen, die benutzten Werken im Wortlaut oder dem Sinne nach entnommen sind, mit Quellen– bzw. Herkunftsangaben kenntlich gemacht habe.

Frankfurt am Main, den 29. August 2008

Zusammenfassung

Im Rahmen dieser Diplomarbeit wurde eine, von der individuellen Zelle ausgehende, agentenbasierte Computersimulation des Wachstums eines multizellulären Tumorsphäroiden entwickelt. Die theoretische Behandlung des Tumorwachstums ist von großem Interesse, da ein realistisches Modell dazu dienen kann, Experimente *in silico* zu simulieren. Dies bietet nicht nur zeitliche und finanzielle Vorteile gegenüber der tatsächlichen Durchführung der Experimente, sondern muss auch von einem ethischen Standpunkt aus bevorzugt werden, da Simulationen Laborversuche an Tieren oder klinische Tests an Probanden teilweise ersetzen können.

Die Simulationsumgebung, welche als Teil dieser Diplomarbeit entwickelt wurde, ist in der Programmiersprache C++ erstellt, um durch die verwendung von Objekten und Klassen eine maximale Erweiterbarkeit im Hinblick auf zukünftige Untersuchungen zu gewährleisten. Eine starke experimentelle Anbindung ist durch die gitterfreie, kräftebasierte Interaktion der Zellagenten gegeben. Die Tumordynamik inklusive Zellbewegung, Zellzyklus und Diffusion von Nährstoffen wurde als Multiskalenproblem erfasst.

Um eine realistische Simulation zu erstellen, muss die Zelle als das zu simulierende Objekt zuerst abstrahiert werden. Dabei geht es um die realitätsgetreue Abbildung der biophysikalisch relevanten Eigenschaften einer Zelle auf ein mathematisches Modell. Mechanismen der Zelle, die für eine realistische Erforschung der Onkogenese im Modell entscheident sind, müssen im Modellansatz implementiert werden.

In erster Näherung kann eine Zelle als viskoelastische, adhäsive Kugel betrachtet werden. Folgt man dieser Betrachtungsweise so sind etablierte Interaktionsmodelle wie zum Beispiel das Johnson-Kendall-Roberts Modell anwendbar, um die Wechselwirkung zwischen Zellen realistisch zu beschreiben. Zur Bestimmung der Zellnachbarschaft wurde eine kinetische und dynamische Delaunay-Triangulation verwendet, welche es ermöglicht, auf elegante und effiziente Weise die Nachbarschaftsbeziehungen im Gewebe zu erfassen, sowie durch ihre Dualität zur Voronoi-Zerlegung Zellvolumina und -kontakflächen zu berechnen.

Die aus dem Johson-Kendall-Roberst Modell resultierenden Kräfte der Zellinteraktion wurden in einer überdämpften Näherung integriert, wie sie für Zellen in dichtem Gewebe anwendbar ist. Hierzu wurden numerischen Algorithmen für die Stabilisierung und effizientere Simulation der entstehenden Zelldynamik entwickelt (lokale und globale adaptive Zeitschrittweite).

Die Einführung eines Zellzyklus und der dazugehörigen Mechanismen für die Zellagenten ermöglicht die realistische Simulation des Gewebewachstums. Voraussetzung dafür war, das die Dynamik der Nährstoffe für den Zellmetabolismus erfasst werden konnte. Zur Mod-

ellierung der zugrunde liegenden Reaktions-Diffusionssysteme löslicher Nährstoffe wird der "alternating-direction implicit"-Algorithmus (ADI) angewandt.

Weiterhin wurde ein fortschrittlicher Algorithmus für die Zytokinese in agentenbasierten Simulationen eingeführt, der entscheidende Laufzeitvorteile durch eine realistischere Dynamik der Zellen während der Mitose mit sich bringt. Ein implementiertes Modell für die mechanische Proliferationshemmung infolge eines zu hohen Zelldrucks wurde mit der Wirkung eines nährstoffbasierten Mechanismus verglichen.

Das Wachstum eines multizellulären Tumorsphäroiden konnte im Verlauf der Arbeit auf der Basis von experimentell ermittelten Größen für die Zellagenten *in silico* modelliert werden. Dabei wurde ein Vergleich der erzielten Ergebnisse mit experimentellen Resultaten durchgeführt. Sowohl für das Problem der Zellsortierung aufgrund differentieller Adhäsion als auch für das avaskuläre Tumorwachstum, stimmten die Ergebnisse des Modells mit den experimentellen Resultaten überein.

Erste Simulatioinen der Bestrahlung eines Tumors *in silico* zeigten Effekte wie z.B. die Arretierung am G_2/M-Kontrollpunkt, die qualitativ wie quantitativ mit experimentellen Beobachtungen übereinstimmen. Als Reaktion der Tumordynamik auf partielle Bestrahlung des Gewebes wurden verschiedene Phänomene beobachtet, die für weitere Untersuchungen von Interesse sind. Dazu zählen Effekte wie z.B. die Resynchronisierung des Zellzyklus und ein exzessives Tumorwachstum nach erfolgter Bestrahlung.

Die Übereinstimmung der erzielten Ergebnisse zeigt, dass das entwickelte Modell auf die Simulation von komplexeren Effekten der Tumorbestrahlung mit Schwerionen ausgedehnt werden kann. Eine angestrebte Nutzung ist die Simulation der Bestrahlungsprozesse mit dem Ziel, die verwendeten Protokolle zu optimieren und damit die Effektivität der Strahlentherapie zu erhöhen.

Contents

Motivation:
Cancer and theoretical biology

Cancer is a leading cause of death worldwide. In 2007[1] the disease accounted for 7.9 million deaths which is around 13% of deaths worldwide and up to 25% in the developed countries. The lifetime probability of developing cancer for a person in the United States is as high as 45% for men and 38% for women (for detailed statistics on cancer in the US see *Jemal et al.* (2007)). Even if cancer therapy is started early after the onset of the disease, the statistical survival rate, which depends strongly on the type of cancer, is on average as low as about 30 percent. Within this statistics a patient is counted as cured if he survives five years without a recidivism. Since a lot of recidivisms take place after more than five years this definition of healing rates is at most problematic.

It is evident that there is a need for more research in the field of cancer therapy with the ultimate goal of improving the healing chances. Despite the recent major advances in biotechnology and the overwhelming amount of experimental data available, the theoretical mechanisms which govern the onset and progression of cancer are, to a large extent, still unknown. There is a necessity to develop theoretical models which are able to integrate the flood of experimental data in oder to make new predictions and optimise treatment strategies. An interdisciplinary approach is inevitable, since the problem of cancer modelling lies at an intersection between biology, medical science, physics, mathematics and computer science. This is also where the field of systems biology emerged during the last years, combining approaches from different areas of science.

A holistic model with spatial resolution on the subcellular level would be able to capture most of the relevant complex phenomena important for the onset and treatment of cancer. However, such a simulation is not available at present. Building the first steps for such a computer simulation which is able to model the dynamics of the tumour and the effects of irradiation, taking into account processes at the subcellular level, is the goal of this thesis. The development will be continued within the interdisciplinary CARADI research project[2]. Ultimate goal is a model which is able to relate the deposited radiation dose to the dynamical effects of partial tumour destruction. Such a model could be used to optimise treatment planning and investigate the complex mechanisms which determine the tumour's reaction to radiation.

[1] `http://www.who.int/mediacentre/factsheets/fs297/en/`
[2] `http://www.systems-immunology.de/RESEARCH/cancer.html`

Advantages of modelling

Theoretical models open up the possibility to check hypotheses within the framework of a reference system. This is advantageous since experiments can be done in silico without the need for laboratory animals or clinical trials, which offers not only financial and temporal benefits but is also to be preferred from an ethical point of view. However, in order to be useful a model needs to correspond to reality and have predictive power. This is attainable through the use of physical model parameters and connection to experimental results.

Models differing in their basic assumptions are used in the field of tissue modelling to capture cell dynamics (for a comprehensive overview about the field see *Roose et al.* (2007) or *Drasdo* (2003)):

Differential equation models rely on population modelling with ordinary differential equations (ODEs) or density modelling with partial differential equation (PDEs). Therefore they provide well-established mathematical techniques (see *Murray* (2002a) for details), however, they do not allow modelling of small systems (which are at the root of the cancerogenic process). Furthermore, if ODEs are in use, they suffer from a lack of spatial resolution and the introduction of abstract parameters which can not be easily verified in experimental systems.

Lattice-based cellular automatons or event models make use of model space discretisation and fixed interaction rules. Cells are assigned each to a lattice cite (as in *Dormann and Deutsch* (2002)) or are defined by a boundary of sites (see *Graner and Glazier* (1992)). Irregular lattices can be used e.g. static Voronoi tessellations as in *Kansal et al.* (2000). An extension is the use of probabilistic instead of deterministic interaction rules. Furthermore it is possible to couple diffusion to the lattice within the hybrid cellular automaton approach (as in *Deutsch and Dormann* (2003), *Beyer et al.* (2002)). Cellular automatons are captivating through the simplicity of the underlying rules, but this simplicity is also the source of problems such as lacking of biologically relevant mechanisms. Artificial rules and discretisation of the system space may lead to the development of lattice artefacts.

Continuous, agent-based models are centred around cellular agents, which are designed to resemble real cells. Cell shape and interaction may be defined according to physical rules (see *Palsson* (2001), *Dallon and Othmer* (2004)) or mediated by potentials (as in *Drasdo* (2003)). These models offer a continuous, lattice-free representation of the system space, and thus may represent the tissue in a realistic fashion. The cell shape can also be determined by the neighbouring cells within a Voronoi tessellation (see *Meineke et al.* (2001) and *Schaller and Meyer-Hermann* (2005c)). Interactions may be Newtonian force-based where experimental parameters may be taken from, or integrated into the simulation, which enables a rich communication between experimental and theoretical approaches to tissue modelling. Each cell is represented

individually, which is favourable for tumour-modelling because it can represent the monoclonal origin of cancer and capture the diversity of a tumour.

The general applicability of agent-based models to tissue simulation has been demonstrated multiple times, for examples see *Schaller and Meyer-Hermann* (2005a), and *Drasdo and Hohme* (2005). For realistic tissue modelling the agent-based approach seems to be inevitable. Even though it comes at the price of high computational demands, it offers a range of benefits which are of paramount importance.

Goals of modelling

The goal of this thesis is to build an agent-based, lattice-free simulation-environment for the modelling of tumour growth and treatment. This environment will include:

cell dynamics within a contact model for cell interactions

intracellular dynamics of the cell cycle and its regulation

reaction-diffusion of cell nutrients and pharmaceuticals, immuno-agents or the like

tumour dynamics in the formation of a typical tumour spheroid morphology

irradiation modelling within a minimal model of radiation damage

solved as a multi-scale problem. Due to its lattice free architecture it will be a realistic continuous modell close to real tissue. The agent-based approach makes modelling from the first cell possible, using a Newton-based simple interaction system with no arbitrary rules. Results of this simulation environment will be comparable to experimental results from clinical trials and can be checked against simple cell culture experiments for cheap and efficient improvement of the simulation. The use of experimentally accessible parameters will thus yield synergy effects between experiment and theory. A major use of model systems will be to scan the wide landscape of possible experiments with simulations in order to propose such experiments which are likely to produce highly interesting results. A modular layout of the application and open programming will ensure the expandability of the application within the CARADI-project.

The CARADI-project

The project will create a modelling environment enabling researchers to examine the growth of tumours and their reaction to radiation. Applications could be focussed especially on the planing and optimisation of clinical treatment. The application will feature a multi-scale approach considering the intracellular dynamics as well as overall tumour topology.

The interdisciplinary CAncer RADIation research project aims at modelling tumour dynamics under the action of irradiation and response of the immune system and includes microscopic mechanisms of biomolecule damage induced by ionic radiation. For more information on this project the reader is referred to `http://www.systems-immunology.de/RESEARCH/cancer.html`.

Outline

In order to approach the problem of cancer modelling and treatment simulation, this thesis will first take a look at the biology of cancer in chapter 1, where a brief introduction into the topics of cancerogenesis, tumour growth and treatment of cancer is given. As a modelling approach for tumour growth has to start from the first cell on, the basic properties of the cell and their mathematical treatment are the subjects of chapters 2 and 3. Special attention has to be paid to the implementation of a realistic interaction model for the cell. An implementation of the cell cycle is developed in chapter 5. Dynamic numerical problems associated with cell movement are treated in chapter 4 which comprises the development of an advanced adaptive algorithm which handles the time-integration of the cell's equation of motion. The implementation of cytokinesis within an agent-based simulation will be the topic of chapter 6. This will feature the development of a sophisticated cytokinesis procedure which improves the performance of the model. The advantages of using triangulations for tissue modelling are introduced in chapter 7. An overview of the final developed application, which features all the relevant mechanisms for modelling, is given in chapter 8.

Within chapter 9 the tissue simulation application developed in this thesis is applied to model problems such as tissue sorting and the dynamics of avascular tumour growth. The results obtained are compared to experimental findings. As cancer therapy with radiation is of special interst for this thesis, chapter 10 will give a brief introduction into the mechanisms responsible for the success of tumour therapy with radiation, having its main focus on heavy ion radiation. A minimal model of how to implement the mechanisms into a simulation environment is developed and applied to tumour simulations. Effects observed during the modelling are discussed. Chapter 11 will close the thesis with a subsumption and discussion of the obtained results. Further mechanisms to be implemented and future fields of investigation for the model are highlighted.

Thus, overall a circular layout will be used, with cancer being the leitmotif of the investigation. Starting from cancer the thesis will take a closer look at its origins and the single cell's properties, eventually returning to cancer modelling and irradiation.

1 Biology of cancer

1.1 Cancerogenesis

The human body is comprised of more than 10^{14} cells which form a complex network of interacting tissues. Somatic cells die and are replaced all the time in the homeostasis, as it is the goal to preserve only the unchanged germ line through reproduction (and eventually recombination with another germ line). Mutations of a single cell can lead to an unfavourable rise in proliferative fitness which might ultimately be fatal. Once a cell looses its ability to divide in a controlled fashion, a chain of events might begin which eventually can lead to cancer.

Multi-mutation theory and the origins of cancer

The multi-mutation theory, also called Knudson hypothesis, is the hypothesis that cancer is the result of accumulated mutations to a cell's DNA. It was first proposed by Carl O. Nordling in 1953, when he noted that in industrialised nations the frequency of cancer seemed to increase according to the sixth power of age. In 1971 Alfred Knudson formulated the hypothesis, that this correlation could be explained by assuming that the outbreak of cancer requires the accumulations of six consecutive mutations. The Knudson hypothesis led indirectly to the identification of cancer-related genes.

Mutations can occur within the cells DNA due to various mechanisms, which include spontaneous mutations that occur due to errors in DNA replication and repair, ionising radiation, chemical agents (deaminating agents, such as Nitrous acid, intercalating agents such as Ethidium bromide etc.) and other mutagens. However, a healthy cell holds a multitude of complex mechanism to repair such mutations or commit suicide if these mutations cannot be repaired.

Oncogenes and tumour suppressor genes

If DNA mutations occur in critical positions, such as genes that regulate the cell growth and response to extracellular signals, the damage can lead to cancerous growth. In fact, cancerous cells acquire a combination of the properties shown in figure 1.1.

Definition 1 (*Oncogenes and tumour suppressor genes*)

Carcinogenesis depends both on the
activation of oncogenes - genes that stimulate cell proliferation - and
deactivation of tumour suppressor genes - genes that keep proliferation in check.

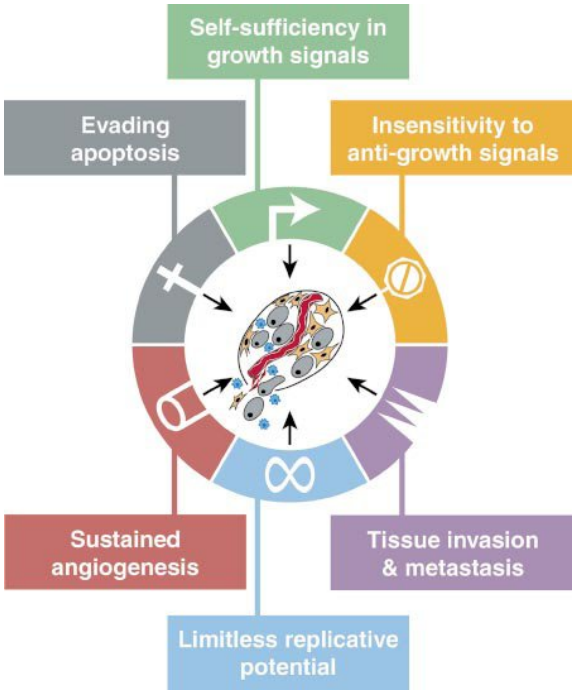

Figure 1.1: Cancerous cells show common properties which they acquired through mutation. Not every cancer acquires the full set of features. Figure taken from *Hanahan and Weinberg* (2000).

A first mutation in an oncogene does not necessarily lead to cancer, as normally functioning tumour suppressor genes (TSGs) still counterbalance this impetus. Only additional damage to TSGs would lead to unchecked proliferation. Conversely, a damaged TSG does not lead to cancer unless there is an activated oncogene in the cell. TSGs generally follow a two-hit hypothesis: both recessive alleles that code for a particular gene must be affected before an effect is manifested. If only one allele for the gene is damaged, the second can still produce the correct protein. Oncogene alleles in contrast are typically dominant.

Examples include genetically mediated disfunctions of the cyclin dependent kinases regulating pathways (see for example *Hilakivi-Clarke et al.* (2004)). It is the aim of ongoing research to uncover more and more oncogenes and TSGs through genetic screening and to finally unwind the complex interactions in these regulating gene networks.

Development of a tumour

The chain of events which leads from a single deregulated cell to full scale cancer can be schematised as follows:

1. Genetic mutation which disables response to cell cycle regulation mechanisms within one cell (monoclonal origin)
2. Hyperplasia - which is still benign - deregulated cell divides and forms a tumour which remains small
3. Dysplasia (malignant) where the tumour stops responding to killer-signals and grows exuberantly

4. In situ cancer, which is threatening the surrounding tissue but still remains compact
5. Invasion (metastasis) upon which cancerous cells are spread throughout the body

An evolving tumour comprises about 10^8 cells when it becomes visible on x-ray images, ten times more before it becomes palpable and typically around 10^{12} cells when its existence proves to be fatal for its host organism.

1.2 Tumour growth and typical morphology

The typical morphology of a tumour spheroid develops due to the limited nutrient supply through diffusion into the tumour. Glucose availability, for example, is decreasing with growing distance to the tumour boundary. Therefore, while cells on the boundary are well-fed and continue to multiply, cells with greater distance to the boundary are either growing much slower or are forced to enter quiescence at the restriction point. This effect gives rise to a quiescent cell core during the early stage of tumour spheroid growth.

During later stages of growth, the depletion of nutrients in the core of the tumour reaches a level upon which survival becomes impossible for the tumour cells. A necrotic core starts to develop which leads to inflammation, attracting immune agents into the core and leading to the excretion of growth-inhibiting factors. At this stage the final morphology of the avascular tumour is present. A core of necrotic cells is surrounded by a layer of quiescent cells with actively dividing cells at the boundary of the tumour spheroid (see figure 1.2 for an illustration of the spheroid growth).

Multicellular tumour spheroids (MCTS) are a three dimensional cultures of cancerous proliferating cells. They are often studied *in vitro* (see for example *Casciari et al.* (1988), *Wehrle et al.* (2000),*Freyer* (1998)) or *in silico* (e.g. *Ward and King* (1997), *Drasdo and Hohme* (2005)) as a model system of avascular tumour growth, due to the fact that they are simple in their cultivation but at the same time able to capture the relevant processes at the heart of cancerogenesis (see figure 1.2). MCTS show the distinct tumour topology which develops as described above. This topology should be reproducible by an agent-based model as a basis for further developments.

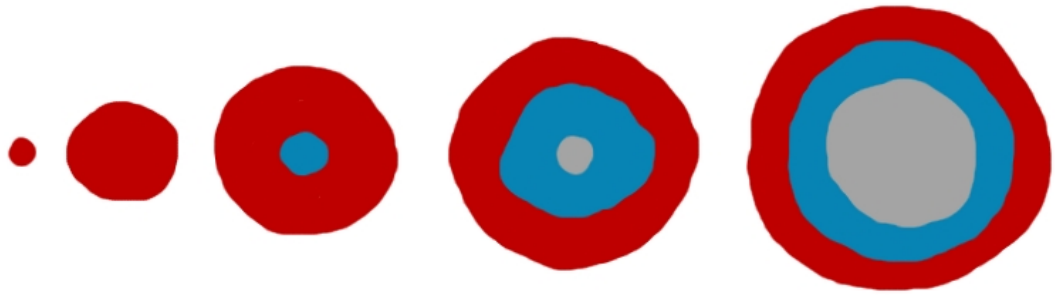

Figure 1.2: Commonly accepted morphology of a MCTS showing the outer proliferating region, the intermediate quiescent layer and the necrotic core. These distinct regions form as the MCTS grows in size. Nutrients can only diffuse into the spheroid volume through the boundary, thus, with growing size, the nutrient concentration inside the tumour decreases. Upon reaching a critical level cells in the tumour core enter quiescence. This core of quiescence cells increases in size with the tumour until the available nutrient concentration in the core drops to a level where cells are dying through necrosis.

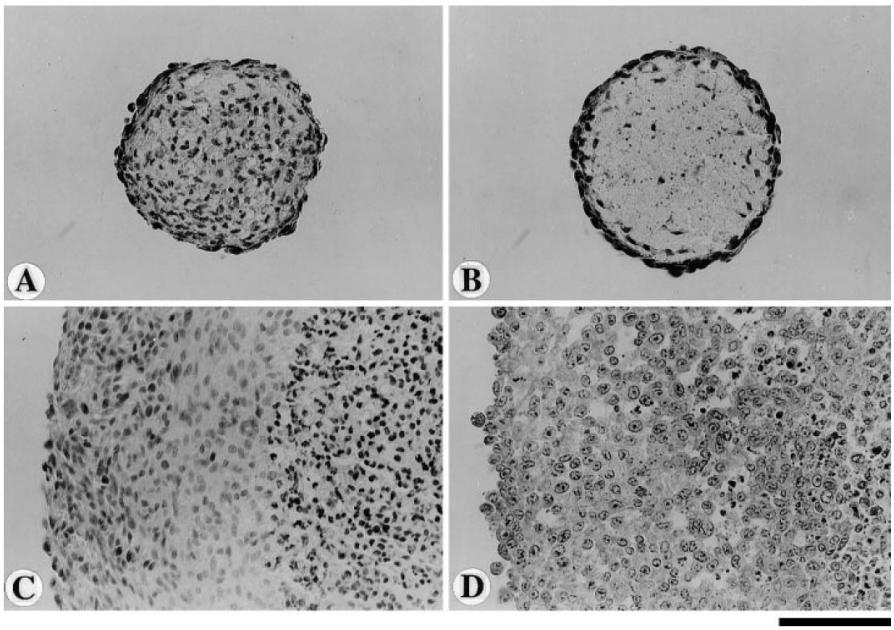

Figure 1.3: Histological structure of spheroids from differently transformed rat embryo fibroblasts. Representative $5\mu m$-thick median, hematoxylin and eosin-stained paraffin sections of Rat1 (A) and M1 (B) aggregates with a diameter of 150–$200\mu m$, and Rat1-T1 (C) and MR1 (D) spheroids with a diameter between 1200 and $1300\mu m$ (sector magnification). Bar size is $100\mu m$. Figure and caption from *Kunz-Schughart et al.* (2000).

Tumour angiogenesis / Vascularisation

In the beginning tumours cannot grow beyond a certain size, generally $1 - 2mm^3$, due to a lack of oxygen and other essential nutrients. Therefore tumour growth would be rather slow or even reaching a saturated state due to nutrient limitation and mechanical inhibition of cell growth. However, tumours may induce blood vessel growth (angiogenesis) by secreting various growth factors (e.g. Vascular Endothelial Growth Factor or VEGF) to ensure a continuous supply of nutrients. Growth factors, such as bFGF and VEGF can induce capillary growth into the tumour, thereby delivering required nutrients into quiescent regions and serving as a waste pathway for end products of the rapid division taking place inside the spheroid.

Angiogenesis is a key step for the transition of a tumour from a small harmless cluster of cells to full scale cancer. Furthermore, angiogenesis also opens up a pathway for the spreading of the tumour via metastasis, where single cancer cells can break away from an established solid tumour, enter blood vessels, and be carried to a distant site, where they can implant and begin the growth of a secondary tumour.

Mutations inside the tumour

In cancerous cells some of the DNA repair mechanisms are no longer working. If, in addition, the apoptotic pathway is blocked, mutations rapidly accrue within cancerous cell populations. These mutations allow the cancer cells to develop drug resistance and escape various therapy attempts. They also lead to the rise of multiple sub-populations in one tumour, which may show different reactions to pharmaceuticals, further complicating the treatment. This diversity can be easily captured in an agent-based model.

Hypoxia in tumour tissue

According to the Warburg hypothesis, cancer is a problem of mitochondrial deregulation. It was postulated by the Nobel laureate Otto Warburg in 1924, when he hypothesised that cancer is caused by the fact that tumour cells mainly generate energy by non-oxidative breakdown of glucose. Since this breakdown takes place within the mitochondria, according to Warburg, cancer should be interpreted as a mitochondrial dysfunction. Warburg reported a fundamental difference between normal and cancerous cells to be the ratio of glycolysis to respiration; this observation is also known as the Warburg effect.

Today this hypothesis is generally assumed to be wrong. Nevertheless, anaerobic metabolism might play an important part in tumour growth and its interaction with its environment.

Under hypoxic conditions the only possible solution for the survival of cells is a change in the metabolism to anaerobic combustion of glucose. However, as discussed in section 5.3, this leads to a production of lactic acids. If large parts of a tumour use anaerobic glycolysis as part of their metabolism this leads to an acetous court around the tumour spheroid. Depending on the amount of acid produced and the tolerance of the surrounding tissue this has a strong impact on the interaction between the tumour and its surrounding.

1.3 Weapons in the war on cancer

Since cancer is one of the major causes of death worldwide, a wide variety of treatment methods has been developed so far, including classical methods such as surgery, chemotherapy, and radiation therapy, but also newer and only partially tested approaches such as immunotherapy, antibody therapy, bacterial treatments or thermotherapy. The choice of therapy heavily depends upon the cancer type and grade of the tumour.

Complete removal of the cancer without damage to the rest of the body is the goal of treatment. In early stages this goal can sometimes be accomplished by surgery. However, the propensity of cancers to invade adjacent tissue or to spread to distant sites by microscopic metastasis often limits its effectiveness. In general almost every therapy has its special field of application and often comes with distinct drawbacks to it. In many cases combinations of multiple therapeutical approaches are applied in adjuvant therapy, i.e. chemotherapy given after surgery, or neoadjuvant therapy.

Due to the high rate of mutations, even within one tumour, it is quite unlikely that a single cure for cancer can be found - a combination of treatments will probably always offer the best chances in cancer therapy. This is another reason why continued research is necessary in the field of tumour biology. This section provides a brief overview of some available therapies for cancer.

Surgical treatment

As mentioned in the previous paragraph, cancer is curable if the tumour can be completely excised by surgery. However, this ideal situation is seldom present in clinical cases. The tumour boundary tends to get irregular through the invasion of surrounding tissue, making it hard to determine where to stop the excision. If even small parts of the tumour remain in the body after surgery, they may spread again rapidly and lead to tumour recurrence. Cells which were previously quiescent due to insufficient nutrient supply may restart to proliferate. Therefore a removed surgical specimen has to be examined thoroughly in order to make sure that the tumour has been removed with a thin layer of healthy tissue surrounding it. Surgery is quite often used in combination with chemo- or radiation-therapy (before or after surgery) greatly increasing the chances of eliminating the cancer.

Another problem arises with inoperable tumours. If the tumour is surrounded by delicate tissue, as it is common with brain tumours as the glioblastoma multiforme, surgical therapy becomes completely impossible. Surgical excision of metastasised cancers is usually also not possible. Surgery is often used in order to determine the extent of the tumour and check if metastasis to regional lymph nodes has happened. Based on this staging a prognosis can be generated and the need for adjuvant therapies determined.

Radiation therapy

Radiation has a long history of medical applications and has been in use as a cancer treatment for about 100 years. Early experiments were done soon after discovery of x-rays by Wilhelm Röntgen in 1895. Upon the discovery of the radioactive elements polonium and radium followed their use in medical treatment and research. Later on radiation from linear accelerators has been used in medical applications (since the late 1940s) because of their penetrating energies and lack of physical radiation sources.

A basic distinction has to be made between methods where radioactive substances are brought into the body (brachytherapy) and radiation therapy as the medical use of ionising radiation (external beam therapy). The former is mainly used to treat localised prostate cancer, cervical cancer, and cancers of the head and neck, where a sealed radioactive source is placed inside or next to the area requiring treatment. The latter one may be used for curative, adjuvant or palliative cancer treatment (where cure is not possible and the aim is local disease control or symptomatic relief).

Development of imaging technologies such as computed tomography (CT), magnetic resonance imaging (MRI) in the 1970s and positron emission tomography (PET) in the 1980s made effective 3D treatment planing and effective monitoring of dose delivery possible. The latest advances were the usage of heavy ion radiation for treatment and the dose delivery in scanning procedures such as IMRT and IGRT. As a result of these advancements the treatment outcomes are improving steadily as side effects are decreasing.

As simulation of radiation therapy is a main target of this thesis, the topic is discussed in detail in section 10.

Chemotherapy

Chemotherapeutic treatment of cancer makes use of cytotoxic drugs which affect rapidly dividing cells in general. Most chemotherapeutic drugs disturb cell division for example by preventing cell division or chromosome alignment. As the majority of cells in the human body is in quiescent state, this treatment affects mostly the cancerous growing cells, but unfortunately also all healthy tissue that shows a high replacement rate, such as hair follicles or the intestinal lining. Since repair capacities of healthy cells are usually superior to cancerous cells, parts of the damaged healthy cells can regenerate after chemotherapy.

While usually affecting all cells, some chemotherapeutic agents can show a certain degree of specificity by targeting the inability of many cancer cells to repair DNA damage.

It is common practice to combine multiple drugs in a treatment to make use of synergetic effects (known as combination chemotherapy).

Virotherapy

Virotherapy makes use of “reprogrammed” viruses, such as the herpes simplex or adenoviruses, to attack cancerous cells, only leaving healthy cells undamaged. As early as the 1950’s doctors were noticing that cancer patients who suffered a non-related viral infection,

or who had been vaccinated recently, showed signs of improvement. This phenomenon has been attributed to the production of interferon and tumour necrosis factors in response to viral infection. Nowadays oncolytic viruses are being designed that selectively target and lyse cancerous cells only.

Vaccination and cell-mediated immunity

Using the immune system of a patient itself to eliminate a tumour is the target of cancer immunotherapy. Vaccines that generate a specific immune response to cancerous cells through cell-mediated immunity are the target of research today (see e.g. *Knuth et al.* (2000) for details). Allogeneic hematopoietic stem cell transplantation (commonly referred to as "bone marrow transplantation" from a genetically non-identical donor) also can be considered to be immunotherapy. Immune cells of the donor will often attack the tumour in a phenomenon known as graft-versus-tumour effect. For this reason, allogeneic HSCT leads to a higher cure rate than autologous transplantation for several cancer types, although the side effects are also more severe.

Other treatment strategies

New treatment methods and strategies for cancer are under development all the time, from the delivery of nanoparticles (see *Koo et al.* (2006)), either as a vector for drugs or for treatment with heating due to radiation, to new combinations of existing treatment methods. Thermotherapy exploits the sensibility of tumour tissue to temperature and tries to heat or cool the tumour volume. Targeted therapy makes use of inhibitors for mutated, overexpressed or otherwise critical proteins within the cancer cell and relies strongly on the knowledge of detailed genetic mechanisms. Angiogenesis inhibitors are another group of promising drugs which can help to keep cancer in check through the inhibition of blood vessel formation in the tumour.

2 The cell and its in silico implementation

2.1 Basic characteristics of cells

A single cell is the building brick for complex multicellular organisms, but it is also a extremely complex object in itself. Each cell is self-contained and self-maintaining in the sense that it can convert nutrients into energy, carry out specialised functions, and reproduce as necessary. Its own building plan is stored in each cell's DNA.

All cells have several different abilities in common:

Cell division as reproductive mechanism which is realised by binary fission in prokaryotes and mitosis or meiosis in eukaryotes.

Protein synthesis wherein proteins coded for by the cells DNA are built.

Metabolism by which nutrients are taken up, energy is extracted and used to build cell components.

Stimuli response by which cells can respond to internal and external stimuli, like growth factors, acidity changes and so forth.

Two basic types of cells have to be distinguished, namely eukaryotic and prokaryotic cells. Eukaryotes are about 10 times the size of a typical prokaryote and contain membrane-bound compartments in which specific metabolic activities take place. The cell nucleus, which stores the cells DNA aligned in linear chromosomes, associated with histone proteins, is the most important among these. Note that some eukaryotic organelles, such as mitochondria, also contain small amounts of DNA called mitochondrial DNA (mtDNA). Material is moved between these compartments by regulated traffic and transport of small spheres of membrane-bound material called vesicles. While prokaryotic cells are usually independent, eukaryotic cells are often found in multicellular organisms. Therefore only the latter ones are of interest for the modelling of multicellular tumour spheroids.

Cell membrane and interaction

A realistic model for tumour growth must start at the single cell[1] and its mechanical properties. Each cell is surrounded by a cell or plasma membrane defining the cell boundary. This membrane separates the cell interior from the surrounding exterior. It is comprised of a double layer of hydrophobic lipids and hydrophilic phosphorus molecules. Therefore,

[1] If not stated otherwise "cell" refers to eukaryotic cells throughout this thesis for reasons of simplicity.

the membrane is called a phospholipid bilayer. A variety of different functional proteins are embedded in the membrane (see figure 2.1(b)):

Channels and pumps which regulate the exchange of substances between the cell interior and exterior by passive or active transport.

Cell adhesion molecules (CAMs) which mediate the binding to the extracellular matrix (ECM) and other cells.

Receptor proteins enable the cell to detect external signal molecules (e.g. hormones).

For an isolated cell a spherical shape arises through hydrostatic pressure and cell surface tension (*Lecuit and Lenne* (2007)). However, the cell shape is largely governed by the cytoskeleton, which acts as the cells scaffold. The cell shape can thus actively change with its help. The cytoskeleton consists of microfilaments, intermediate filaments and microtubules (see figure 2.1(a)). It is also responsible for fixing cell organelles in place, cytokinesis and the separation of daughter cells, as well as growth and motility in general.

Differential adhesion between cells

Cell Adhesion Molecules (CAMs) are proteins located on the cell surface which are involved in the binding with other cells or the extracellular matrix. They play an important role in mediating differential cell adhesion (see figure 2.1). CAMs are transmembrane receptors composed of:

- an intracellular domain that interacts with the cytoskeleton (anchor)
- a transmembrane domain
- an extracellular domain which either binds homophilically to other CAMs of the same kind or heterophilically with other CAMs or the extracellular matrix (adhesion protein)

CAMs can be subdivided into four protein families: cadherins, integrins, immunoglobulin superfamily CAMs (IgSF CAMs) and selectins. Cadherins are transmembrane adhesion proteins which depend on calcium ions. They are responsible for cell adhesion in cadherin-based adherens junctions, where they are linked with actin filaments. Integrins act as surface receptors in signal transduction and as adhesion molecules. Selectins are transmembrane proteins which bind to sugar polymers. IgSF CAMs are a family of diverse adhesion molecules which are structurally similar to antibodies (Ig).

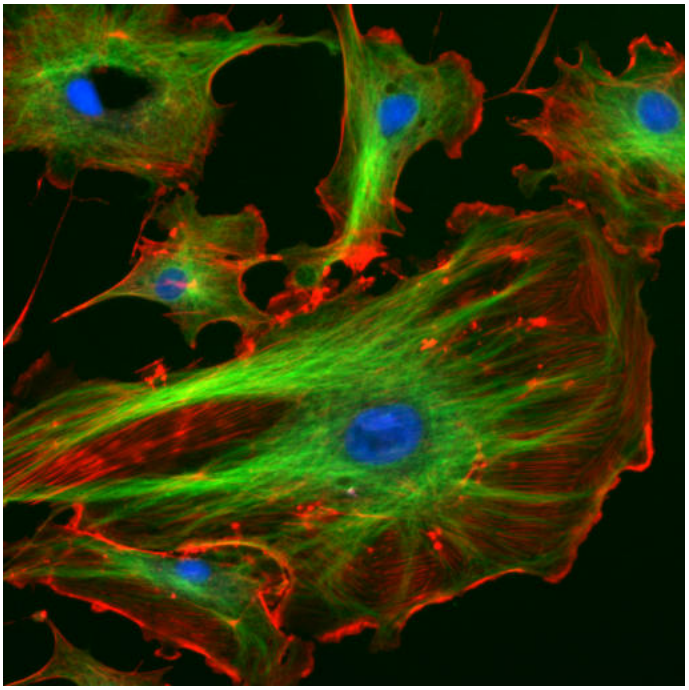

(a)

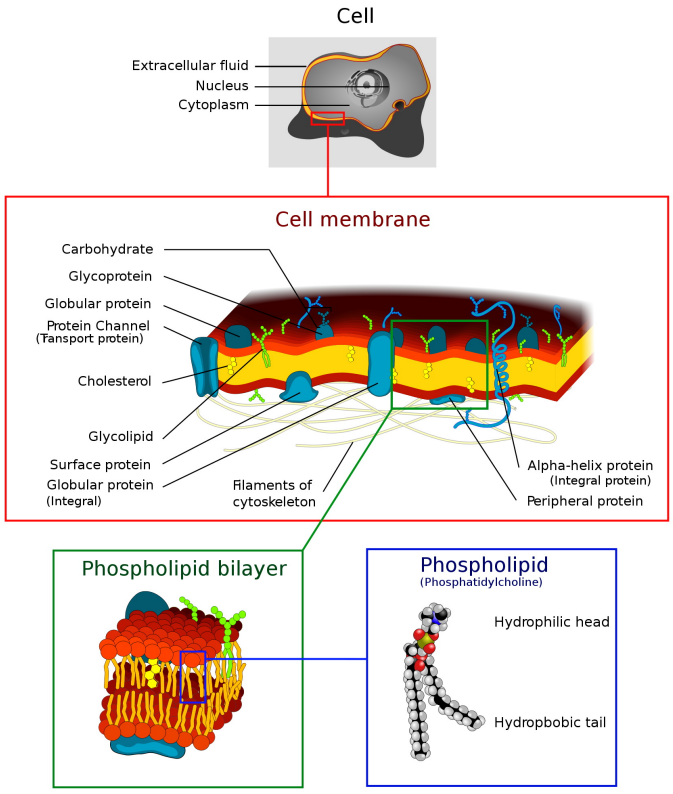

(b)

Figure 2.1: **(a)** Endothelial cells under the microscope. Nuclei are stained blue with DAPI, microtubules are marked green by an antibody bound to FITC and actin filaments are labelled red with phalloidin bound to TRITC. Bovine pulmonary artery endothelial cells are used. **(b)** Schematic view of the cell membrane depicting its composition and important parts. Figure (a) is in public domain under terms 1, figure (b) under term 2.

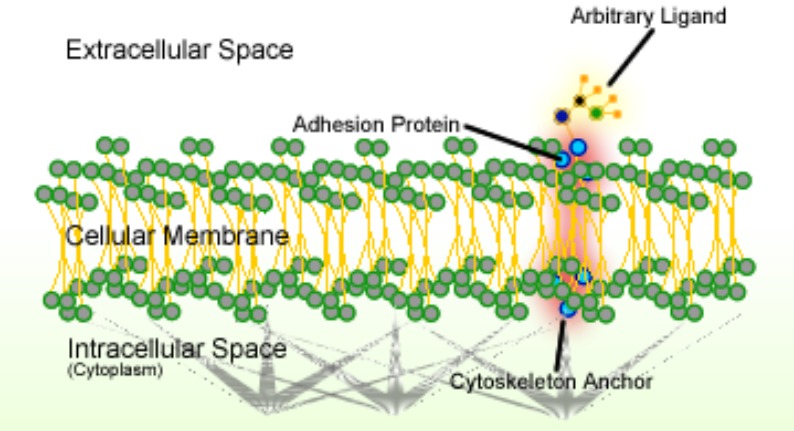

Figure 2.2: Mechanisms of cell adhesion. Most cell adhesion molecules (CAMs) are transmembrane proteins linking to the cytoskeleton of a cell in the intracellular space at the cytoskeleton anchor. Their extracellular domain might bind to other adhesion molecules or signalling molecules depending on the CAMs function. Picture in open domain.

The Extracellular matrix

The extracellular matrix (ECM) is a ubiquitous extracellular part of animal tissue (especially in connective tissue) which provides the cell with structural support and anchorage, segregating tissues from one another and regulating intercellular communication.

The extracellular matrix includes the interstitial matrix, which is present in the intercellular spaces between various cells and the basement membrane. The interstitial space is filled with gels of polysaccharides and fibrous proteins which act as a compression buffer against stress placed on the ECM. Basement membranes are sheet-like depositions of ECM on which various epithelial cells rest.

Cells are anchored in the ECM through the use of their CAM molecules (*Iozzo* (1998)). Especially the integrins bind cells to ECM structures, such as fibronectin and laminin, and to integrin proteins on the surface of other cells.

The ECM is of paramount importance for the cell's dynamic behaviour. It may dissociate cellular growth factors and may act as a depot for them. These local depots can be released upon trigger events such as grave changes in physiological conditions and are thus important for the regulation of processes like growth, wound healing and fibrosis.

In order for a tumour to invade surrounding tissue, it has to decompose the extracellular matrix using different enzymes (e.g. serine and threonine proteases). This mechanism is also important for tumour metastasis. For a detailed description, the reader is referred to the standard textbooks of the field, such as *Cotran and Robbins* (1994).

The DNA

The deoxyribonucleic acid (DNA) of a cell holds the information necessary for its development and functioning. It consists of two long nucleotide polymers with supporting backbones of ester bound sugars and phosphate groups. The DNA strands are anti-parallel, as they run in opposite direction to each other, both coding the same information. The nucleotides attached to each sugar are either adenine (abbreviated A), cytosine (C), guanine (G) or thymine (T). Hydrogen bonds between these bases stabilise the DNA and the genetic code is stored within the base sequence. The eukaryotic DNA is organised in one or more linear molecules, called chromosomes, which are associated with histone proteins. All chromosomal DNA is stored in the cell nucleus, separated from the cytoplasm by a membrane.
The DNA codes the building plan for the cell itself as well as for all the proteins it will produce. This plan is translated in protein biosynthesis to produce functional proteins from amino acids. One strand of the DNA is used to obtain a template called messenger RNA (mRNA) in the process of transcription. Translation of this template occurs in the ribosomes of the cytoplasm. Their subunits surround the transcribed mRNA. According to its plan and the rules inherent in the genetic code, polypeptides are built using the sequence of the mRNA as a template to guide the synthesis of a chain of amino acids that eventually forms a protein.

Further details

Due to the complexity of the cell the introduction of all its beautiful mechanisms is beyond the scope of this thesis. A comprehensive but not at all exhaustive overview can be found in *Alberts et al.*.

2.2 Agent-based representation of a cell in C++

Within a simulation a detailed representation of a cell as an object is needed. In order to create a theoretical modelling framework of cell populations, the governing attributes of a cell have to be realistically abstracted into a mathematical model, which has to be as simple as possible in order to remain computationally feasible (see table 2.2). Using the object oriented programming language C++ a simple approach for the representation of a cell is the definition of a `cell`-class, which provides variables and functions that may be used by every instance of that class. Each cell is spawned by the constructor function of this class and is thereafter existent as an individual object. Each cell object is characterised by a state vector defining all cell attributes which are of importance to the simulation.
Defining properties of a cellular agent which are included in this state vector are for example:

Cell mechanism	Implementation type	Comment
elasticity	mechanistic	Hertz/JKR contact model
adhesion	mechanistic	JKR contact
CAM	mechanistic	adhesion term
pressure	mechanistic	pressure force
stimuli response	mechanistic	active motility responding to gradient
ECM	effective	frictional coefficient
protein synthesis	effective	cell biomass conversion and growth
DNA	effective	damage model
receptor proteins	not implemented	signalling only through diffusion
channels and pumps	not implemented	nutrients distributed through diffusion only

Table 2.1: Important cellular mechanisms and their type of implementation within this simulation. Mechanistic implementations rely on a realistic force based model for mechanism. Cell mechanisms implemented effectively are abstracted and simplified during their inclusion. The function of important unimplemented mechanisms is taken over by other implemented mechanisms.

mechanical parameters such as size, Poisson's ratio and CAM concentration on the membrane

internal parameters e.g. cycle phase, phase duration, DNA content

Functional properties of the cell, such as the cell cycle or replication, have to be implemented as member functions of the `cell`-class. This functions change the properties of the cell and its surrounding accordingly to observed mechanisms (e.g. mitosis, adhesion to neighbours). A full overview of the implementation developed in this thesis is given in section 8.

3 Cell shape and interaction

3.1 Cell interaction methods

Although much more complicated in real life, from a physicists point of view a cell can be abstracted to be an elastic, adhesive sphere. These abstracted cellular agents can grow, multiply (proliferate), and die (through necrosis or apoptosis). They may eventually aggregate to form a regulated tissue or cease to respond to regulatory signals and start to grow exuberantly, eventually forming a tumour.

A first step will be to deal with the interaction of two cellular agents. There are multiple ways for cells in a tissue to interact. Each of them may be modelled within a simulation to obtain realistic results. Possible interactions include:

- repulsive forces through Hertzian contact force
- adhesive forces through CAM-adhesion
- shear forces from moving neighbour cells
- repulsive pressure from cell indentation (hydrostatic pressure)

Complex phenomena like mechanical proliferation inhibition emerge from the interaction of these basic principles. Considering the simple cell model of elastic spheres, the aim is to find a realistic contact model which can be used in order to model the cellular interactions. It has been shown (see *Chu et al.* (2005) and *Schaller and Meyer-Hermann* (2005a)) that the Johnson-Kendall-Roberts model is a possible choice to calculate the cell interactions within the necessary parameter regime.

3.2 Abstraction of the cell interaction

The Hertz model

If two curved surfaces get into contact they are subject to localised stresses that develop due to the slight deformation under the imposed load. Heinrich Rudolf Hertz first studied these stresses and published his work on the topic in *Hertz* (1882). This stress is known as Hertzian contact stress and it is usually described with respect to the positions x_i, x_j of contacting spheres of different radii r_i and r_j. The amount of deformation and the rising repulsive hertzian contact force F_{ij}^{hertz} depends on the elastic modulus E and the

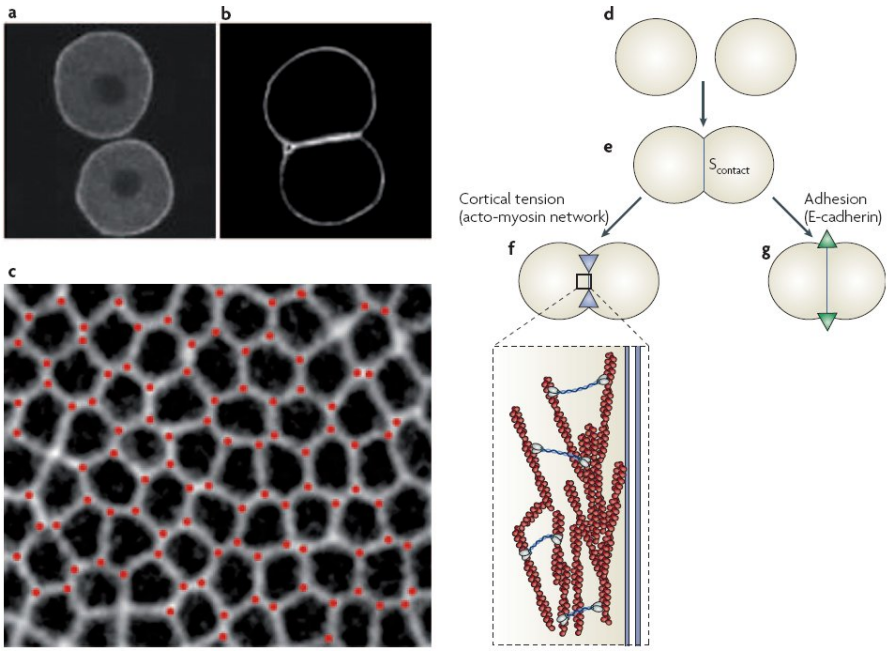

Figure 3.1: Shape of two free cells and of two cells in contact as seen under the microscope **(a+b)** and schematically **(d+e)**. Cell shape resulting from a mixture of tension (mediated by the actomyosin network **(f)**) and adhesion (through E-cadherin on the cell membrane **(g)**). **(c)** shows the arrangement of cells in a dense tissue which resembles polyhedra as found in a Voronoi tessellation. Figure from *Lecuit and Lenne* (2007).

Poisson ratio ν of the material. With $\hat{\mathbf{e}}_{ij} = \frac{\mathbf{x}_j - \mathbf{x}_i}{\|\mathbf{x}_j - \mathbf{x}_i\|}$ defining the normal of the contact plane between the two spheres and

$$h_{ij} = r_i + r_j - \|\mathbf{x}_j - \mathbf{x}_i\| \tag{3.1}$$

defining the penetration depths of the spheres, the Hertz force is given by the following expression:

$$\boldsymbol{F}_{ij}^{\text{Hertz}}(\mathbf{x}_i, \mathbf{x}_j) \quad = \quad E_{ij}^* \sqrt{r_{ij}^*}\, h_{ij}^{3/2} \hat{\mathbf{e}}_{ij}. \tag{3.2}$$

The effective elasticity E_{ij}^* and the effective radius r_{ij}^* used in equation 3.2 are determined by the elastic constants E_i, E_j, the Poisson ratios ν_i, ν_j and the radii of the spheres r_i, r_j as follows:

$$\frac{1}{E_{ij}^*} \quad = \quad \frac{3}{4}\left[\frac{1-\nu_i^2}{E_i} + \frac{1-\nu_j^2}{E_j}\right] \tag{3.3}$$

$$\frac{1}{r_{ij}^*} \quad = \quad \frac{1}{r_i} + \frac{1}{r_j} \tag{3.4}$$

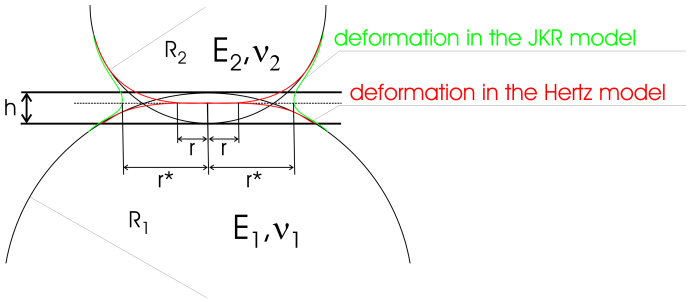

Figure 3.2: The Hertz model for elastic interactions. The deformation of two elastic spheres penetrating each other by a distance h is shown. In comparison the deformation in the presence of adhesion (JKR model) is shown. The contact plane indicated by the dashed line corresponds to the plane where the common face of the corresponding Voronoi cells of the two spheres is located. Figure from *Beyer* (2007).

Adding adhesion – derivation of the JKR model

The Hertz model may account only for the repulsive forces in cell interaction. Since cells are sticky through the expression of adhesion molecules on their surface, an additional adhesive term is needed to capture cell interaction. This leads to the model of Johnson, Kendall and Roberts (JKR) who showed in *Johnson et al.* (1971) that the effective contact radius a_{ij} between two spheres will be enlarged if adhesive forces are present (see figure 3.2).

The adhesive contribution to the force between the spheres is given by

$$F_{ij}^{\text{adh}} = -\sqrt{6\pi\sigma_{ij}E_{ij}^{*}{r_{ij}^{*}}^{3/2}h_{ij}^{3/2}} \tag{3.5}$$

and depends on the surface energy σ. The effective elasticity E_{ij}^{*} and effective radius r_{ij}^{*} are equal to the ones defined for the Hertz model in equation 3.3.

A linear combination of the purely repulsive Hertz model (*Landau and Lifshitz* (1959)) and the adhesive contribution from equation 3.5 yields the JKR contact force:

Equation 1 (*Johnson-Kendall-Roberts-force*)

$$\boldsymbol{F}_{ij}^{\text{JKR}}(\mathbf{x}_i,\mathbf{x}_j) \approx \{E_{ij}^{*}\sqrt{r_{ij}^{*}}\,h_{ij}^{3/2} - \sqrt{6\pi\sigma_{ij}E_{ij}^{*}{r_{ij}^{*}}^{3/2}h_{ij}^{3/2}}\}\hat{\mathbf{e}}_{ij} \tag{3.6}$$

F_{ij}^{JKR} is positive (repulsive) for large virtual overlaps, and negative (attractive) for small virtual overlaps h_{ij} (see figure 3.2 on page 24). Objects interacting according to the JKR model therefore tend to stay in an equilibrium distance for which the resulting force on the interaction partners is zero (as depicted in 3.3). This equilibrium distance depends on the radius of the object and is given in table 3.2 for cellular objects of different radii.

The load-displacement relationship given by equation 3.6 is an approximation following *Schaller* (2006) which is valid in the used parameter regime. *Johnson et al.* (1971) contains a definition for the JKR contact surface which is not easily transformed into a representation based on the penetration depth h_{ij} without ambiguities.

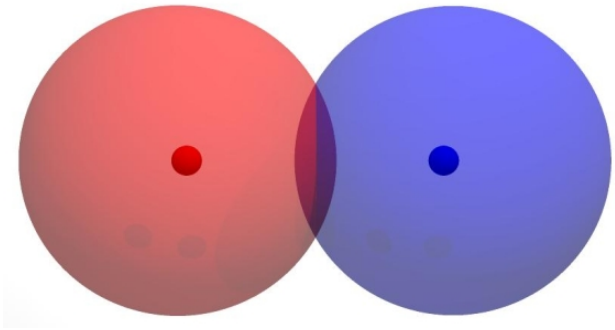

Figure 3.3: Visualisation of two spheres under JKR interaction in equilibrium distance. Pulling the cells further apart would result in F_{ij}^{JKR} to be attractive as the adhesive contribution is dominating. Further pushing of the cells together results in strong repulsive JKR force.

method	**cell type**	**viscosity** [Pa s]	**elasticity** [Pa]	**forces** f [nN]	**remarks**
magnetic bead microrheometer	3T3 fibroblasts	$2000 - 4000$	$G = 2 - 4 \cdot 10^4$	2	no strain hardening below 2 nN
magnetic tweezers, displacement field	J774 macrophages	210 ± 143	$G = 20 - 735$		no strain hardening
pressure plates	chicken embryonic	$10^4 - 10^5$	$G = 100 - 1000$		
micropipette aspiration, atomic force microscope	erythrocytes			14-27	
poking with glass needles	REF 52 fibroblasts			70	response is local
pulling cells	S180 + dextran		$E = 3500 \pm 1500$		JKR theory valid

Table 3.1: The results of different methods for measuring mechanical properties of cells. Elasticities are given as shear modulus G or Young's modulus E. Forces are either typical forces generated by cells or force applied to cells during experiment. Measurements from *Bausch et al.* (1998) (line 1 and 2), *Forgacs et al.* (1998), *Hategan et al.* (2003), *Heidemann et al.* (1999), and *Chu et al.* (2005). Compiled in *Beyer* (2007).

Realistic parameters for the JKR model

A advantage of the JKR model lies within the fact that it uses experimentally accessible parameters. Techniques like the atomic force microscope (AFM) or scanning force microscope (SFM) reach resolutions of fractions of a nanometer and are at the same time widely available and thus open up the possibility to probe these parameters. Recent advances include sophisticated methods such as scanning probes and field gradient traps (like optical tweezers) which can be used to examine mechanical parameters of living cells (see *Zhang and Liu* (2008), *Neto et al.* (2006), and *Hoffman et al.* (2006)). Through these techniques it is possible to measure single cell parameters like the elastic modulus, the Poisson ratio or the rupture force for a cell membrane (see table 3.2 for examples). Using an individual and force based model with JKR interaction for the cellular agents these measured parameters may be integrated (see *Chu et al.* (2005)).

cell type	**initial size (start of G_1)** $[\mu m]$	**final size (end of G_2)** $[\mu m]$	**JKR equilibrium distance** $[\mu m]$
small cell	4.76	6.0	7.32
medium cell	7.94	10.0	13.28
large cell	11.11	14.0	19.3
huge cell	15.87	20.0	28.6

Table 3.2: Example values for cell sizes and the resulting cell equilibrium distance in the JKR model. Parameters for JKR interaction are $\nu = 0.5, \quad E = 1nN/\mu m^{-2}, \quad \sigma = 0.1nN/\mu m^{-1}$.

Numerical evaluation of the JKR interaction

To obtain the JKR forces for the interacting system of cells, equation 3.6 was implemented in the `get_forces()`-function of the `Cell`-class. In order to ensure the correctness of the implementation, the output of the function was compared to the analytical solution.

Implementation of differential adhesion

To include differential adhesion strength in the model, cell agents show a distinct concentration of receptors c^{rec} and ligands c^{lig} on their surface and are thus able to show different binding energies depending on their concentration of CAM:

Equation 2 (*Differential adhesion through CAMs*)

$$F_{ij}^{adh} = A_{ij}\epsilon^{adh}\frac{1}{2}(c_i^{rec}c_j^{lig} + c_i^{lig}c_j^{rec}) \tag{3.7}$$

This force component can be added to the interaction force yielded by the JKR interaction. In this simplified approach the receptor and ligand concentration is assumed to be equal across the whole cell surface. The concentrations c_i, c_j can well be time-dependent e.g. according to the cell cycle.

An alternative way to include differential adhesion is to alter the JKR parameters e.g. the surface energy term to depend on the cell type of the interaction partners.

Other models for cell interaction

A variety of models exist for the calculation of cell interactions which take into account viscoelastic and nonlinear mechanical properties found in cells or make use of the tensegrity model (see for example *Bausch et al.* (1999), *Forgacs et al.* (1998), and *Canadas et al.* (2002)). A comprehensive overview of current models can be found in *Schaller and Meyer-Hermann* (2005a). See also the works of *Drasdo et al.* (1995), *Palsson* (2001), *Meineke et al.* (2001). While these models might be more sophisticated than the JKR interaction model, for a large simulation the employed contact model must be as realistic as possible at a given computational cost. High resolution and complex mechanisms for a single

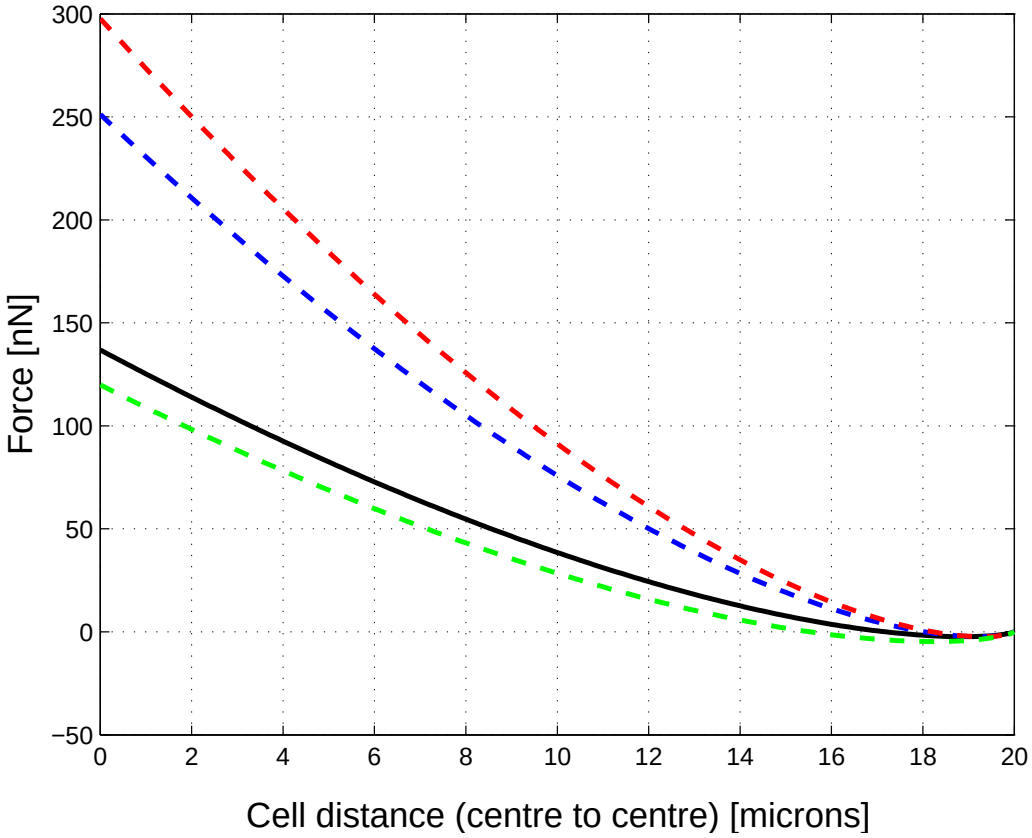

Figure 3.4: Analytical solution of the JKR force for different parameters. The solid black line depicts the JKR force in nN for cell of $10\mu m$ size and the parameter set typically used within this thesis ($\nu = 0.5, \quad E = 1nN/\mu m^{-2}, \quad \sigma = 0.1nN/\mu m^{-1}$). Deviating parameters for blue $\nu = 0.75$, red $E = 2nN/\mu m^{-2}$, and green $\sigma = 0.2nN/\mu m^{-1}$ curve. The JKR force is strongly repulsive for large overlaps (unphysiological regime) and attractive for a range of small overlaps. Resulting force is approximately linear for small deflections from the equilibrium position (between 16 and $18\mu m$). Contact between the cells is lost at a centre to centre distance of double the cell's size.

cell encompassed in a too sophisticated model render computation of complex tissues impossible, due to the huge number of simulation agents.

4 Modelling cell movement

4.1 Biological cell movement

Tissue gains its stability from the anchoring of its cells through CAMs, which form interconnections between adjacent cells and the extracellular matrix (ECM). Nevertheless, cells are highly motile objects and can move through this dense network by methods such as ECM-cleaving and the formation of protrusions.

The ability of a cell to move spontaneously and actively is called motility. This active movement usually requires the consumption of energy by the organism. Motility often refers to directed cell movement down gradients of which prominent examples include chemical gradients (chemotaxis) or gradients of cell adhesion sites (haptotaxis). Cells may have a defined time during which they can keep an orientation when following a gradient (often called polarisation time) and move actively in a distinct direction for prolonged periods of time until they repolarise.

A comprehensive introduction into the mechanisms of cell movement can be found in *Fletcher and Theriot* (2004).

Active cell movement will play a minor role when modelling multicellular tumour spheroid formation as the dominating component of cell movement will be passive cell movement through mitotic pressure and cell growth.

4.2 Integration of the cells equation of motion

Cell interaction with the JKR model yields forces in the range of nN depending on cell distance, physiological parameters and cell radius. Summation of these forces on a cell results in a total force which leads to passive cell movement. If cell cycle dynamics are disabled, this leads to a cool-down of the tissue into an equilibrium (see figure 9.2 on page 82).

The basic scheme to implement cell movement is to calculate the total interaction force for all cells in discrete timesteps, obtain a cell displacement for the current force determined by an adaptive timestep and then displace the cells simultaneously. Nearly motionless and very fast cells may be update asynchronously to improve the computational performance of the simulation. The finite steps result in an approximate solution of the cell movement, which is applicable as long as the allowed stepsize for the algorithm remains small.

Using an overdamped approach

In the previous section it was mentioned that cells are integrated into the ECM. This anchoring and binding to other cells results in an effectively dense medium of high viscosity. Modelling all the cell-ECM-interactions would be impossible for a large scale simulation of tumour dynamics, therefore the effects of the ECM are integrated into the simulation via a friction term in the cells equation of motion. A partial model of the differential interaction of cells with the ECM can easily be integrated by changing the viscosity of the medium in dependence of the integrin concentration on the cells surface.

Stokes friction can be used to calculate the friction of a cell

$$\gamma_i^{\alpha\beta} = 6\pi\eta R_i \delta^{\alpha\beta} \tag{4.1}$$

A cell's velocity decay is then given by the expression

$$v(t) = v_0 \exp\left\{-\frac{6\pi\eta r}{m}t\right\}. \tag{4.2}$$

If we assume movement of a cell with radius $r = 5\mu m$ and an initial velocity of $v_0 = 1\,\mu\mathrm{ms}^{-1}$ within water of viscosity $\eta = 10^{-2}P$ we can easily calculate a stopping distance using equation 4.2. This distance is $\frac{mv_0}{6\pi\eta r} \approx 10^{-11}\mathrm{m} = 0.01\,\mathrm{nm}$, which shows the extreme velocity decay. Taking into account that the effective viscosity of a dense tissue is much higher than that of water and the fact that cells are additionally bound in the ECM via there CAMs, it is obvious that neglecting accelerations does not impose an error on the simulation. Similar arguments for the soundness of the overdamped approach can be found in *Dallon and Othmer* (2004), *Schaller and Meyer-Hermann* (2005a) and *Beyer and Meyer-Hermann* (2007).

The cell's equation of motion

We obtain the Newtonian equation of motion for the cells by summing up all the forces which act on a cell i:

$$\boldsymbol{F}_i(t) = m_i\ddot{\boldsymbol{x}}_i(t) = \boldsymbol{F}_i^{act}(t) + \boldsymbol{F}_i^{fric}(t) + \sum_{j\in\mathcal{N}^c} \boldsymbol{F}_{ij}^{inter}(\boldsymbol{x}_i(t), \boldsymbol{x}_j(t)). \tag{4.3}$$

This includes active cell movement forces $\boldsymbol{F}_i^{act}$ i.e. from chemotactic movement, cell-ECM-friction $\boldsymbol{F}_i^{fric}$ and interaction forces with the cells neighbours in contact $\boldsymbol{F}_{ij}^{inter}$. Using Stokes friction for the cells and inserting expressions for the force components one obtains

$$m_i\ddot{\boldsymbol{x}}_i(t) = \boldsymbol{F}_i^{act}(t) - \gamma\dot{\boldsymbol{x}}_i(t) + \sum_{j\in\mathcal{N}^c} \{\boldsymbol{F}_{ij}^{JKR}(\boldsymbol{x}_i(t), \boldsymbol{x}_j(t)) \tag{4.4}$$

$$+\boldsymbol{F}_{\mathrm{ij}}^{\mathrm{CAM}}(\boldsymbol{x}_{\mathrm{i}}(\mathrm{t}), \boldsymbol{x}_{\mathrm{j}}(\mathrm{t})) + \boldsymbol{F}_{\mathrm{ij}}^{\mathrm{pre}}(\boldsymbol{x}_{\mathrm{i}}(\mathrm{t}), \boldsymbol{x}_{\mathrm{j}}(\mathrm{t})) + \boldsymbol{F}_{\mathrm{ij}}^{\mathrm{drag}}(\boldsymbol{x}_{\mathrm{i}}(\mathrm{t}), \boldsymbol{x}_{\mathrm{j}}(\mathrm{t}))\}. \tag{4.5}$$

With $\boldsymbol{F}_{ij}^{JKR}$ being the JKR force between neighbouring cells and $\boldsymbol{F}_{ij}^{CAM}$ the appropriate adhesion force mediated by the cell's CAM molecules. The pressure force $\boldsymbol{F}_{ij}^{pre}(\boldsymbol{x}_i(t), \boldsymbol{x}_j(t))$, which rises between neighbouring cells is implemented in the application but not used during most simulation runs. Other force components which can be included in a straightforward manner comprise cell drag forces $\boldsymbol{F}_{ij}^{drag}(\boldsymbol{x}_i(t), \boldsymbol{x}_j(t))$.

Assuming movement of the cell in a dense medium, the overdamped approach as introduced in the previous passage can be used to neglect acceleration:

$$\ddot{\boldsymbol{x}}(t) \approx 0 \tag{4.6}$$

Combining equation 4.3 (omitting seldom used force components for reasons of clarity) and 4.6 yields the equation of motion:

$$0 \approx m_i \ddot{\boldsymbol{x}}_i(t) = \boldsymbol{F}_i^{act}(t) - \gamma \dot{\boldsymbol{x}}_i(t) + \sum_{j \in \mathcal{N}^c} \{\boldsymbol{F}_{ij}^{JKR}(\boldsymbol{x}_i(t), \boldsymbol{x}_j(t)) + \boldsymbol{F}_{ij}^{CAM}(\boldsymbol{x}_i(t), \boldsymbol{x}_j(t))\} \tag{4.7}$$

This can be rewritten to obtain the cells velocity from the equation

Equation 3 (*Cell's equation of motion*)

$$\dot{\boldsymbol{x}}_i(t) = \frac{1}{\gamma}\{\boldsymbol{F}_i^{act}(t) + \sum_{j \in \mathcal{N}^c} \{\boldsymbol{F}_{ij}^{JKR}(\boldsymbol{x}_i(t), \boldsymbol{x}_j(t)) + \boldsymbol{F}_{ij}^{CAM}(\boldsymbol{x}_i(t), \boldsymbol{x}_j(t))\}\} \tag{4.8}$$

Equation 4.8 is evaluated for every cell in every timestep of the simulation. The resulting velocity is stored in the cell object.

Integration of object dynamics

The cell's velocity according to equation 4.8 has to be integrated in order to propagate the dynamics of the system correctly. In this process, the displacement that would result from movement with the given velocity for a given timespan is approximated with the help of an integration scheme. Here the forward Euler algorithm is the method of choice. Named after Leonhard Euler, the Euler algorithm is a first order numerical procedure for solving ordinary differential equations (ODEs) with a given initial value. It is the most basic kind of explicit method for numerical integration for ordinary differential equations, but preferable in this application for reasons that will be obvious shortly.

The idea is that while the trajectory of the cell is initially unknown, its starting point, which we denote by x_0, is known. This starting point corresponds to the initial cell position within the simulation. Then, from the differential equation, the slope to the trajectory at x_0 can be computed, which corresponds to the cells velocity given by equation 4.8. Now the system is propagated for a small step along that tangent line up to a point x_1. If we assume that the timestep Δt was small enough, x_1 will approximately be still on the initial curve. This scheme can be repeated and after several steps, a polygonal curve

$x_0 x_1 x_2 x_3 \ldots$ is computed. If the timestep is small enough, this curve does not diverge too much from the original unknown trajectory, and the error between the two can be made arbitrarily small. It is possible to approximate the solution of the initial value problem

$$x'(t) = f(t, x(t)), \qquad x(t_0) = x_0, \tag{4.9}$$

by using the first two terms of the Taylor expansion of x, which represents the linear approximation around the point $(t_0, x(t_0))$. This point is our cell's initial position. One step of the Euler method from t_n to $t_{n+1} = t_n + \Delta t$ is

$$x_{n+1} = x_n + \Delta t f(t_n, x_n). \tag{4.10}$$

which gives the approximate new position of the cell in the simulation. This straightforward approximation of the forward Euler method is applicable since the simulation timestep is small. At the same time, the choice of this simple algorithm is motivated by the inherent complexity of the problem which is to be simulated. An iterative algorithm of higher order like Runge-Kutta can be implemented easily but introduces the need for intermediate points at which the dynamics have to be evaluated. This involves recomputation of the systems triangulation, which renders higher order algorithms inefficient. An algorithm of second order results in an effective bisection of the simulation timestep, since intermediate steps are not known to the simulation. Implicit schemes for the solution of the system are not applicable since an inverse of the regular triangulation is not accessible.

4.3 Determination of the integration timestep

As mentioned in the introduction to the Euler algorithm, the choice of the stepsize is of paramount importance for the validity of the numerical approximation. If the stepsize is too big, the system will diverge from its analytical solution. An overly small stepsize, on the other hand, must be avoided in order to keep the system computable. An obvious choice for the timestep Δt is a solution which results in a maximum displacement that is still small compared to the simulation object. Thus for cell objects this maximum displacement Δx may be made dependent on the cell radius $\Delta x = 0.1 R_{cell}$. This choice is also preferable because this is exactly the region in which the JKR interaction yields a highly realistic model for the cell interaction (see *Chu et al.* (2005)).

Global adaptive stepsize

In order to make a system of agents moving with different speeds computable, an adaptive timestep is necessary to ensure that agents are only allowed to move within a realistic velocity frame, as discussed above. A robust approach to this is the variable timestep Δt used to propagate the system. This timestep depends on the velocity of the fastest object in the system and is chosen such, that the propagation of the fastest object at the given

timestep does not exceed the allowed movement threshold:

Definition 2 (*Global adaptive timestep*)

$$\Delta t = \frac{\Delta x}{v_{max}} \tag{4.11}$$

This relation is referred to as global adaptive timestep from now on. By this method the dynamics of the system can be integrated in a robust manner (see figure 4.1). However this method comes at the high price of enormous computational demands, since the timestep for the whole system is defined by the fastest agents.

Local adaptive stepsize

Single cells can speed up due to numerical inaccuracy or unfavourable configurations. This is especially the case in regions with high mitotic activity. A cell may be affected by multiple neighbours whose interaction forces add up in a way that yields an unphysiologically high cell velocity. So, in a model with a global adaptive timestep, few artificially fast cells determine the stepsize for the whole system. Thus, even cells which could be propagated with greater timesteps without the risk of numerical errors are moved with a small stepsize. A much more favourable simulation scaling could be achieved if the high resolution would only be applied where it is needed. This is the goal of a local adaptive stepsize algorithm. Since the artificial velocity of fast cellsis up to two orders of magnitude higher than the velocity of the slow cells in the system (see figure 9.1 for details), an adiabatic approach is applicable. In this case, the global adaptive stepsize algorithm (as in 4.11) is used to determine a propagation timestep which is not adapted to the fastest cell in the simulation, but to the average velocity of cells times a multiplicative scaling factor f_{ave}:

Definition 3 (*Local adaptive stepsize*)

$$\Delta t = \frac{\Delta x}{v_{ave} f_{ave}} \tag{4.12}$$

Due to the nature of the velocity spectrum, which shows only few mavericks, this approach results in the vast majority of cells being treated with a timestep as large as possible (in order to still stay below the spatial resolution Δx). The few fast cells which lie above v_{ave} are treated asynchronously with a smaller timestep before the whole system is evolved. Their velocity is recalculated for their new position repeatedly, taking into account their virtual displacement until the full propagation timestep of the whole system is reached (see figure 4.2). Typical total displacements resulting from this algorithm are of the same magnitude as the spatial resolution Δx, but may be cut if adaptive movement would exceed Δx. As the velocity of artificially fast cells is orders of magnitude higher than the

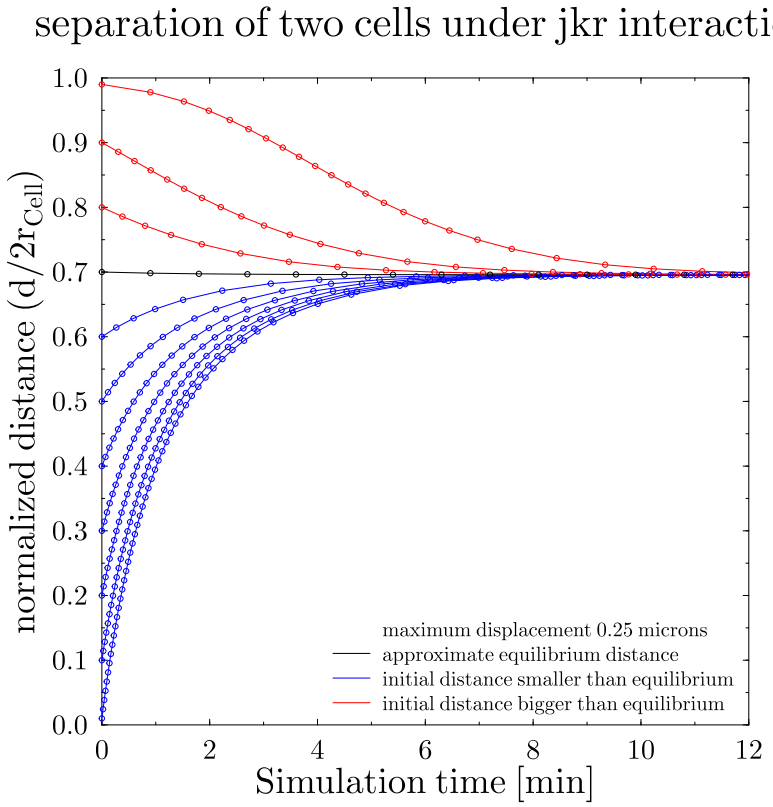

(a) Simulation of two cells separating due to JKR interaction with global adaptive timesteps.

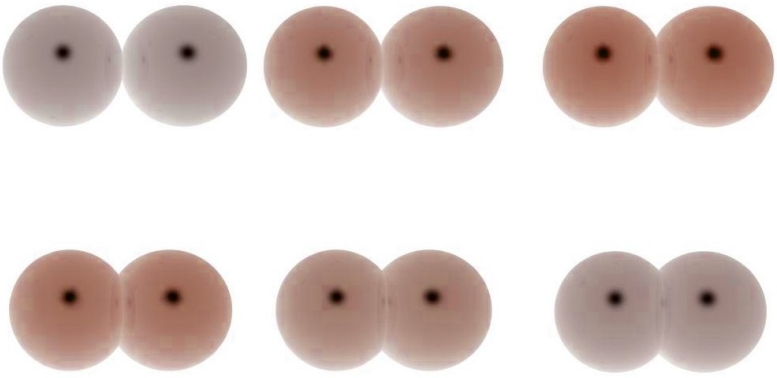

(b) Simulation of two cells under JKR interaction. Red colouring corresponds to higher cell velocities.

Figure 4.1: **(a):** Simulation of two cells with different initial distances separating due to JKR interaction. Cells move into the JKR equilibrium distance, where the resulting force between them is zero. Note the markers which show the global adaptive timestep algorithm at work, limiting the displacement to $dx_{max} = 0.25\mu m$ per timestep. Therefore in regions with higher slope the marker density is increased on the same curve corresponding to a smaller timestep. **(b):** Simulation of two cells under JKR interaction starting at normalised distance of $\chi = d/2r_{cell} = 0.99$ (first contact - corresponding to the upmost curve in the left figure). Red colouring corresponds to higher cell velocities. Timesteps of 90 s starting in the upper left corner at $t = 0$ and $\chi = 0.99$ until equilibrium is reached at $\chi \approx 0.7$ (bottom right).

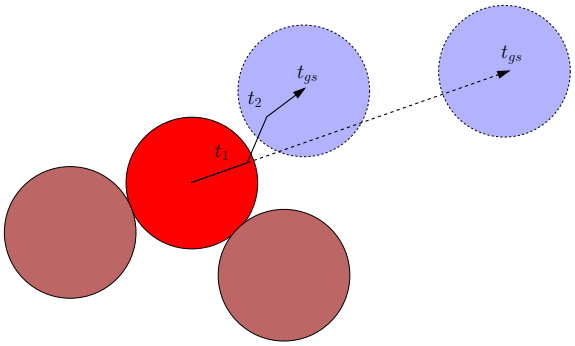

Figure 4.2: Basic concept of the local adaptive treatment for cells. If the cell velocity exceeds the $v_{ave}f_{ave}$-threshold it is not propagated to the according position (indicated by the dashed arrow) but instead displaced multiple times according to the global maximum displacement Δx. Surrounding cells are assumed to be static in an adiabatic approximation.

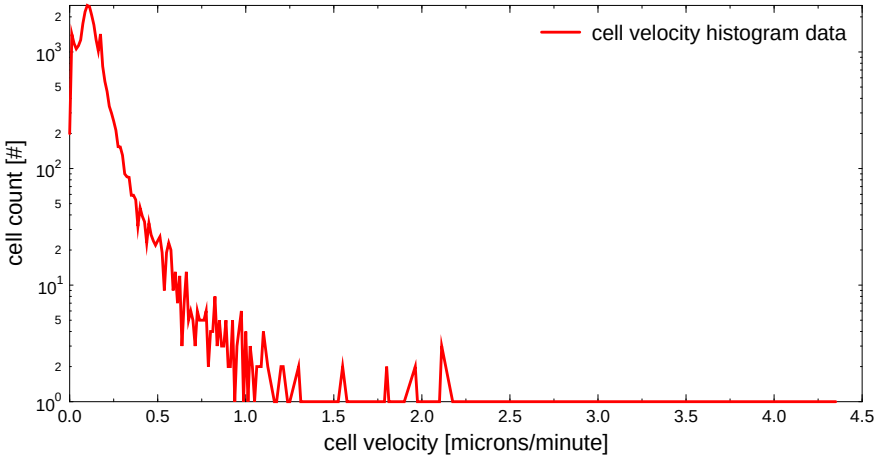

Figure 4.3: Typical velocity profile of a multicellular tumour spheroid in simulation. Compare figure 9.1 for the velocity distribution throughout a tumour spheroid. Note that few fast mavericks exceed the typical cell velocities by orders of magnitude. The average cell velocity is used as threshold for the local adaptive treatment. It can be shifted as described in equation 4.12 with help of the factor f_{ave}.

average velocity of cells, it can be assumed that their surrounding does not change during their asynchronous treatment.

The application of a local adaptive stepsize algorithm as described in equation 4.12 results in a great increase in simulation performance, as shown in figure 4.4.

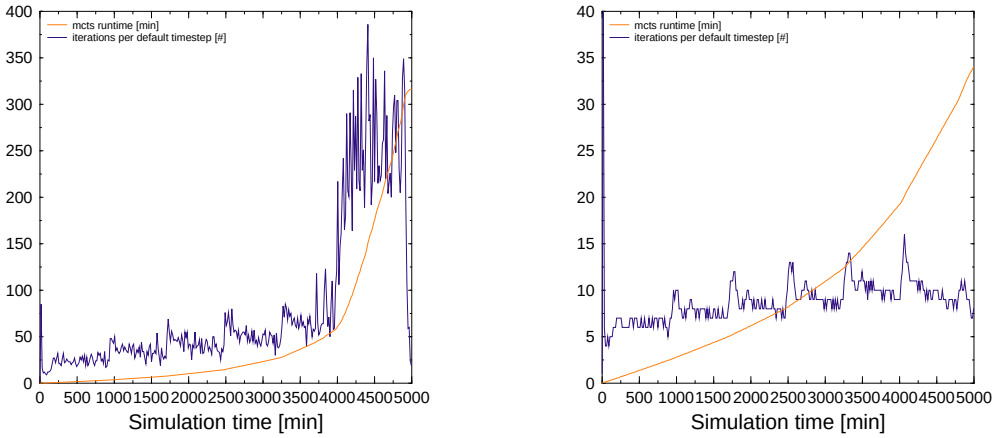

(a) Algorithmic simulation efficiency without local adaptive treatment.

(b) Algorithmic simulation efficiency including local adaptive treatment.

Figure 4.4: Local adaptive treatment of the fastest cell agents results in an tenfold decrease in computational time for a typical setup. Number of global adaptive timesteps needed to advance the simulation for one default timestep in purple, total runtime in orange. Note the decrease in the number of iterations right from the start in b). Even large cell numbers with numerical unfavourable cell interactions do not increase the computational effort in run b) significantly compared to a). See figure 4.5 for statistics of this simulation run.

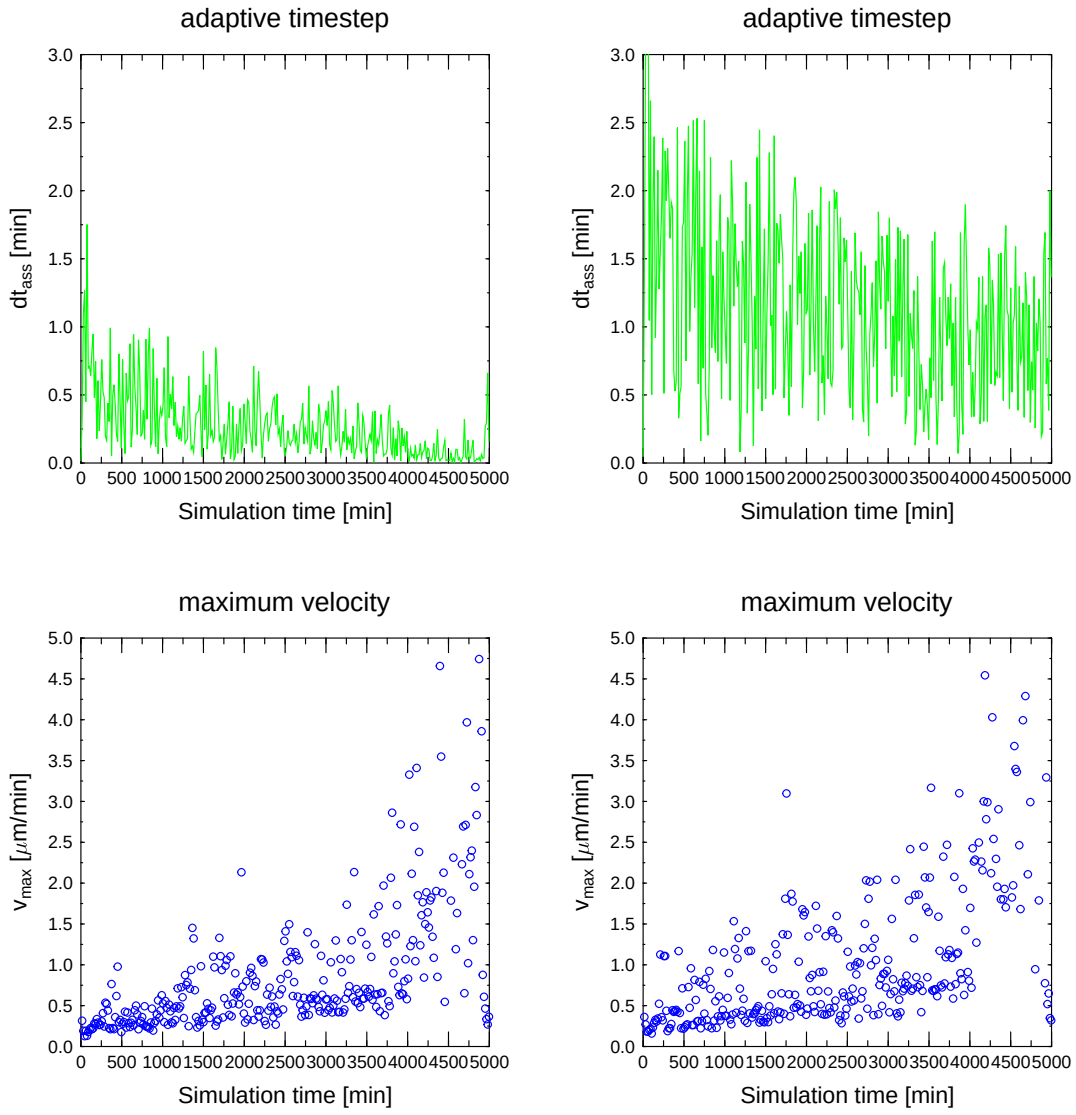

(a) Simulation statistics without local adaptive treatment.

(b) Simulation statistics including local adaptive treatment.

Figure 4.5: With local adaptive treatment a decrease of the default timestep is only necessary for faster cell agents. Although the top cell velocities are similar to run a) note the much higher adaptive timestep used to propagate the majority of cell agents when local adaptive treatment is used in run b). This results in a tenfold decrease of simulation runtime, as shown in 4.4.

5 Cell cycle and metabolism

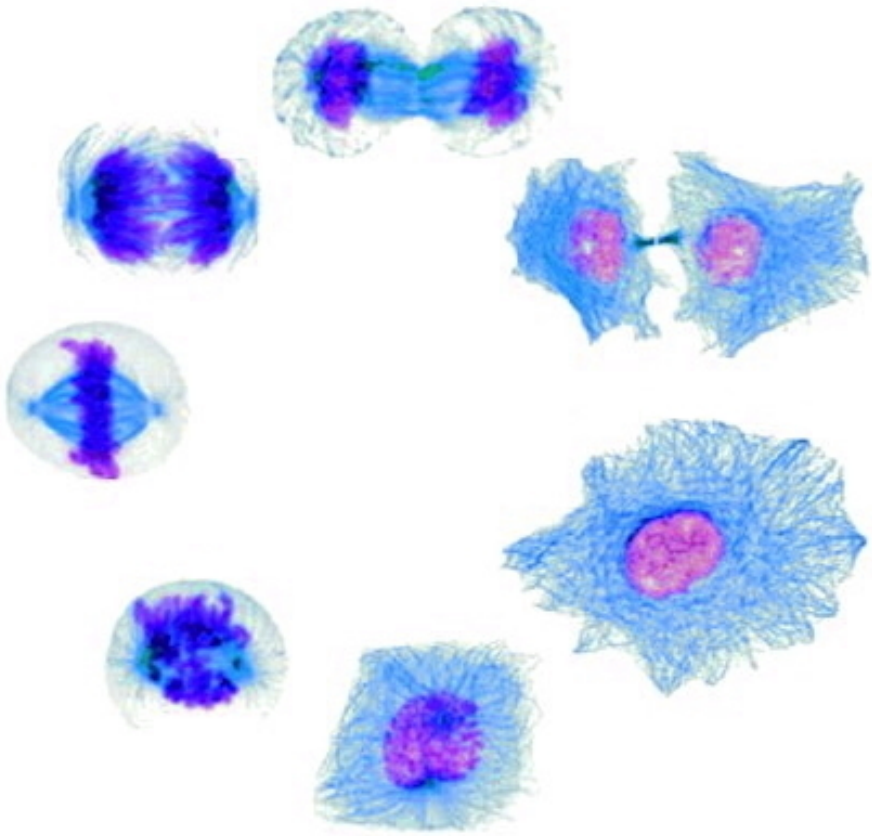

Figure 5.1: The cell cycle: microtubules stained blue, genetic material in purple. From `www.cbp.pitt.edu/faculty/yong_wan/`

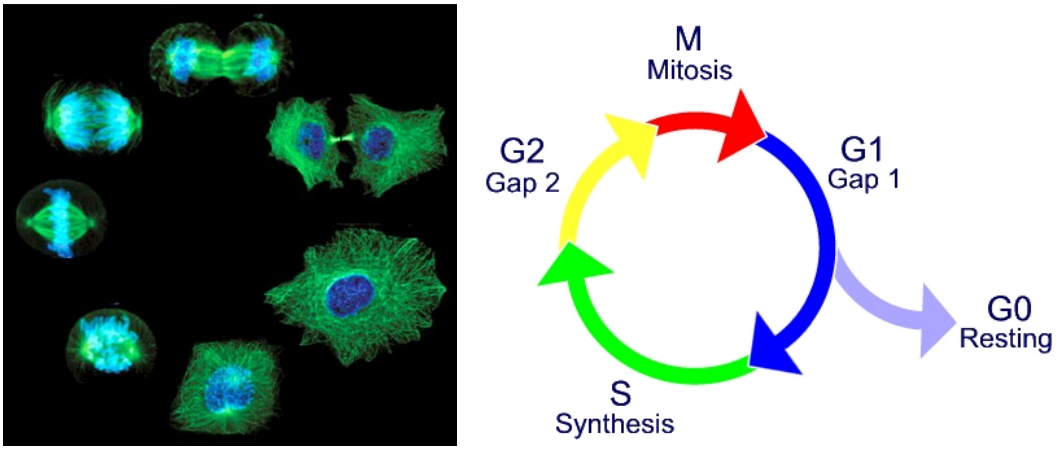

(a) (b)

Figure 5.2: **(a)** The cell cycle in vivo: microtubules stained green, genetic material in blue. From `www.cbp.pitt.edu/faculty/yong_wan/`. **(b)** Schematic visualisation of the cell cycle phases.

5.1 The life and death of a cell

During its lifespan a cell undergoes multiple repetitions of a characteristic cycle of distinct functional phases known as the cell cycle. The first three of these phases are subsumed under the name of interphase, in which the cell prepares itself for the initiation of cell division. Tthe fourth phase, in the active part of the cycle, is the mitotic phase, in which the mother cell divides into two daughter cells, which begin the cell cycle anew. A fifth phase exists in which fully differentiated cells, senescent cells or cells in unfavourable environments reside. This phase is characterised by inactive behaviour in respect of the cell cycle.

The cell cycle

G1 Phase

Gap/growth phase 1 or short G_1 is characterised by high biosynthetic activities of the cell. Cells grow in size in response to mitogenic signals, such as soluble extracellular growth factors. Thy synthesis of various enzymes which are required in the S phase is performed. Protein kinases (PKCs), enzymes which catalyse the addition of phosphate to other proteins (phosphorylation), are activated. The cyclin dependent kinases (CDKs) are a group of such protein kinases whose activity is central to this process (see section 5.1).

The first group of cyclins to become activated are the D-type cyclins, which bind and activate CDK4 or CDK6. The active cyclin D/CDK4-6 enzyme phosphorylates Rb, the retinoblastoma protein, which impedes its ability to bind and inactivate transcription factors. These factors, such as E2F-1, when released from Rb, bind to the promoter regions of specific genes, resulting in increased RNA transcription.

The duration of G_1 may vary on a large scale (more details on the cell cycle control can be found in *Morgan* (2007)).

The Restriction Point

At the end of G_1 cells have to pass the regulative tests at the so-called restriction point, where the decision is made on whether the cell should continue in the cell cycle or pause in G_0. Due to its importance for growth regulation, the mechanisms of the restriction point are treated in full detail in the next section.

S-Phase

During synthesis phase (or short S phase) the DNA stored in the chromosomes is exactly replicated through the activity of a family of enzymes including the DNA polymerases. When all of the chromosomes have been replicated, each chromosome has two identical sister chromatids. Thus, during this phase, the amount of DNA in the cell is effectively doubled, though the ploidy of the cell remains the same. Except for the histone production the rates of RNA transcription and protein synthesis are very low during this phase. The duration of S phase is relatively constant among cells of the same species.

S phase can easily be distinguished from other phases by the ability of the cell to stably incorporate fluorescently or radioactively tagged nucleotides, the building blocks of DNA, into their chromosomes. To activate the replication machinery cells depend on the protein kinase activity cyclin A coupled to CDK1 and CDK2.

G2 Phase

After verifying the exact copy of the genetic information, the cell enters the gap/growth phase 2 or short G_2, which lasts until the cell enters mitosis. Activity of the mechanisms responsible for protein synthesis rises again during this phase. Especially microtubule-synthesis plays an important role in the preparation for mitosis. Inhibition of protein synthesis during G2 phase prevents the cell from undergoing mitosis.

CDK1 (a.k.a. cdc2) replaces CDK2 as the predominant cyclin and it couples with either Cyclin A or one of the B-type cyclins to catalyse the phosphorylation of proteins specific to the G2 and M phases of the cell cycle.

G2 checkpoint

The G2 checkpoint initiates or prohibits the entry into mitosis, depending mainly on the Mitosis Promoting Factor, MPF.

Mitosis

Mitosis (or short M phase) is the phase of the cell cycle in which cells leave the preparing interphase and eventually divide physically into two separate daughter cells.

The mitotic phase itself is usually subdivided in four distinct phases, namely prophase, metaphase, anaphase, and telophase. Since this further distinction is of no importance for this thesis and could well be the topic of a whole series of books itself, this division is neglected here.

The relatively short M phase consists of two functional processes: nuclear division

(karyokinesis) and cytoplasmic division (cytokinesis). During karyokinesis the doubled information stored in the DNA is equally divided in two parts, one for each daughter cell. In order to do so, first the nuclear membrane is dissolved (which later reforms, once cell division is complete). The chromosomes condense into compact structures and are then aligned in the future plane of separation called the metaphase plate. Microtubules splay out from opposite ends of the cell, attach themselves to the chromosomes kinetochores (amphitelic attachment) and shorten, pulling apart the sister chromatids of each chromosome such that each half of the cell gets exactly one copy of the DNA. A new nuclear envelope forms around the separated sister chromosomes. Although there are control mechanisms which prohibit further advance through mitosis upon attachment or separation errors, syntelic attachment (when microtubules from the same pole bind to both sister kinetochores) occurs – especially in cancerous cells – which results in one daughter cell inheriting multiple copies of a chromosome (aneuploidy).

At the completion of mitosis, cells undergo cytokinesis, or separation into two halves. Actin and Myosin-II form a band around the cell waist and generate local tension. This band gradually constricts like a belt until the cell pinches in two.

The B-type cyclins remain active throughout M-phase, but their activity immediately ceases once cell division is complete and the two daughter cells once again enter G1.

Quiescence (G0 Phase)

Post-mitotic cells reside in a phase called G_0, which includes both quiescent and senescent cells. These cells are non-proliferative and may remain quiescent for long periods of time, possibly indefinitely. In fact most cells in an adult body are in quiescence, neurons and skeletal muscle cells even being in a terminally differentiated G_0 state. However, most of the cells in G_0 can reenter the cell cycle if the right conditions are met (mitogenic signals available, nutrient supply sufficient etc.). Cells which do not receive mitogenic signals in G_1 may enter G_0 due to CDK inhibition. Cellular senescence leading to G_0 can occur in response to severe DNA damage or degradation, and is sometimes used as an alternative to self-destruction of such a damaged cell by apoptosis.

The metabolic demands of G_0 phase vary according to the specialised functions being carried out by the quiescent cell, but there is often lower levels of gene expression, macromolecular biosynthesis and energy consumption compared to actively dividing cells.

Regulation of the cell cycle through growth factors and CDKCs

In healthy tissue the cell transitions sequentially through the cycle phases in response to regulatory signals and growth factors. These are specific proteins which are capable of stimulating proliferation and differentiation in a distinct type of tissue. Commonly known families of growth factors include

FGF (Fibroblast Growth Factor) promoting angiogenesis, wound healing, and embryonic development

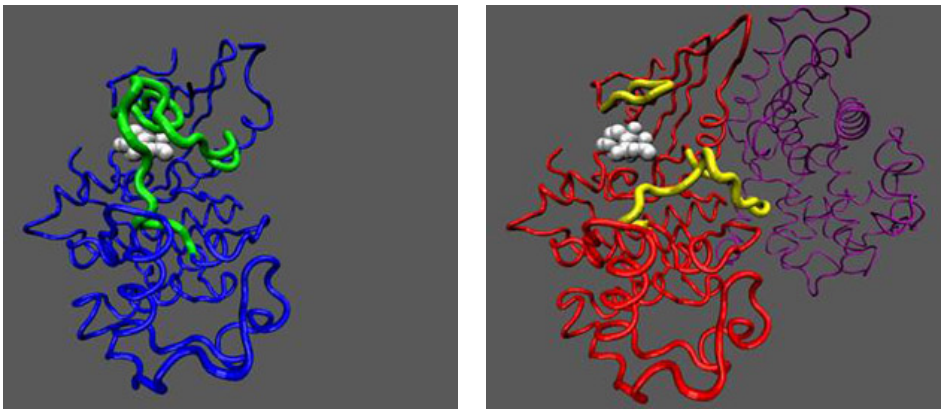

(a) (b)

Figure 5.3: **(a)** Cdk 2 (blue) and the complex of Cdk 2 (red) and Cyclin A (purple) (**(b)**). The active centre and the associated ATP-molecule are shown in white. The loops of Cdk 2 which move furthest when binding Cyclin A are stained in colour (green for inactive, yellow for active) showing the effect of the conformation change upon binding on the active centre of Cdk 2. Image source `http://www.molekuelkueche.de/img/molecularModeling/Cdk2_CycA(inactive).jpg`

VEGF (Vascular Endothelial Growth Factor) promotes blood vessel differentiation in vasculogenesis and angiogenesis

EGF (Epidermal growth factor) important for regulation of cell growth, proliferation, and differentiation - increases cancer risk (see *Herbst* (2004))

Diffusion of growth factors in the system can be included in the simulation through modelling their concentration on a diffusion grid. Molecular networks can couple these growth factors to the cell cycle progression.

Another source of regulating signals was discovered only recently. In 2001 the Nobel Prize in Physiology or Medicine was awarded jointly to Leland Hartwell, Tim Hunt and Paul Nurse for their discoveries of "key regulators of the cell cycle". Using genetic and biochemical methods, they identified the molecules CDK and cyclin that control the cell cycle in eukaryotic organisms. The CDKs (cyclin dependent kinases) bear their name because their activity requires binding to a protein partner, a cyclin, whose levels of expression and activity vary depending on the phase of the cell cycle (see figure 5.3 for the structure of CDK2 during binding). The bound CDK and cyclin form a cyclin-dependent kinase complex (CDKC) which phosphorylates other compounds under consumption of ATP. CDKC function depends on the type of cyclin attached to CDK, therefore the cell cycle progression can be regulated by the type of cyclin present (see figure 5.4).

Cell cycle checkpoints mediated through CDKs

Cell cycle checkpoints are control mechanisms that ensure the fidelity of cell division in eukaryotic cells. These checkpoints verify whether the processes at each phase of the cell

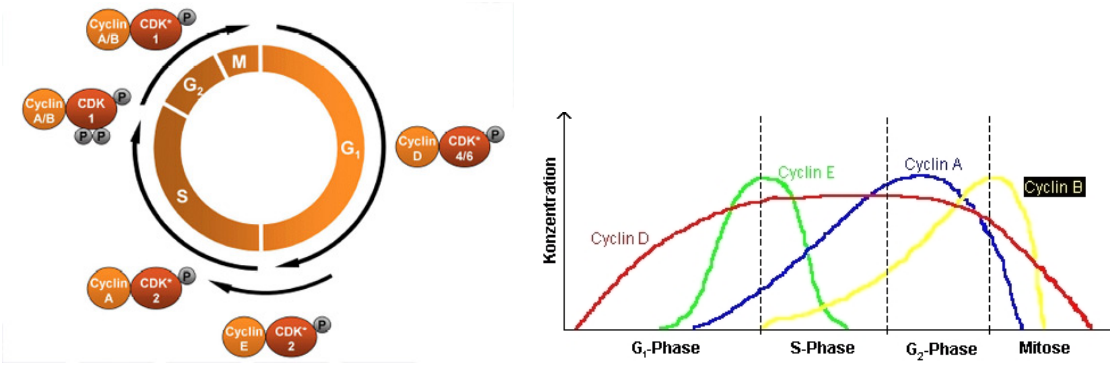

(a) (b)

Figure 5.4: **(a)** CDK and cyclin are key molecules that control and coordinate DNA-synthesis, chromosome separation and cell division. CDK and cyclin together drive the cell from one cell cycle phase to the next. **(b)** Cyclin type and amount vary throughout the cell cycle.

cycle have been accurately completed before progression into the next phase. Progression is typically prevented through negative signalling and, if necessary, repairs are initiated (e.g. in the case of DNA damage)

Several checkpoints are designed to ensure that damaged or incomplete DNA is not passed on to daughter cells. Two main checkpoints exist: the G1/S checkpoint and the G2/M checkpoint. The G1/S transition is a rate-limiting step in the cell cycle and is also known as restriction point.

The well known transcription factor p53 (also known as protein 53 or tumour protein 53) plays an important role in triggering the control mechanisms at both G1/S and G2/M checkpoints (see *Agarwal et al.* (1995) and *Taylor et al.* (1999)).

An important function of many checkpoints is to assess DNA damage, which is detected by sensor mechanisms. When damage is found, the checkpoint uses a signal mechanism to either stall the cell cycle until repairs are made or to target the cell for destruction via apoptosis. The same sensor-signal-effector mechanism seems to be in use for all assessment of DNA damage, which makes damage to these mechanisms highly carcinogenic.

G1/S Checkpoint (Restriction point)

Located at the end of the cell cycle's G1 phase, the restriction point marks the key decision whether the cell should divide, delay division, or enter a resting stage. Most cells stop at this stage and enter quiescence e.g. due to unfavourable environmental conditions. The restriction point is mainly controlled by action of the CKI-p16. This protein inhibits the CDK4/6 and ensures that it can no longer interact with cyclin D1 to cause the cell cycle progression. In growth induced or oncogenic induced cyclin D expression, this checkpoint is overcome because the increased expression of cyclin D allows its interaction with CDK4/6 by competing for binding. Once active CDK4/6-cyclin D complexes form, they phosphorylate the tumour suppressor retinoblastoma (Rb) and this relieves the inhibition

of the transcription factor E2F. E2F is then able to cause expression of cyclin E, which interacts with CDK2 to allow for G1-S phase transition. Therefore, reentry into the cell cycle can be achieved by growth factor induced expression of cyclin D proteins.

The existence of a restriction point can be demonstrated by depriving cells from growth factors in their medium. Many types of cells will continue to complete a single cell cycle if they are in S-phase, G2 or Mitosis, but will then arrest in the next G1 phase.

G2/M Checkpoint

The second checkpoint is located at the end of G2 phase, triggering the start of the M phase (mitosis). In order for this checkpoint to be passed, the cell has to check a number of factors to ensure the cell is ready for mitosis. The CDKs associated with this checkpoint are activated through phosphorylation by the action of a Maturation promoting factor (or Mitosis Promoting Factor, MPF).

The molecular nature of this checkpoint involves an activating phosphatase, known as Cdc25, which under favourable conditions removes the inhibitory phosphates present within the MPF complex. If the DNA is damaged prior to mitosis, the cell cycle is arrested via inactivation of the Cdc25 phosphatase to prevent transmission of damage to daughter cells.

Anaphase Checkpoint

The mitotic spindle checkpoint occurs at the point in metaphase where all the chromosomes should have aligned at the mitotic plate and be under bipolar tension. The tension created by this bipolar attachment is what is detected and what initiates the anaphase entry. Degradation of cyclin B ensures it no longer inhibits the anaphase promoting complex, which in turn is now free to break down securin.

Telomere shortening and cell mortality

A single cell can divide a number of times up to the Hayflick limit, after which the cells telomere reaches a critical length. Human cells in a cell culture divide about 52 times before entering a senescence phase (entering G_0). During each mitosis the telomere appendix on the DNA is shortened in the replication process, acting as a kind of inner clock for the cell. This limited division capability protects the organism from cancerogenesis as the possibility for a cell to acquire the necessary mutations for uncontrolled growth is limited with its active lifespan. Since the telomere is essential for safe DNA replication, sending the cell into senescence upon reaching a critical length is also a protective mechanism against genomic instability.

Many stem cells, as they are undifferentiated, are not affected by the Hayflick limit. They exist in every tissue and may continue reproducing for the lifespan of the organism, thus replenishing the pool of “mortal”, fully differentiated cells. Cells which divide without

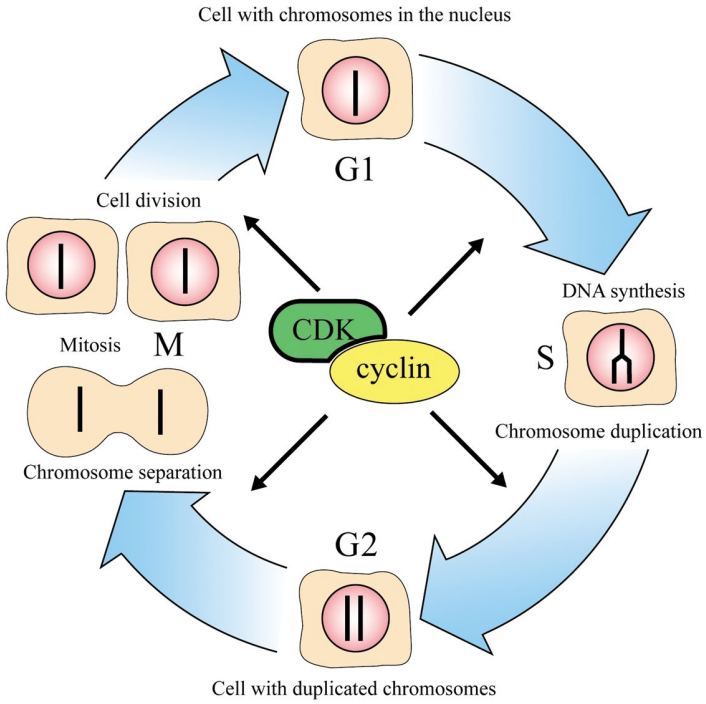

Figure 5.5: CDK and cyclin regulate the progression through the cell cycle.

limit usually express the telomerase enzyme or use other mechanisms to lengthen their telomere. These methods are also used by cancer cells to divide uninhibited.

Death of a cell - Necrosis vs. Apoptosis

As cells inside a multicellular organism exist in a social fabric it is inevitable for them to provide a mechanism for self-destruction to be used if they threaten the welfare of the tissue. This mechanism is called apoptosis and is of great use to eliminate a cell which is no longer capable of dividing safely e.g. due to severe DNA damage. It is important to note that apoptosis needs a distinct enzymatic pathway, which is often disabled in malignant cells due to oncogenreferredic mutations. Extreme environmental conditions or damage of the apoptotic pathway may lead to cells dying without any regulation. This process is called necrosis and is hazardous for the complete tissue through inflammatory effects. Both processes are described in detail in the following sections.

Apoptosis as programmed cell death (PCD)

Apoptosis is often also referred to as the “physiological death of the cell”. It is the regulated mechanism used by the body to dismantle unneeded cells. Apoptosis means “falling off” in Greek, and this name holds true since it is the cellular suicide commando. In general, apoptosis is associated with benefits for the whole organism. Prominent examples include the sculpting of digits by apoptosis of cells between the digits during early ontogenesis

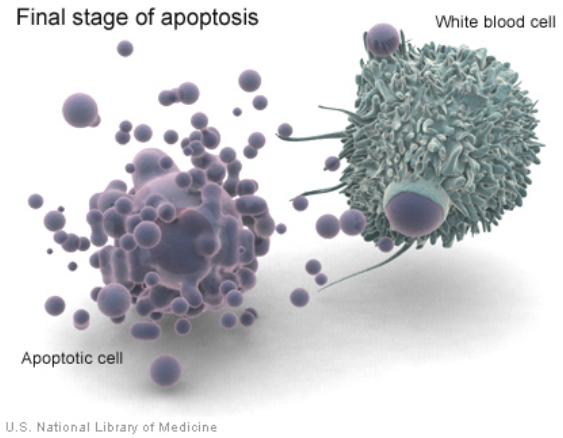

Figure 5.6: An apoptotic cell breaking away into apoptotic bodies which are phagocytised by a macrophage. Picture in public domain by the US National Library of Medicine.

and the renewal of the bone marrow and intestine (which kills billions of cells by apoptosis in a healthy adult in every hour). Furthermore, cell death helps to regulate cell numbers and maintain homeostasis, as a counterweight to cell division. The mode of apoptosis ensures a secure recycling of the dying cell's parts. Two important examples of the direct initiation of apoptotic mechanisms in mammals include the TNF-induced (tumour necrosis factor) model and the Fas-Fas ligand-mediated model, both involving receptors of the TNF receptor (TNFR) family coupled to extrinsic signals.

The process of apoptosis can be subdivided into several characteristic steps:

- breakdown of the proteinaceous cytoskeleton by caspases; cell shrinkage and rounding
- chromatin condensation into compact patches (pyknosis)
- nuclear envelope discontinuities and DNA fragmentation (karyorrhexis)
- high levels of endonuclease activity, degradation of DNA
- irregular buds (blebs) in the cell membrane
- cell breaking apart into vesicles called apoptotic bodies
- phagocytosis of apoptotic bodies by immune agents (depicted in figure 5.6)

A main application of apoptosis are cells which are damaged beyond repair, infected with a virus, or undergoing stress conditions such as starvation. Safe elimination of those cells is of importance for the whole tissue.

Therefore, apoptosis plays a prominent role in cancerogenesis: if a cell is unable to undergo apoptosis, due to mutation or biochemical inhibition, it can start to divide excessively and develop into a tumour. For example, the infection with papillomaviruses causes a viral gene to interfere with the cell's p53 protein of the apoptotic pathway. This interference in the apoptotic capability of the cell plays a critical role in the development of cervical cancer. For more details on the interplay between apoptosis, cancer development and treatment response see *Brown and Attardi* (2005).

Pathological death of cells: Necrosis

Necrosis occurs when cells die of extreme changes in the physiological conditions. It is, therefore, also referred to as "unnatural death" of cells and living tissue. It can be induced by a variety of external factors, such as thermal changes (extreme heat or cold or fast temperature fluctuations), chemical factors (lack of oxygen or existence of toxic substances), infection with lytic viruses or activation of the complement system.

In total, necrosis has no advantage for the organism as the uncontrolled release of intracellular content after plasma membrane rupture is the cause of inflammations. Lysic enzymes released by this rupture start to degrade neighbouring cells which can lead to further necrotic deaths. In addition, the cleanup of cell debris by phagocytes is difficult, as the disorderly death generally does not send cell signals which tell nearby phagocytes to engulf the dying cell. This lack of signalling makes it harder for the immune system to locate and recycle dead cells which have died through necrosis than those that have undergone apoptosis. Necrosis follows a typical scheme:

- cell swelling due to loss of the selective action of the plasma membrane and osmotic inflow
- chromatin digestion
- disruption of the plasma membrane and organelle membranes
- DNA hydrolysis, organelle breakdown
- cell lysis

Necrosis plays an important role in the development of tumour spheroids (*Bell et al.* (2001)) and necrotic waste materials might have a strong effect on the surrounding tissue by inducing apoptosis, calling immune agents to the site or other mechanisms. This can be modelled by keeping track of toxic necrose waste products on a separate diffusion grid within a simulation.

Stem cells and the maintenance of homeostasis

Tissues in multicellular organisms are always on a fine line between exuberant growth and extinction. They must maintain a viable cell count in order to fulfill their duties. Maintenance of homeostasis is therefore a property of living organisms, regulating their internal environment so as to maintain a stable, constant condition. In a tissue this translates into keeping a nearly constant number of cells by balancing cell division and cell death.

Most cells in an organism cease to divide after they are terminally differentiated. Depending on the type of tissue they may:

- go into permanent quiescence (e.g. neurons)

- reenter the cell cycle under certain conditions (e.g. liver cells)
- stay active almost all the time (e.g. intestine)

In healthy tissue the cell population is replenished by stem cell division (symmetric or asymmetric (see *Dingli et al.* (2007) and *Huntly and Gilliland* (2005))). At the same time homeostasis is maintained with the help of apoptosis.

5.2 Implementation of the cell cycle for simulation agents

In order to capture the behaviour of cells in a simulation, the mechanisms of the cell cycle as described in the previous sections were implemented in a `cell`-class within this thesis. The basis for this is the agent-based representation of cells (see section 2.2) within an object-oriented programming language such as C++. This section will introduce the chosen implementation.

Insertion of cells at simulation start

Basic information about each cell is stored within its state vector. This vector of variables contains information such as the current cycle phase and the remaining phase length (see also section 8.1 on page 73). Member functions of the cell handle the regulation of the cell cycle progress. phase length At the initialisation of a simulation run, a predetermined number of cells is inserted. Inserted cells can be marked as malign or benign and insertion is done using a Monte Carlo algorithm to obtain a chosen configuration (spherical e.g. malign cells surrounded by benign ones, mixed or pointwise). Upon instantiation cell agents are assigned a random phase (G_1, S or G_2), a random phaselength is drawn from a given distribution (e.g. Gaussian around a typical phaselength with given width) and an according size is calculated (initial size plus already performed growth). Simulations starting with few malignant cells will show an oscillating behaviour with respect to the overall cell cycle phases of cells since progression will be synchronised to large extents depending on the chosen parameters for the phaselength distribution. However, this oscillation is damped due to the partial randomisation of phaselenghts and other effects such as cell cycle arrest in G_0. Synchronisation is completely lost after a few cell cycles (as can be seen in figure 9.9).

Important cell cycle control functions

The cycle of each cell agent is controlled by the
`void check_phase ( double& dtass, Triangulator<double,Cell>& tri )`
function. It handles all of the cell's internal event triggering, growth and shrinking. Furthermore, it checks if the available nutrient concentration has fallen below the critical limit for cell necrosis. The remaining phaselength of a cell agent is decreased according to the

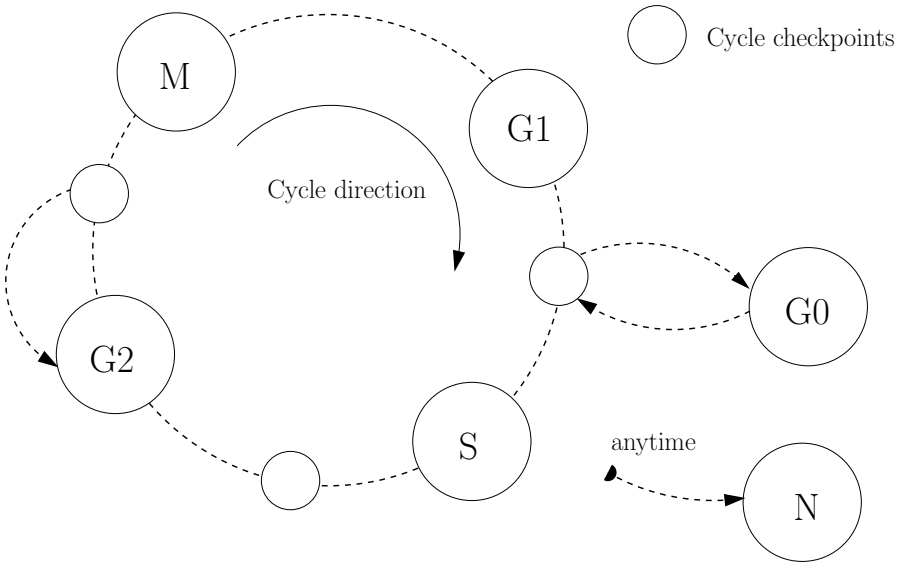

Figure 5.7: Sketch of the cell cycle as implemented in the simulation.

passed timestep `dtass`. If the remaining phaselength reaches zero, `check_phase` initiates a phase transition handled by the `void update_phase`-function.

`update_phase` includes all the cell cycle checkpoints described in the previous section. At the G_1/S-transition the nutrient availability is checked on the diffusion grids `Soluble<double> DIFF_GLUCOSE` and `Soluble<double> DIFF_OXYGEN`. The cell can be sent into quiescence if a minimum nutrient threshold is not reached. Apart from the nutrient check, at the restriction point `update_phase` performs a check of the pressure on the cellular agent mediated by its neighbours, via the `check_mechanical_inhibition` function. If this pressure exceeds the threshold, cell cycle progression is delayed and the cell is sent into quiescence. All checkpoints can be disabled if i.e. entry into quiescence should only be possible by high pressure on a cell and not mediated by nutrient conditions.

If all checks done by `update_phase` are positive, the cell is advanced into the next cycle phase, changing its internal variables and drawing a new phaselength from the distribution via the `set_phaselength` function. So far no external growth signals are processed and the molecular network around the CDK4/6 inhibition is not taken into account directly for reasons of simplicity. However modelling the cyclin interaction is possible once a molecular network is coupled to the `update_phase` function.

S phase is characterised by the replication of the DNA. This is mainly an internal process of the cell without impact on the tissue. DNA replication can be marked as incorrect with a certain probability, forcing the cell to prolong S phase or go into quiescence until repairs were successful. As DNA replication is a highly accurate process this mechanism is not used by default.

In G_2 the cell grows to reach its final size for mitosis. The G_2/M-transition is accompanied by a DNA damage checkpoint. If the cell is marked as damaged (e.g. by the `irradiate` function) repairs are initiated that succeed with a defined probability. Upon

success of the DNA repair the cell enters mitosis. If repairs are unsuccessful, the cell stays in G_2 phase attempting further repairs. Upon failure of a determined number of repair attempts, the cell is sent into senescence or apoptosis if possible. If the cells DNA was not damaged at the G_2/M checkpoint the cell enters mitosis immediately. Until now Cdc25 dynamics and the Mitosis Promoting Factor, MPF are not taken into account directly. This is feasible in the same way as for the G_1/S checkpoint, through the coupling of a molecular network to the cell. The MPF activates the CDK in response to environmental conditions being right for the cell, and allows the cell to begin DNA replication.

Upon initiation of mitosis the `update_phase` function calls the `proliferate` function to handle cytokinesis. Karyokinesis is taken to be an fully internal process of the cell. However, an anaphase checkpoint can be inserted, halting the progression through mitosis in the beginning due to an attachment error of the chromosomes with a defined probability.

Quiescence of a cell in G_0 is associated with a predetermined phaselength decreased by the `check_phase` function. At zero phaselength the `update_phase` functions checks for nutrient availability and cell pressure. If both checks are positive the cell is re-entered into the cycle exactly where it was sent into G_0, but if one of the checks is negative quiescence is prolonged. Cells which have been flagged as senescent due to irreparable DNA-damage or terminal differentiation stay in G_0 for unlimited time.

Necrosis is determined by a given phaselength during which the cell will shrink constantly (handled by the `check_phase` function) and eventually be deleted from the simulation. Toxic or hazardous products of necrosis can be modelled on the `Soluble<double> DIFF_NECROSIS` diffusion grid such as lysic enzymes. If their concentration is above a certain concentration threshold, neighbouring cells can be affected.

Sample cycle

always nutrients checked and necrosis initiated if below necrosis threshold

G1 phase growth with constant rate

G1/S checkpoint nutrient check for G_0 threshold; pressure check

G2 phase growth with constant rate

G2/M checkpoint DNA damage check; stall and repair or send into senescence if all repair tries failed

Necrosis and apoptosis

Cells undergoing necrosis within the tumour volume are removed from the cell cycle. They are shrinked to a predefined end radius over the duration of the necrosis phaselength τ_{N}. After the expiration of their phaselenght they are removed from the simulation. It is assumed, that the necrotic debris of cells is removed through the decomposition by immuno-agents and diffusion. Effects of toxic substances or other chemicals produced

by cell necrosis, which might affect other cells, can be examined through modelling of their diffusing according to section 5.4. Due to the fact that the apoptotic pathway is commonly disabled in cancerous cells, apoptosis is generally not used within the simulation. Implementation is done similar to necrosis with the difference of a faster cell removal (through the activity of phagocytes) and the apoptotic cell acting as a minor nutrient source for the time of its degradation.

5.3 Consumption of nutrients

Cell respiration and metabolism

Each cell takes up nutrients in order to convert their biochemical energy into adenosine triphosphate (ATP) within the process of cellular respiration. The energy stored in ATP can then be used to drive processes requiring energy, including biosynthesis, locomotion or transportation of molecules across cell membranes.

Under normal conditions cells mainly generate energy from oxidative breakdown of pyruvate. Pyruvate is an end-product of glycolysis, and is oxidised within the mitochondria (see figure 5.8 for an comprehensive overview of the metabolic reactions involved). This process is called aerobic respiration and can be summarised in the simplified reaction:

Equation 4 (*Aerobic cell respiration*)

$$C_6H_{12}O_6 + 6O_2 \longrightarrow 6CO_2 + 6H_2O + E \tag{5.1}$$

$$\Delta Hc = -2880kJ \tag{5.2}$$

Through glycolysis and the Citric acid cycle (CAC), glucose is oxidised to CO_2 and water, yielding energy in the form of ATP. Aerobic respiration requires oxygen in order to generate energy (ATP) because pyruvate needs to be fully oxidised (Krebs cycle) in the mitochondria.

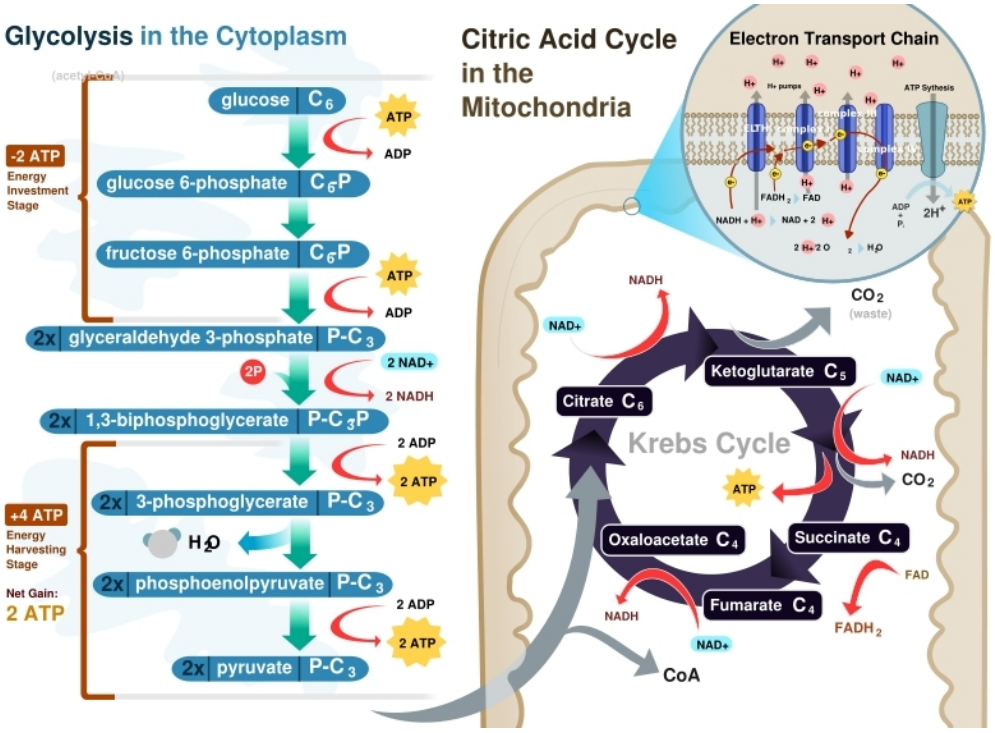

Figure 5.8: Cellular respiration including glycolysis, Krebs cycle, citric acid cycle, and the electron transport chain. From `http://upload.wikimedia.org/wikipedia/commons/7/74/CellRespiration.svg` under terms 3.

Under unfavourable oxygen conditions pyruvate is not metabolised by cellular respiration, but undergoes a process of substrate phosphorylation. This is a fast but rather inefficient process.

Equation 5 (*Anaerobic cell respiration*)

$$C_6H_{12}O_6 \longrightarrow 2C_3H_6O_3 + E \tag{5.3}$$

$$\Delta Hc = -120kJ \tag{5.4}$$

In this anaerobic respiration, pyruvate is not transported into the mitochondrion but fermented in the cytoplasm. A common waste product of this process is lactic acid in muscle cells. Alcohol produced in yeast fermentation is also produced within this process (ethanol fermentation).

As the aerobic metabolism is about 19 times more efficient than anaerobic metabolism (compare equations 5.2 and 5.4), it is the preferred metabolic activity in eukaryotic cells. However, tumour cells may show deviations to this behaviour as a reaction to the anaerobic conditions usually found inside a tumour spheroid.

It is clear that tumour cells may use anaerobic respiration to survive inside hypoxic

cycle phase	**oxygen consumption rate** [amol/s]	**glucose consumption rate** [amol/s]
G_0	15	75
G_1	20	95
S	18	85
G_2	20	95
M	18	85
N	0	0
A	-5	-20
overall rate	20±5	95±10

Table 5.1: Cell cycle dependent nutrient consumption rates used in the simulation. As no data about the cell cycle dependency of these rates was available in the literature they are set by an educated guess to resemble the commonly reported level of biomolecule synthesis. Consumption rates are assumed to be negative for apoptotic cells since apoptotic bodies can be recycled. Basis for the estimation of the cycle dependent rates is an overall rate investigated in *Casciari et al.* (1992), *Kunz-Schughart et al.* (2000), and *Wehrle et al.* (2000).

conditions. This leads to the generation of lactic acid which surrounds the tumour with an acidic court.

Cell cycle dependent nutrient consumption

The nutrient consumption of a cell varies throughout the cell cycle phase. Quiescent cells tend to show lower levels of gene expression, macromolecular biosynthesis and therefore energy consumption compared to actively dividing cells. To capture this behaviour in the simulation, cells show a certain nutrient consumption rate according to their cycle phase as shown in table 5.1. As no data about the cell cycle dependency of these rates was available in the literature, they are set by educated guessing to resemble the commonly reported level of biomolecule synthesis. Furthermore, nutrient uptake rates depend on other parameters such as the nutrient availability itself and even the tumour spheroid size (see *Freyer and Sutherland* (1985) for evidence on a reduction in the rates of oxygen and glucose consumption of cells in EMT6/Ro spheroids during growth). However, these further mechanisms are not included in the implementation yet. The nutrient consumption rate of the cell is distributed to the nodes of the diffusion grid surrounding the cell position via trilinear interpolation by the `add_rate()`-function. The rates are cleared using the `clear_lattice_rate()`-function and updated in constant intervals to capture the changing cell positions and phases.

5.4 Nutrient modelling with reaction diffusion equations

Nutrient distribution inside the simulation volume can be modelled with the help of reaction diffusion equations (RDEs). Each diffusing substance (e.g. glucose and oxygen) is modelled on a separate reaction diffusion grid through the solution of partial differential

equations (PDE). The numerical representation of the PDEs solution is discrete in both time and space within a finite-differences approach.

Typical reaction-diffusion equations will be of the form:

Equation 6 (*Reaction-diffusion equation*)

$$\frac{\partial u}{\partial t} = \nabla \left[D(\boldsymbol{x}, t) \nabla u(\boldsymbol{x}, t) \right] + Q(\boldsymbol{x}, t) \,, \tag{5.5}$$

with $u(\boldsymbol{x}, t)$ being the local concentration of a soluble,
$D(\boldsymbol{x}, t)$ the local diffusion coefficient and
$Q(\boldsymbol{x}, t)$ as reaction term (source or sink for the soluble under consideration).

Complex diffusion cases might be treated with a vectorial diffusion coefficient $\boldsymbol{D}(\boldsymbol{x}, t)$. However, in the cases to be solved within this thesis, scalar diffusion is sufficient.

There exists a range of applicable solvers for this type of reaction diffusion dynamics, which can be divided into implicit and explicit methods. Here the alternating-direction implicit algorithm (ADI) according to *Press et al.* (1994) is applied, where each propagation timestep is divided into several sub-steps and, during each sub-step, a single dimension is treated implicitly while the others are treated explicitly.

Spatial discretisation

Within the finite-difference approach, the spatial discretisation of equation 5.5 can be performed by dividing the system into disjoint volume elements V_i. Within these volume elements, one locally defines spatially averaged quantities by

$$u_i(t) = \frac{1}{V_i} \int_{V_i} u(\boldsymbol{x}, t) \, dx \tag{5.6}$$

The spatial derivatives occurring in the diffusion equation 5.5 can then be transformed into finite differences according to:

Definition 4 (*Spatial discretisation*)

$$\left. \frac{\partial u(\boldsymbol{x}, t)}{\partial \boldsymbol{x}} \right|_{\partial V_i \cap \partial V_{i'}} \rightarrow \frac{u_{i'}(t) - u_i(t)}{|\boldsymbol{x}_{i'} - \boldsymbol{x}_i|} \frac{\boldsymbol{x}_{i'} - \boldsymbol{x}_i}{|\boldsymbol{x}_{i'} - \boldsymbol{x}_i|} \,, \tag{5.7}$$

where $\boldsymbol{x}_i$ denotes centres of the volume element V_i.

Time discretisation

The reaction-diffusion equation 5.5 has to be discretised in time as well as space in order to be suitable for the application of a numerical solving algorithm. This can be achieved via

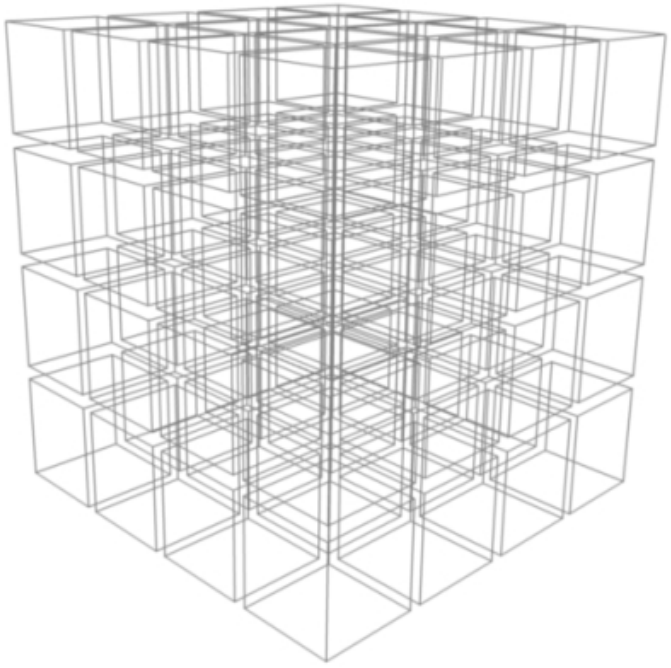

Figure 5.9: Finite difference approach: for spatial discretisation the computational domain is divided into disjoint volume elements V_I as described in equation 5.7. Introducing also a time discretisation according to equation 5.8 results in a fully discretised reaction-diffusion equation which can be solved by numerical algorithms.

Definition 5 (*Time discretisation*)

$$\frac{\partial u_I}{\partial t} \to \frac{u_I^{n+1} - u_I^n}{\Delta t}\,, \tag{5.8}$$

with $u_I^{n+1} = u_I^n(t + \Delta t)$ *and* $u_I = u_I(t)$,

where for rectangular lattices in three dimensions the index $I = \{i, j, k\}$ is a triple of indices, each one denoting the spatial position in one dimension. This definition of the time discretisation is symmetric around $t + \Delta t/2$.

Solution of the RDE

If the reaction volumes V_I are constant in time ($\frac{\partial V_I}{\partial t} = 0$), one can average equation (5.5) as described in equation (5.6). Using Gauss's theorem:

$$\int_V \nabla \boldsymbol{F}\, \mathrm{d}^{(n)}V = \oint_S \boldsymbol{F} \cdot \boldsymbol{n}\, \mathrm{d}^{(n-1)}S, \tag{5.9}$$

one obtains

$$\frac{\partial u_I}{\partial t} = \frac{1}{V_I} \oint_{\partial V_I} D(\boldsymbol{x}, t) \nabla u(\boldsymbol{x}, t) \cdot d\boldsymbol{f} + Q_I(t)\,, \tag{5.10}$$

The algebraic structure of the numerical discretisation depends on the specific geometry under consideration.

For the simplest and most common case of rectangular grids in three dimensions with

lattice constants Δx, Δy, Δz one can improve the accuracy by directly discretising (5.5)

$$\begin{aligned}\frac{\partial u_{i,j,k}}{\partial t} &= +\frac{(D_{i+1,j,k}-D_{i-1,j,k})\,(u_{i+1,j,k}-u_{i-1,j,k})}{4\Delta x^2}+D_{i,j,k}\frac{u_{i+1,j,k}-2u_{i,j,k}+u_{i-1,j,k}}{\Delta x^2}\\ &\quad+\frac{(D_{i,j+1,k}-D_{i,j-1,k})\,(u_{i,j+1,k}-u_{i,j-1,k})}{4\Delta y^2}+D_{i,j,k}\frac{u_{i,j+1,k}-2u_{i,j,k}+u_{i,j-1,k}}{\Delta y^2}\\ &\quad+\frac{(D_{i,j,k+1}-D_{i,j,k-1})\,(u_{i,j,k+1}-u_{i,j,k-1})}{4\Delta z^2}+D_{i,j,k}\frac{u_{i,j,k+1}-2u_{i,j,k}+u_{i,j,k-1}}{\Delta z^2}\\ &\quad+Q_{i,j,k}\,, \end{aligned} \tag{5.11}$$

which is second-order accurate[1] in space (*Bronstein et al.* (1997)). Equation 5.11 is only valid for the volume elements not residing on the boundary of the reaction volume. In these volume elements the boundary conditions (i.e. Dirichlet or von-Neumann) have to be discretised independently.

Within a Voronoi tessellation the simulation space is decomposed into disjunct volume elements V_I, for which every point within a volume element (Voronoi cell) is closer to a point called its generator $\boldsymbol{x}_I$ than to any other generator. The mechanisms of spatial tessellations, which are mentioned briefly in the following, will be introduced in detail in section 7.1. If one uses the Voronoi tessellation for the definition of volume elements V_I, equation 5.10 reduces to

$$\frac{\partial u_I}{\partial t}=\frac{1}{V_I}\sum_{J\in\mathcal{N}(I)}\frac{A_{IJ}}{|\boldsymbol{x}_I-\boldsymbol{x}_J|}(u_J-u_I)D_{IJ}+Q_I\,, \tag{5.12}$$

where V_I is the volume of the Voronoi cell I, and $J\in\mathcal{N}(I)$ denotes the next neighbours of cell I with generator $\boldsymbol{x}_I$. Consequently, the terms A_{IJ} denote the contact area of the adjacent Voronoi cells I and J. Linear interpolation on the connection lines between the generators of I and J yields for the diffusion coefficient

$$D_{IJ}=D_{J,I}=\frac{1}{2}D_I\left[1+\frac{\omega_J-\omega_I}{(\boldsymbol{x}_J-\boldsymbol{x}_I)^2}\right]+\frac{1}{2}D_J\left[1-\frac{\omega_J-\omega_I}{(\boldsymbol{x}_J-\boldsymbol{x}_I)^2}\right] \tag{5.13}$$

at the position of the Voronoi boundary. This reduces to the simple arithmetic average in case of equal weights $\omega_I=\omega_J$.

Within this thesis solution, modelling of the reaction diffusion equation on a grid as described by equation 5.11 was the method of choice. As the Voronoi boundaries of the cell are available from the triangulation of the cell system, an approach using equation 5.12 might be of great interest for further investigations.

A pseudo-steady-state approximation has been applied for the RDEs of the nutrients (see *Schaller* (2006)) as the diffusion coefficients of oxygen and glucose are orders of magnitude larger than typical random cell motilities. The nutrient concentrations are recalculated from the time-dependent cellular positions at fixed timesteps of $\Delta t_{diffev}=300s$, although

[1] The discretisation of the second derivatives can be derived by using a virtual grid with halved lattice constants.

this timestep is likely to be smaller as handled by the diffusion solver. The pseudo-steady-state approximation is justified because the diffusion length $L_{\mathrm{D}} = \sqrt{6D\Delta t_{diffev}}$ associated with the timestep and the smallest occurring diffusion coefficient (glucose in tissue) is larger than the largest spheroid radius observed during the agent-based simulations.

Linear operator form and solving strategies

The general handling of equations (5.12) and (5.11) differs in the way of discretisation. The equations can be written as

Definition 6 (*Linear operator form*)

$$\frac{\partial u_I}{\partial t} = \mathcal{L}u_I + Q_I(t)\,, \tag{5.14}$$

where $\mathcal{L}$ is a linear operator describing the geometry and diffusional properties of the system.

Equation 5.14 can be discretised in time accordingly to equation 5.8:

$$\frac{u_I^{n+1} - u_I^n}{\Delta t} = \mathcal{L}u_I^n + Q_I(t)\,, \tag{5.15}$$

with $u_I^{n+1} = u_I(t + \Delta t)$.

This linear operator form can be solved with different strategies:

- Forward-Time-Centred-Space (FTCS), Courant stable (see equation 5.17)
- Backward-Time-Centred-Space (BTCS), unconditionally stable
- Crank-Nicholson scheme (CNS), average of FTCS and BTCS, unconditionally stable

The simplest explicit scheme (Forward-Time-Centred-Space, FTCS) is realised by evaluating equation 5.15 at time t, i. e.,

$$u_I^{n+1} = \{\mathbb{1} + \Delta t\mathcal{L}^n\}u_I^n + \Delta t Q_I^n\,, \tag{5.16}$$

which has the advantage that the solution $u(t + \Delta t)$ can be readily obtained from $u(t)$ without necessitating matrix inversion. However, already for constant diffusion coefficients a von-Neumann stability analysis *Press et al.* (1994) on rectangular grids shows that this solution scheme becomes numerically unstable if

Definition 7 (*Courant-condition*)

$$\frac{D\Delta t}{\Delta x^2} + \frac{D\Delta t}{\Delta y^2} + \frac{D\Delta t}{\Delta z^2} \geq \frac{1}{2}\,, \tag{5.17}$$

a constraint which is known as Courant-condition.

Numerical instability implies that the numerical errors will increase exponentially in time, which is a serious limitation for practical applications. As the Courant condition involves both spatial (Δx) and temporal (Δt) resolutions, one can either decrease the timestep or decrease the spatial resolution to obtain correct numerical solutions with a method that is dependent on the Courant condition. An illustration of the underlying principle for equation 5.17 can be found in figure 5.10.

Numerical stability can be recovered if one applies a fully implicit scheme (Backward-Time-Centred-Space, BTCS), i. e., by evaluating 5.14 at time $t + \Delta t$ one yields

$$\left\{\mathbb{1} - \Delta t \mathcal{L}^{n+1}\right\} u_I^{n+1} = u_J^n + \Delta t Q_J^{n+1}\,, \tag{5.18}$$

which is still first order accurate in time. However, one can show by von-Neumann stability analysis that this scheme is unconditionally stable, i. e., timesteps larger than allowed by the Courant condition do not lead to an exponential increase of the numerical errors (*Schaller* (2006)). Note that the existence of $\mathcal{L}$ on the left hand side necessitates the inversion of a sparsely populated matrix.

ADI Algorithm

A method of choice is to combine the advantages of explicit and implicit algorithms by an average, i. e.,

Definition 8 (*Crank-Nicholson scheme*)

$$\left\{\mathbb{1} - \frac{\Delta t}{2}\mathcal{L}^{n+1}\right\} u_I^{n+1} = \left\{\mathbb{1} + \frac{\Delta t}{2}\mathcal{L}^{n}\right\} u_I^{n} + \frac{\Delta t}{2}\left(Q_I^n + Q_I^{n+1}\right)\,, \tag{5.19}$$

which is a sparsely populated linear system that can be solved for u_I^{n+1} with knowledge of u_I^n, Q_I^n, and Q_I^{n+1}. This method is referred to as the Crank-Nicholson scheme, and von-Neumann stability analysis shows that it is unconditionally stable for the free diffusion case (*Press et al.* (1994)). Furthermore, it is second order accurate in time, since here both the left and right-hand sides are centred at time $t_n + \Delta t/2$. The resulting system is tri-diagonal in one dimension, which enables a fast and simple algorithmic matrix inversion. This, however, does not hold true in higher dimensions. In this case, approaches such as operator splitting can help to reduce sparse matrices to several tri-diagonal ones (as shown in *Press et al.* (1994)).

For the two dimensional case the application of the alternating-direction implicit method (ADI) is demonstrated explicitly in *Press et al.* (1994). The basic idea is to divide each timestep into several sub-steps. Within each sub-step, a single dimension is treated implicitly, whereas the other dimensions are treated explicitly. In two dimensions, this procedure preserves unconditional stability, whereas in three dimensions the updating scheme from *Press et al.* (1994) can be generalised, $\mathcal{L} = \mathcal{L}_x + \mathcal{L}_y + \mathcal{L}_z$, to (reaction terms omitted)

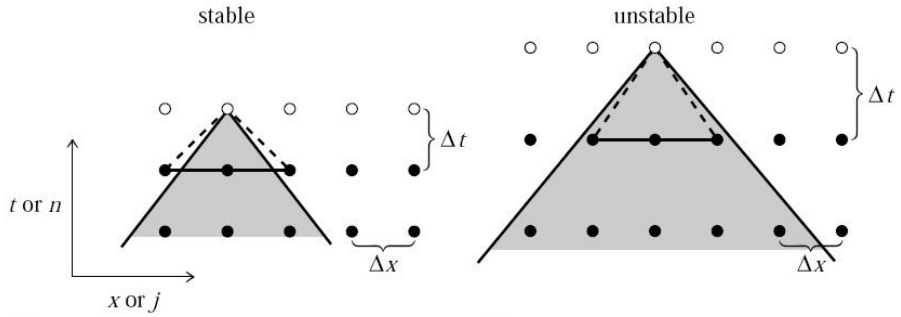

Figure 5.10: The Courant condition: A differencing scheme is stable if the solution to a problem at a point depends only on a differencing domain which is larger than the PDE domain. As the Courant condition (equation 5.17) involves both spatial (Δx) and temporal (Δt) resolutions, one can either decrease the timestep or decrease the spatial resolution to obtain correct numerical solutions with a method that is dependent on the Courant condition. Figure from *Press et al.* (1994).

Definition 9 (*Alternating-direction implicit method*)

$$\begin{aligned}
\left\{\mathbb{1} - \frac{\Delta t}{3}\mathcal{L}_x^{n+1/3}\right\} u_{i,j,k}^{n+1/3} &= \left\{\mathbb{1} + \frac{\Delta t}{3}\mathcal{L}_y^{n} + \frac{\Delta t}{3}\mathcal{L}_z^{n}\right\} u_{i,j,k}^{n}\,, \\
\left\{\mathbb{1} - \frac{\Delta t}{3}\mathcal{L}_y^{n+2/3}\right\} u_{i,j,k}^{n+2/3} &= \left\{\mathbb{1} + \frac{\Delta t}{3}\mathcal{L}_x^{n+1/3} + \frac{\Delta t}{3}\mathcal{L}_z^{n+1/3}\right\} u_{i,j,k}^{n+1/3}\,, \\
\left\{\mathbb{1} - \frac{\Delta t}{3}\mathcal{L}_z^{n+1}\right\} u_{i,j,k}^{n+3/3} &= \left\{\mathbb{1} + \frac{\Delta t}{3}\mathcal{L}_x^{n+2/3} + \frac{\Delta t}{3}\mathcal{L}_y^{n+2/3}\right\} u_{i,j,k}^{n+2/3}\,, \qquad (5.20)
\end{aligned}$$

which replaces a sparse system by three tri-diagonal ones. Unfortunately, the above splitting scheme sacrifices numerical stability at $D\Delta t/\Delta x^2 \geq 1/2$ (see *Schaller* (2006)). However, this drawback can be compensated by a solver implementation which automatically breaks the timestep down into sub-steps, in agreement with the Courant condition equation 5.17, as it is done within the solver employed within this thesis.

Realistic boundary conditions

Assuming that a tumour spheroid resides in a well stirred medium (in vitro) this can be modelled by Dirichlet type boundary conditions. Concentration on the nodes lying on the boundary of the diffusion grid is kept constant at the given value (e.g. 16.5 mMol glucose according to *Freyer and Sutherland* (1986)). Nutrients are assumed to diffuse in from an infinite reservoir outside the reaction cuboid. The type of boundary conditions, boundary concentrations and initial concentrations for an instance of the `soluble`-class are defined within the application's parameter file and passed on to the solver by the parameter parser. An example of a simulation run showing the nutrient concentration is shown in figure 5.11.

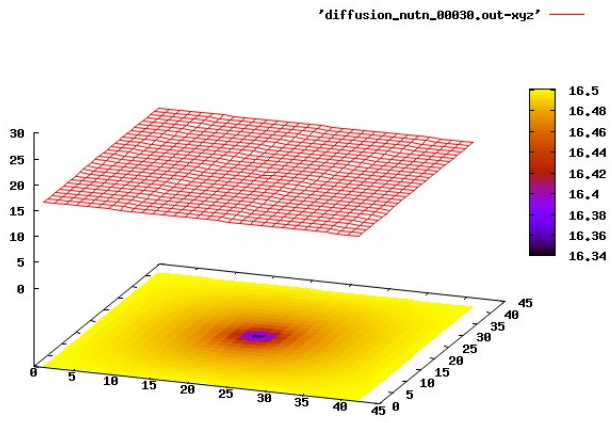

(a) Glucose concentration after 30 min of simulation.

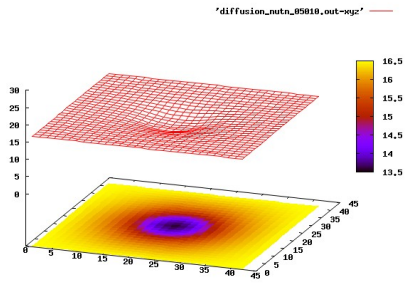

(b) Glucose concentration after 5000 min of simulation.

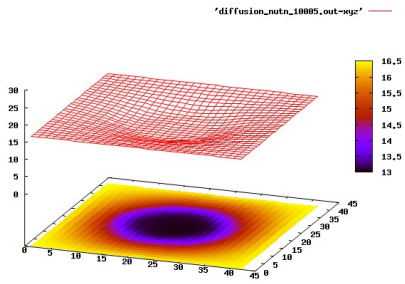

(c) Glucose concentration after 10000 min of simulation.

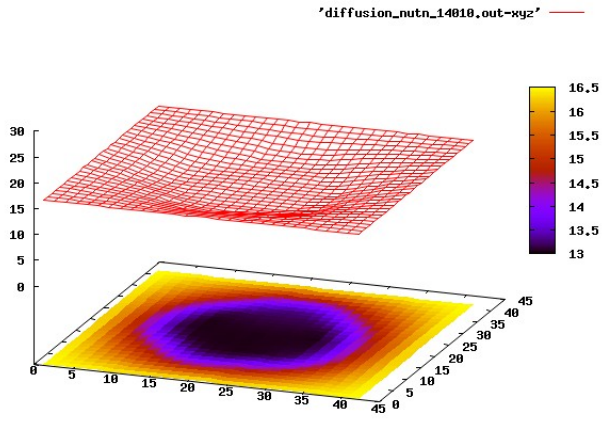

(d) Glucose concentration after 14000 min of simulation.

Figure 5.11: Solution of the reaction diffusion system as given by equation 5.10. Figures show a section through the middle of the reaction cuboid, x and y axis depict grid nodes while the z axis show the glucose concentration in *mmol*. The alternating-direction implicit method (ADI) as described in *Press et al.* (1994) was used to solve the system. Implementation is done in the `soluble`-class of the application. Initially the reaction cuboid is filled with a nutrient concentration of 16.5*mmol* glucose. This concentration decreases due to the fact that the growing tumour spheroid is consuming nutrients faster than the diffusive influx through the boundary can sustain.

6 Cytokinesis modelling

6.1 Cell division and the abrupt transition of cytokinesis

Having completed the growth and synthesis phases, the cell enters the mitotic phase as described in section 5.1. Mitosis in eukaryotes can be broken down into two functional phases:

karyokinesis where the cell core is divided and thus the separation of the duplicated DNA into two equally sized groups of chromosomes takes place

cytokinesis which is the physical division of the entire cell whereby the cytoplasm of a single cell is divided to spawn two daughter cells.

The process of karyokinesis is assumed to be an internal process of the proliferating cell within the simulation. Although it is possible to model karyokinesis within the simulation, its effects on the surrounding medium are marginal.

From a technical point of view the spherical cell begins to deform into a bell-shape and finally splits up into two spherical objects. The demanding part in modelling this process in a simulation is the fact that proliferation is an abrupt transition where a new agent has to be inserted into the simulation. Furthermore the triangulation is built to handle spherical objects only, so the cell elongation must be captured by a combination of spheres. Referring to the mitotic cell as the "mother cell "and to the two offsprings as "daughter cells", the two daughter cells will have to be inserted close to each other. Using the JKR interaction model this yields extreme velocities, which, although they may be treated with the adaptive stepsize routine, break down the applicable timestep for the dynamics. This leads to an increase in computational effort, which would render the simulation of larger systems infeasible.

Possible algorithms for cytokinesis

At this point a detailed implementation of the mitotic process is needed that does not require a timestep smaller than the one used during non proliferative growth of the system. Multiple approaches are imaginable. The simplest method consists in shrinking the mother cell to initial size, displacing it in a random direction and inserting a daughter cell inversely to the mother's displacement. This method works as long as the resulting displacements are relatively small. However, it lacks elegance and is not able to capture the dynamics of cytokinesis itself. Moreover, in a dense tissue of proliferating cells this implementation

will lead to severe artificial speedups of cell velocities due to unfavourable configurations rising. An effective algorithm has to take care of situations were two proliferating cells are neighbours and the randomly determined proliferation direction is chosen in a way that would move the daughters into each other. There are multiple favourable solutions to this problem:

1. Proliferating cells are interacting normally but the reciprocity between sister cells is disabled during proliferation and replaced with an velocity that is kept constant until mitosis is completed (e.g. until both cells are close to the mutual JKR equilibrium distance). This approach may lead to cells staying arbitrary long in the mitotic phase.

2. Proliferating cells can exert forces onto neighbouring cells not currently undergoing mitosis, but this interaction is not considered to be symmetric - the mitotic cell is only affected by interactions with other proliferating cells; the resulting forces are projected onto the plane defined by the proliferation direction as normal vector in order not to affect the sister separation. This approach can ensure a defined mitotic phaselength which is sufficient to separate the sister cells.

3. Interaction between common daughter cells is disabled and replaced by a cytokinesis velocity that ensures full separation within mitosis time. Proliferating cells fully interact with neighbouring cells but forces imposed on them are projected onto a plane perpendicular to the proliferation direction in order not to interfere with cytokinesis (see figure 6.1 and 6.2 for a sketch of this method).

The latter algorithm was used as a standard method for the implementation of proliferation throughout the simulation, and is referred to as advanced cytokinesis model. It offers the possibility to model the process of cytokinesis in detail, which might be of interest in itself, since a complex rearrangement of surface proteins is essential for cytokinesis (see *Bauer et al.* (2008) for details). Furthermore, if combined with an local and global adaptive stepsize algorithm, it offers a tremendous improvement in simulation runtime compared to straightforward proliferation methods (as shown in figure 6.5).

6.2 Details on the cytokinesis algorithm for agent-based simulations

Upon mitosis, a random direction is determined and the mother-cell is slightly displaced in this direction while a daughter cell is inserted inversely. The displacement of both cells is chosen to be much smaller than the final equilibrium distance in order to minimise the disturbance to the simulation. To model the bell-shape during mitosis both cells separate with a constant velocity (v_{mit}), while their radii are decreased at the same time according to the shrinking factor (f_{shrink}) (see figure 6.3).

The magnitude of the mitotic velocity v_{mit} is determined to ensure full separation into the corresponding JKR equilibrium position:

$$v_{mit} = \frac{(d_{jkrequi} - d_{mit})}{\tau_{\mathrm{M}}} \tag{6.1}$$

with $d_{jkrequi}$ being the equilibrium distance of two cells of initial size ($r_{initial}$) under JKR interaction, d_{mit} the slight displacement of the cells at the beginning of cytokinesis and τ_{M} the length of the mitotic phase in minutes.

Similar to the cell growth factor in phases G_1 and G_2:

$$f_{grow} = \frac{(r_{tar} - r_{ini})}{(\tau_{\mathrm{G}_1} + \tau_{\mathrm{G}_2})} \tag{6.2}$$

a shrinking factor for cytokinesis is calculated to ensure volume conservation and bring the daughter cells down to the preferred initial cell size:

$$f_{shrink} = \frac{(r_{tar} - r_{ini})}{\tau_{\mathrm{M}}}. \tag{6.3}$$

In order to ensure volume conservation, the radius of daughter cells after cytokinesis (start of the G_1-phase) must be determined so that two daughter cells take up the same volume as one large mother cell before cytokinesis (at end of the G_2-phase):

$$r_{ini} = r_{tar} 2^{-1/3} \tag{6.4}$$

$$\tag{6.5}$$

Where r_{ini} refers to the decreased cell radius after proliferation (at the start of G_1) and r_{tar} to the final cell radius (at the end of G_2). Example values for the cell radii are given in table 3.2, as cell sizes vary according to the cell type.

Cell interaction during mitosis

Cell-cell interaction during cytokinesis is limited in a way that the interaction between common mitotic daughter cells is replaced by the artificial mitotic force and other interaction forces are projected onto the plane perpendicular to the proliferation direction:

$$\boldsymbol{n}_{mit} \cdot \boldsymbol{p} = 0 \tag{6.6}$$

$$\boldsymbol{n}_{mit} \cdot \boldsymbol{F}_{res} = 0 \tag{6.7}$$

where $\boldsymbol{n}_{mit}$ is the vector in mitosis direction (normal vector of the plane), $\boldsymbol{p}$ an arbitrary vector lying in the perpendicular plane and $\boldsymbol{F}_{res}$ the projection of the force vector onto the perpendicular plane.

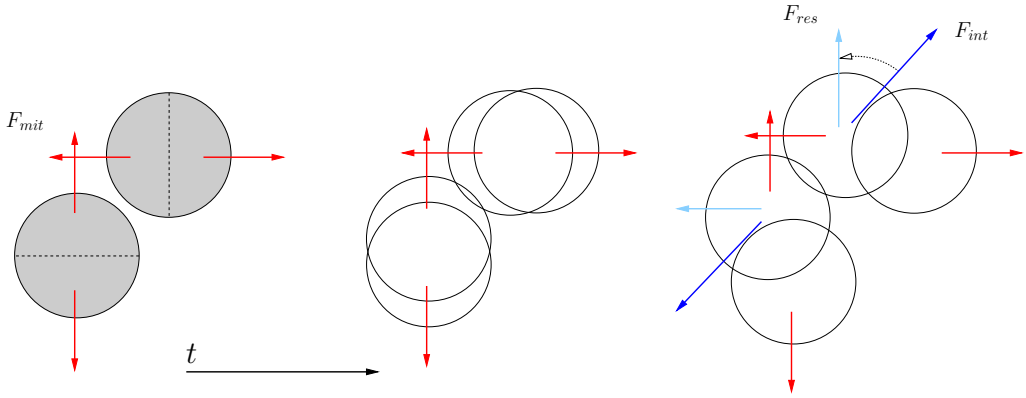

Figure 6.1: Sketch of the cytokinesis handling implemented in this thesis. Cells draw a random cytokinesis direction upon the start of mitosis and spawn a daughter cell nearby to model the bell shaped deformation (see figure 6.3). In a dense layer of mitotic cells this may lead to cells being moved into each other, in the case of unfortunate cytokinetic directions. This collision is detected due to the fact that mitotic cells show full interaction with other mitotic cells. However, the force F_{int} along with all other interaction forces between mitotic and non-mitotic cells will be projected onto the plane defined by the cell's mitosis direction as plane normal. This ensures full separation of mitotic daughters after a predetermined timespan as the mitotic force F_{mit} is left unchanged.

6.3 Effects of the algorithm on the overall simulation performance

The newly developed advanced proliferation mechanism yields a significant performance improvement of the simulation, due to decreased maximum velocities as seen in figure 6.4. Unnatural cell velocities as a result of unfortunate cell conformations are decreased, therefore making the global adaptive stepsize on average larger, what yields a significant increase in simulation performance (see figure 6.5).

This effects add up to a highly increased simulation performance (note the decrease of the iteration number due to the adaptive timestep in figure figure 6.5).

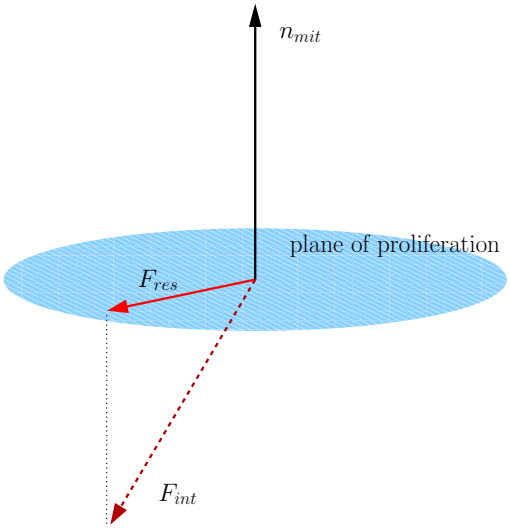

Figure 6.2: Sketch of the force projection during proliferation as implemented in the cytokinesis algorithm. Interaction forces F_{int} are projected unto the plane of proliferation defined by the plane normal n_{mit}. The projected forces F_{res} are used for the propagation of mitotic cells together with their mitotic force, to ensure full separation within the according phaselength τ_{M} and still preserve as much system dynamics as possible.

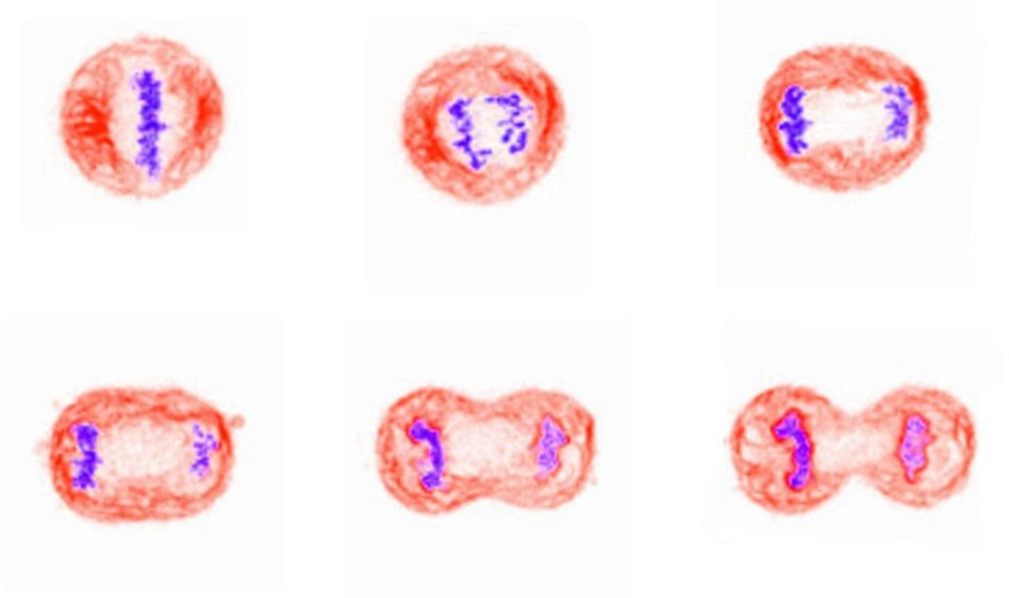

(a)

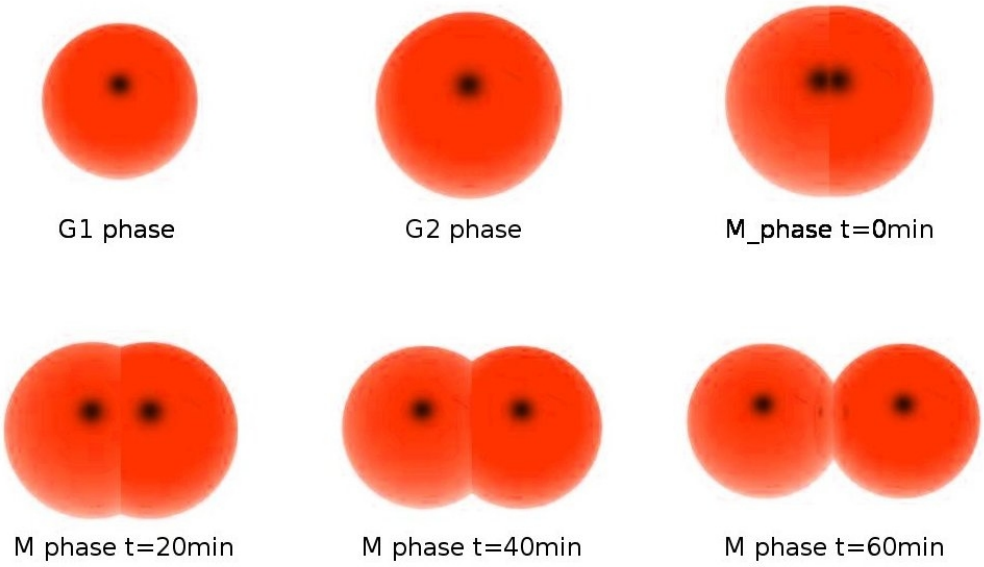

(b)

Figure 6.3: **(a)** Mitosis in vivo: chromosomes (shown in purple) line up in the metaphase plate and are pulled apart. Tubules of the ER (stained red) bind to chromatin. During the later stage of karyokinesis DNA binding proteins that reside in the ER immobilise some of the tubules. They are flattened out to create the nuclear membrane for cytokinesis. **(b)** In silico simulation of the cell cycle and mitosis according to the implemented cytokinesis algorithm. From top left to bottom right: growth of cell in G1 and G2, begin of cytokinesis (top right), separation process accompanied by shrinkage of the daughter cells (lower left), final equilibrium position for both cells at initial cell size (lower right). Black spots in (b) are not identical with the cells nucleus but are results of the POV-Ray rendering. Source picture used to create collage (a) by Daniel J. Anderson, Salk Institute for Biological Studies.

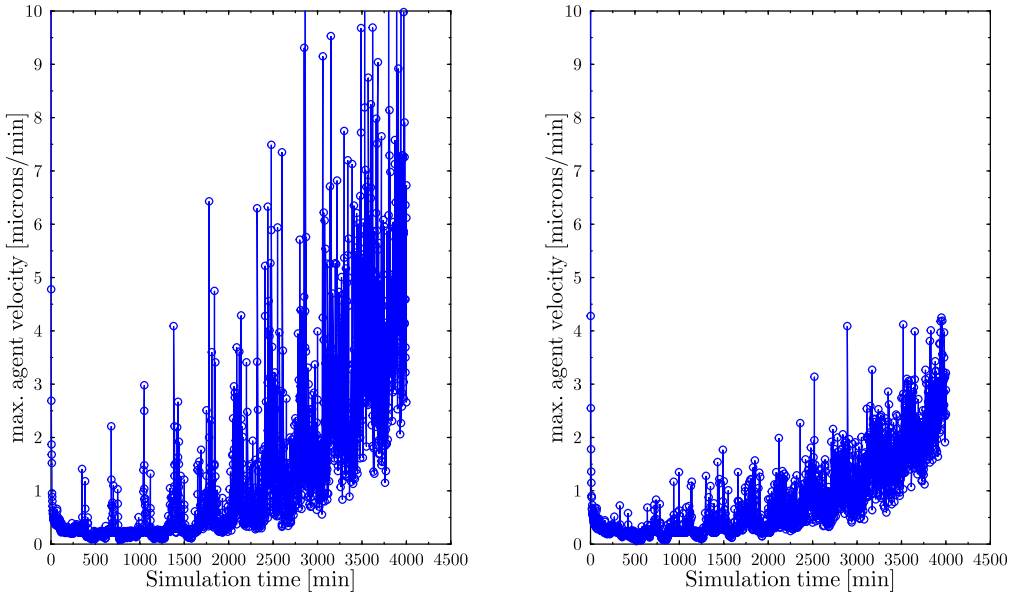

(a) simple cytokinesis model

(b) advanced cytokinesis model

Figure 6.4: Comparison between a sample simulation without and including the advanced proliferation method. Note the dramatic change in maximum velocity peaks due to a smoother proliferation.

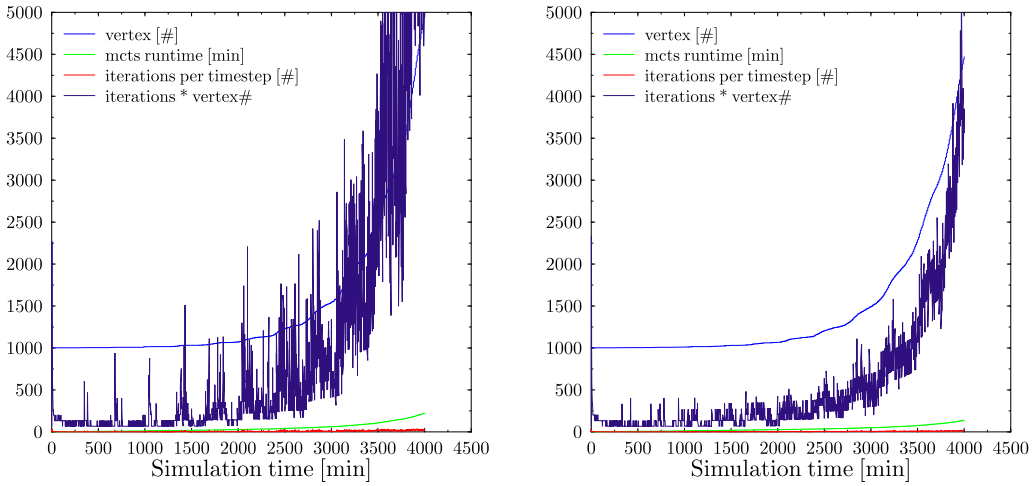

(a) simple cytokinesis model

(b) advanced cytokinesis model

Figure 6.5: Comparison between a sample simulation without and including the advanced proliferation method. Note the dramatic change in the number of iterations per timestep due to a smoother proliferation.

7 A social dimension - cells in tissue

7.1 Defining neighbourship relations through spacial tessellations

Eukaryotes aggregate in large colonies and eventually form tissues, in which direct interaction is limited to cell neighbours which are in contact. However, determining which cells should interact is not a trivial task, since the tissue-simulation is done in free space and cross checking all cells would results in a quadratic runtime. Instead of checking all cells for neighbourship with each other, it would be useful to obtain a list of interaction partners for each cell agent.

This can be done in an efficient and elegant way using a Delaunay triangulation of the simulation space. A straightforward way to introduce the Delaunay triangulation is through its dual, the Voronoi tessellation (see *Aurenhammer* (1987); *Okabe et al.* (2000)). In solid state physics the Voronoi tessellation is also known as partition into Wigner-Seitz cells. Within the scope of tissue simulations the Voronoi tessellation offers direct access to cell contact surfaces and cell volumes (see figure 7.2).

As the complexity of triangulations lies beyond the scope of this thesis, the following section will be limited on introducing the necessary terms and concepts. For a detailed disquisition on spatial tessellations and their efficient algorithmic implementation the reader is referred to *Beyer et al.* (2005b) and *Beyer* (2007).

Voronoi tessellation

The Voronoi tessellation of a set of generators is defined as the partition of space into Voronoi cells V_n for which every point of one cell is closer to its generator $\mathbf{v}_n$ than to any other generator $\mathbf{v}_m$.

Definition 10 (*Vertex*)

Let $\mathbf{x} \in \mathbb{R}^3$ define a point. The pair $X = (\mathbf{x}, w_x) \in \mathbb{R}^3 \times \mathbb{R}$ is called a vertex. w_x is called weight of the vertex X.

Together with its weight a vertex can be interpreted as a sphere with radius $\sqrt{w_x}$ at position $\mathbf{x}$, and therefore vertices can represent cells in a regular triangulation. However, the concept of triangulations can be applied to objects of higher dimension in an equal way.

For the later definitions two more objects are of great importance:

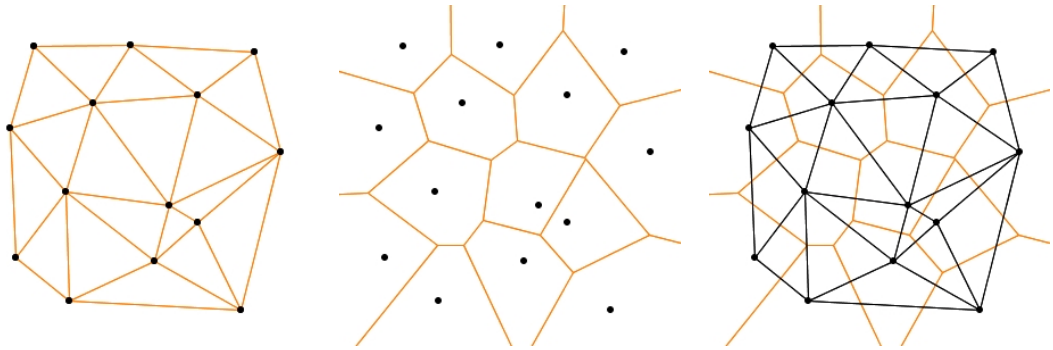

(a) (b) (c)

Figure 7.1: Duality between the Delaunay triangulation and the Voronoi diagram. **(a)** A Delaunay triangulation of a random set of generators $\mathbf{v}_n$. **(b)** Voronoi tessellation of the same point set. **(c)** Overlay of Delaunay triangulation from (a) in black and Voronoi tessellation from (b) in orange showing the fundamental relationship of duality between them.

Definition 11 (*Simplex*)

A simplex σ is defined as the convex hull of $d+1$ points $\mathbf{v}_i \in \mathbb{R}^d$ in a d-dimensional space.

In 2 dimensions the corresponding 2-simplex will be a triangle as depicted in figure 7.1(a), in 3 dimensions the term simplex (or 3-simplex) is a synonym for a tetrahedron. To simplify the notation the points of a simplex $\sigma_{\langle P_1,P_2,P_3,P_4\rangle}$ will be noted by the vertices with the corresponding coordinates $\mathbf{p}_i$, $i = 1, 2, 3, 4$. Another simplification of notation is

Definition 12 (*Edge and face*)

An edge (1-simplex) $\langle P_1, P_2\rangle$ is the line connecting the points $\mathbf{p}_1$ and $\mathbf{p}_2$. A face (2-simplex) $\langle P_1, P_2, P_3\rangle$ is the triangle formed by $\mathbf{p}_i$, $i = 1, 2, 3$.

A classical approach from solid state physics for the generation of the Voronoi tessellation is to draw the connection lines between all neighbouring generators $\mathbf{v}_n$ and then add the perpendicular bisectors of the sides. The area around the generator bound by the bisectors is the Voronoi cell of the generator (see figure 7.1(b)).
An example of a voronoi tessellation is the investigation of the natural patches of post offices in a city. The logical patch for each post office will consist of all areas of the city for which the distinct post office is nearer than any other office.

Following the introduction from *Beyer* (2007) from this point on we can define a voronoi tessellation as

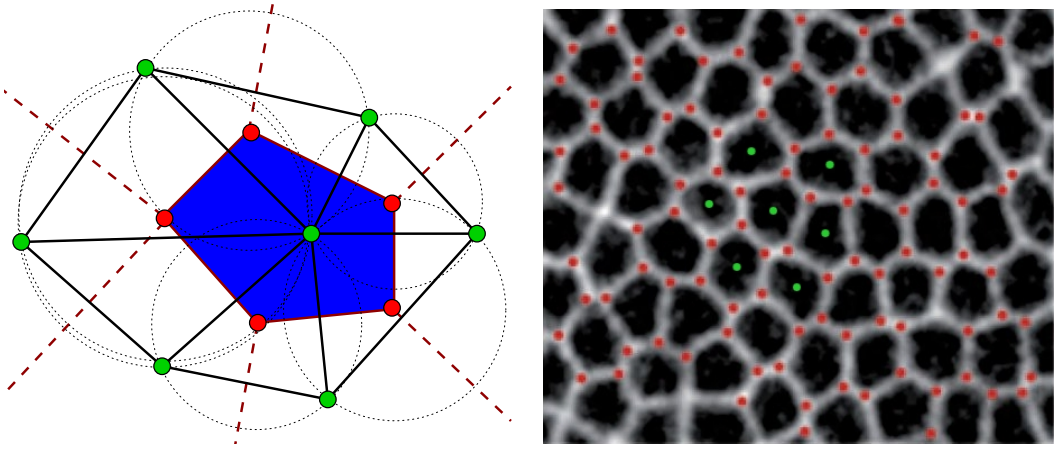

(a) (b)

Figure 7.2: Correspondence of the Voronoi tessellation to the cell form in a real tissue. **(a)** Voronoi tessellation created according to the empty circumsphere criterion. Green points are vertices in the Delaunay triangulation corresponding to cell centres. The blue polyhedra is the Voronoi cell which can correspond to the biological cell. Vertices of the Voronoi cell are shown as red points. **(b)** Cells in a tissue under the microscope. The actual cell shape is polyhedral and therefore modelled in an optimal way within a Voronoi approach. Cell centres marked with green dots, cell edge vertices with red dots. Source for figure (b) is *Lecuit and Lenne* (2007).

Definition 13 (*Voronoi tessellation*)

a subdivision $\{C_n\}$ *of space such that*

$$\bigcup_n C_n = \mathbb{R}^3 \quad \textit{with} \quad C_n = \left\{\mathbf{x} \in \mathbb{R}^3 : \|\mathbf{x} - \mathbf{v}_n\| < \|\mathbf{x} - \mathbf{v}_m\| \ \forall\, m \neq n\right\}. \tag{7.1}$$

The points $\mathbf{v} \in \mathcal{S}$ *are called the generators and the* C_n *are called Voronoi cells.*

For the case defined in equation 7.1 the resulting Voronoi cells are polyhedra in three dimensions.

Considering the duality of the Delaunay triangulation and the Voronoi tessellation each face of the Voronoi cell polyhedra corresponds to an edge in the Delaunay triangulation between the vertices being the generators of those two cells (see figure 7.1). With the help of figure 7.2 it becomes obvious that the centre of the circumsphere of the simplices of the Delaunay triangulation are the endpoints of the polyhedra forming the Voronoi cells.

If different weights are assigned to the generators $\mathbf{v}_n$ (corresponding to cells of different sizes) then the result is a generalised Voronoi tessellation, also refered to as power diagram, which always exists and guarantees the existence of its dual, the regular Delaunay triangulation (which is defined in the next section). In the weighted case the normal Euclidean distance is replaced by a weighted norm. This requires the definition of the power distance and the orthosphere:

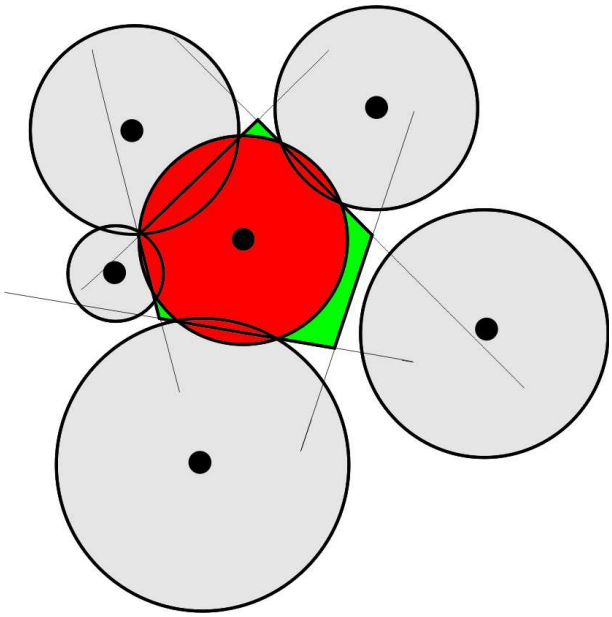

Figure 7.3: The Voronoi tessellation is the dual graph of the regular triangulation. Here it is shown for the vertex indicated by the red disk. The neighbour vertices are marked as grey disks. The Voronoi cell is a polygon shown in green.

Definition 14 (*Power distance*)

The power distance of two vertices U, V is given by

$$\rho(U,V) = \|\mathbf{u} - \mathbf{v}\|^2 - w_u - w_v. \tag{7.2}$$

With $\|.\|$ denoting the Euclidian distance in $\mathbb{R}^3$.

With the help of the power distance the orthosphere of a simplex can be defined:

Definition 15 (*Orthosphere*)

The orthosphere M of a simplex $\sigma_{\langle V_1,V_2,V_3,V_4\rangle}$ is defined as the solution $M = (\mathbf{m}, w_m)$ of the equations $\rho(V_i, M) = 0\,,\ \forall i = 1,2,3,4$.

In case the weight w_m of the orthosphere is positive it can be interpreted as a sphere such that the tangential planes of M at the intersecting points of the spheres representing the vertex weights w_i are orthogonal to the tangential planes of these spheres. Note that, even when all vertices V_i have a positive weight, the orthosphere M can still have a negative weight and the radius is given by $\sqrt{|w_m|}$.

The formal definition of a weighted voronoi tessellation is given by:

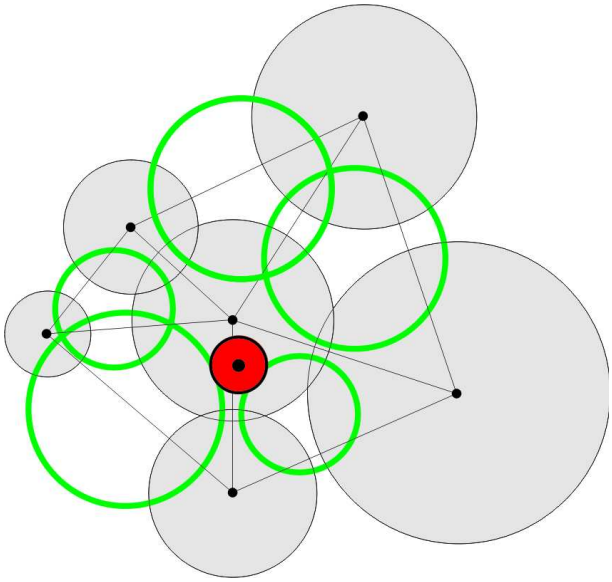

Figure 7.4: Orthocircles of a triangulation in 2D. Each orthocircle M (green) corresponds to a simplex and intersects all circles associated with the vertices of that simplex perpendicularly. The weight of each vertex is represented as the radius $\sqrt{w}$ of the circles. The vertex indicated by the red disk is redundant because it lies outside of all orthocircles of all simplices formed by the surrounding vertices indicated as grey disks. Thus, the redundant vertex is not endpoint of any simplex and the structure of the triangulation does not change if this vertex is present or not.

Definition 16 (*Weighted Voronoi tessellation*)

A weighted Voronoi tessellation *is a subdivision* $\{C_n\}$ *of space such that*

$$\bigcup_n C_n = \mathbb{R}^3 \tag{7.3}$$

with

$$C_n = \left\{\mathbf{x} \in \mathbb{R}^3 : \|\mathbf{x} - \mathbf{v}_n\| - w_{v_n} < \|\mathbf{x} - \mathbf{v}_m\| - w_{v_m} \; \forall \, m \neq n\right\} \tag{7.4}$$

$$= \left\{\mathbf{x} \in \mathbb{R}^3 : \rho\left(X, V_n\right) < \rho\left(X, V_m\right) \; with X = (\mathbf{x}, 0) \; \forall \, m \neq n\right\}. \tag{7.5}$$

The vertices $V \in \mathcal{S}$ *are called the generators. The* C_n *are called* Voronoi cells *or* Laguerre cells.

The Voronoi cells of this type are also called *Laguerre cells* and the tessellation is called a weighted Voronoi tessellation. The duality between the weighted Voronoi tessellation and the regular triangulation is similar to the simple Voronoi/Delaunay case. Instead of circumspheres the centers of the orthospheres of the simplices are the endpoints of the Laguerre cells (see figure 7.3).

Regular Delaunay triangulation

The Delaunay triangulation of a point set is a collection of edges satisfying an "empty circle" property: for each edge we can find a circle containing the edge's endpoints but not containing any other points. Alternately, it can be defined as a triangulation of the sites with the additional property that for each triangle of the triangulation, the circumcircle of that triangle is empty of all other sites.

The triangulation T is said to be a regular triangulation (also known as weighted Delaunay triangulation) if the orthosphere of every simplex $\sigma < A, B, C, D > \in T$ contains

no vertices (see figure 7.4).

Considering the duality of the Delaunay triangulation and the Voronoi tessellation each face of the Voronoi cell polyhedra corresponds to an edge in the Delaunay triangulation between the vertices being the generators of those two cells (see figure 7.1). With the help of figure 7.2 it becomes obvious that the centre of the circumsphere of the simplices of the Delaunay triangulation are the endpoints of the polyhedra forming the Voronoi cells.

Access and usage of the triangulations properties

For applications, mainly three properties of the weighted Voronoi tessellation are needed. These are the volume of the Voronoi cell, the area of the face between two cells and the distance between a face of the cell and its generating vertex. The regular triangulation of the system *Edelsbrunner and Shah* (1996); *Okabe et al.* (2000); *Ferrez* (2001) is the basic geometric structure used for cell modelling throughout this thesis. The used algorithm to implement a dynamic and kinetic triangulation is described in detail in *Schaller and Meyer-Hermann* (2004) and *Beyer et al.* (2005b).

7.2 The fluid-tissue analogy and cell sorting

Large amounts of cells can effectively behave like a fluid. This phenomenon is known as the fluid-tissue analogy. Cells show differential adhesion depending on the type of and amount of CAMs expressed on their surface (as implemented according to equation 3.7) much like liquids do according to their surface energy (see equation 7.6). Cell sorting and aggregation can be explained based on this mechanisms of differential interaction *Lecuit and Lenne* (2007). Also large parts of complex tissue formation reside on the use of this mechanism. This differential adhesion hypothesis can also be used to explain tissue sorting by affinity in the early embryonic development *Townes and Holtfreter* (1955).

Surface tension and tissue sorting

Cell surface tension is analogous to the tension occurring at the boundary layer of a fluid. In a fluid, surface tension is caused by the attraction between the molecules of the liquid by various intermolecular forces. In the bulk of the liquid each molecule is pulled equally in all directions by neighbouring liquid molecules, resulting in a net force of zero. At the surface of the liquid, the molecules are pulled inwards by other molecules deeper inside the liquid and are not attracted as intensely by the molecules in the neighbouring medium. Therefore, all of the molecules at the surface are subject to an inward force of molecular attraction, which is balanced by the resistance of the liquid to compression (see figure 7.5). This inward pull tends to diminish the surface area, and in this respect a liquid surface resembles a stretched elastic membrane. Thus the liquid squeezes itself together until it has the locally lowest surface area possible under the given boundary conditions.

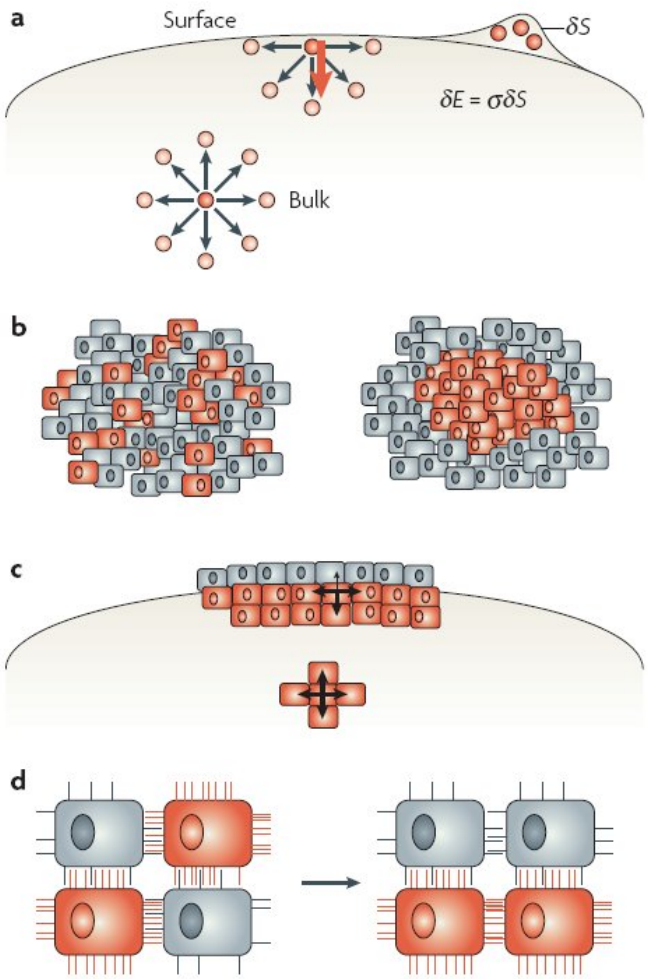

Figure 7.5: Surface tension can explain large parts of complex tissue formation shown in **(b)**. Mechanisms for droplets in fluids **(a)** and cells in tissue **(c)** are functionally similar. **(d):** Cells are sorting depending on their expression level of cadherins on their surface. Picture from *Lecuit and Lenne* (2007).

Equation 7 (*Surface energy*)

A change in surface energy can be described by the expression

$$\delta E = \sigma \delta S \tag{7.6}$$

where δE is the surface energy difference, δS the change in surface area and σ the surface energy coefficient.

As a results of equation 7.6 a liquid must minimise its number of boundary molecules (and therefore its surface area) in order to minimise its energy state (see also figure 7.5).

Another way to approach this phenomenon is to assume that a molecule in contact with a neighbour is in a lower state of energy than if it weren't in contact with a neighbour. This view can be implemented straightforward into modelling of separation phenomena, with the use of energy models such as the Potts model (see *Graner and Glazier* (1992)).

In tissue sorting cells obey a mechanism which effectively implements equation 7.6. Binding energy is mediated through the level of CAM-adhesion. If two populations of cells, which are different in respect to the preferential binding of their CAMs, are mixed,

they will tend to separate as binding between cells of the similar population is preferable (as illustrated in (d) of figure 7.5).

This tissue sorting is reproduced straightforward within this modelling approach (see section 9.2).

Artificial boundary pressure

Within the simulation, cells which lie on the boundary of the growing spheroid may be subject to an artificial force pointing to the spheroid centre. This is in correspondence to the surface energy defined in equation 7.6. Furthermore, the mechanism has been included to mimic the influence of surrounding tissue in a first approach. The favourable approach would be to surround the growing tumour by a layer of benign tissue. However, this involves simulation of a high number of cells which are healthy and, therefore, of minimal interest for the investigation. To minimise the thickness of this surrounding layer and to simulate a realistic environment without having to apply excessive computational power, a combination of both mechanisms can be used. In this combination the artificial forces are acting only on the surrounding healthy tissue, which can deliver a realistic interaction to the growing spheroid.

7.3 Mechanical inhibition

Cells in a tissue are in competition for limited resources such as glucose or cellular growth factors all the time. Therefore, when multiple cells come into contact, they may come to an arrest of cell growth due to contact inhibition. Even cells which are genetically modified to suppress apoptosis maintain this phenomenon, which complicates handling of cell cultures in laboratories. Cancerous cells often lose this property, and thus grow in an uncontrolled manner even when in contact with neighbouring cells.

The mechanisms through which contact inhibition is mediated are not fully understood yet. Depletion of growth factors and other solubles from the extracellular space by the surrounding tissue might play an important role, as it is seen in in vitro tissue cultures. This effect can be easily integrated into the simulation with the help of a soluble diffusion system for growth factors.

Pressure-mediated inhibition

Another possible source of contact inhibition can be termed as mechanical inhibition. It stems from the pressure imposed on a single cell by its neighbours. If this pressure exceeds a certain limit, the cell can react by going into quiescence.

This cell pressure can be obtained locally for each cell in an agent-based simulation through the properties of the voronoi tessellation. As pressure is defined as force divided by area, the effective pressure on a cellular agent is given by the sum of the interaction force divided by the voronoi face shared with the according neighbour:

Definition 17 (*Cell pressure*)

$$P_i^{total} = \sum_{j \subset \mathcal{N}} P_{ij} = \sum_{j \subset \mathcal{N}} \frac{F_{ij}}{A_{ij}} \tag{7.7}$$

where P_{ij} denotes the pressure imposed on cell i by its neighbour j, F_{ij} the force and A_{ij} the voronoi contact surface between those two cells.

Due to the nature of the voronoi tessellation the JKR force will always be parallel with the plane normal of the voronoi face and therefore perpendicular with the plane itself.

$$\boldsymbol{F_{ij}} \parallel \boldsymbol{n_{vf}} \tag{7.8}$$

This pressure can be computed at any time and may be checked at the restriction point to decide whether the cell should initiate mitosis or go into quiescence. It is also valuable in order to obtain the pressure distribution inside the tumour spheroid. Possible further implementation can include a pressure repulsion of highly compressed cells acting on their neighbours of lower pressure.

8 The simulation application in detail

The developed application is written in C++ code. There are two largely independent classes which are at the centre of the simulation: the *cell*-class and the *triangulator*-class. An instance of the first is spawned for each cell in the simulation and handles all of the cells properties and abilities through its variables and member functions. The latter one is used to store the arrangement and layout of the cells and to obtain the neighbourhood topology with the help of a kinetic dynamic triangulation. An overview of the simulation algorithm is given in pseudocode (see algorithm 8.4 on page 76).

8.1 Classes and libraries

This section will only give a brief overview about the basic mechanism used to implement the application for this thesis. For a complete and documented functions overview see the header files of the according class `class.h` or the doxygen documentation.

The cell-class

The `cell`-class provides variables and functions that may be used by every instance of that class. It is developed in order to capture all possible cell mechanisms which are of interest to the modelling. Each cell is spawned by the constructor function of this class and is thereafter existent as an individual object, as described in section 2.2. Some important functions of the cell class:

- `Cell ( Spacepoint<double>& colourtemp, int phasetemp, ... ){}`
  Constructor - inserts a coloured cell given by colour-vector in an initially defined cell-phase with initially defined phaselength
- `void calculate_velocity ( Triangulator<double,Cell>& tri );`
  Calculates the velocity of an agent using an overdamped approach

The cell state is stored in the private variables of the cell class. Some examples can be found here:

- `int phase;`
  Stores the current phase of the cell
- `double phaselength;`
  Remaining time until phase-transition-checkpoint is reached

- `bool proliferating;`
  Marks if the cell is in the mitotic state
- `Spacepoint<double> v;`
  Vector representation of the current cell velocity
- `double elastic_modulus;`
  elastic modulus ϵ of the agent in Pascal
- `double ligand_concentration;`
  ICAM ligand concentration average on cell surface

`check_phase()` and `update_phase()` are the two functions which are at the heart of the cell cycle class, triggering events which happen according to the internal cell timing.

```
check_phase()
G_0 decrease phaselength
G_1 decrease phaselength, grow
S decrease phaselength
G_2 decrease phaselength, grow
M decrease phaselength, shrink
N if nutrients below necrosis threshold send into necrosis
if phaselength = 0 ( update_phase() )

update_phase()
G_0/G_1 check_nutrients && check_pressure
G_1/S check_nutrients && check_pressure
S/G_2 check_dna_integrity
G_2/M proliferate
```

The triangulator-class

The triangulation is stored as a connected simplex list. The data for a simplex is stored as pointers to its four vertices and to its four adjacent simplices. The faces of outer simplices that have no adjacent simplex are omitted. The vertices are also stored in a list. Each of the vertices has a list of pointers to simplices which have this vertex as endpoint. A list of neighbour vertices is also stored using pointers.

Other variables important for the dynamic and efficient update of the triangulation are stored within the simplex data structure. For each pointer to a neighbour simplex the result of the last orthosphere criterion calculation is stored, together with a flag indicating its last update. Depending on the subroutine which are presented below, the result of a former computation can be reused without actually performing the calculation.

The triangulation can be recalculated from the scratch at any time, but is usually dynamically updated at all times, which yields a great performance improvement (see

Beyer et al. (2005a)). Even for relatively small system sizes of about 1000 spheres the complete re-triangulation is a faster method for determining the neighbourhood topology than the naive method of cross-checking all spheres (as shown in *Schaller* (2006)). Update of a existing delaunay triangulation is orders of magnitude faster than the cross-checking method. The update of the triangulation is done with the help of sophisticated flip-algorithms, which can locally restore the delaunay triangulation if its validity was lost through movement of vertices (spheres).

For the purpose of using the dual graph – the Voronoi tessellation – the center of the orthosphere is stored in the simplex structure, again invoking a flag that indicates if a recomputation is needed. The changes to the triangulation are handled differently for simplices and vertices. Simplices are only created and destroyed. Vertices keep their data structure and change properties in the case of triangulation kinetics. They are also created/removed during triangulation dynamics.

Since the triangulator code is ready for parallel computing, it makes use of a unique metapointer concept to identify vertices (cells) on all processes (see *Beyer et al.* (2005a) and *Beyer* (2007)). The parallel implementation is based on the Message Passing Interface (MPI). The concept is to run the same program on different processes – which are usual different physical processors or even computers – and include code that defines which process performs which instruction, including sending or receiving data from other processes through some type of network provided by the hardware.

Further classes

Further important classes include the `soluble`-class, which is used to solve reaction-diffusion-equations with the ADI-algorithm, and the `random`-class, as an interface to provide sophisticated random functions.

Important libraries

Important libraries in use are SPRNG[1] for parallel random number generation, boost [2], iRRAM[3] for exact arithmetic in C++, and ParMETIS[4] for parallel graph partitioning and fill-reducing matrix ordering.

8.2 Further features

The application can write out the actual state of the triangulation and cell agents either in vrml or POV-Ray compatible format. This can be used to visualise the tumour dynamics as it was done within this thesis (see section 9).

[1] `http://sprng.cs.fsu.edu/`
[2] `http://www.boost.org/`
[3] `http://www.informatik.uni-trier.de/iRRAM/`
[4] `http://glaros.dtc.umn.edu/gkhome/metis/parmetis/download`

8.3 Parameters and system setup

A parameter parser was integrated into the application in order to allow the change of simulation parameters at runtime and store them in ordered parameter-files. With the help of this parameter file it is possible to setup scripted runs with different input parameters automatically. A detailed explanation on the parameters is provided within the parameter file itself.

System setup and agent insertion

In order to initialise the system randomly but close to an equilibrated solution a Monte Carlo method was used, where particles are randomly inserted into a cubic volume, but kept only if they lie within an spherical boundary volume, V_t:

$$V_p = \frac{4}{3}\pi r_p^3 \tag{8.1}$$

$$V_t = \frac{4}{3}\pi r_t^3 \equiv \sum_p V_p = \#pV_p \tag{8.2}$$

$$r_t = \sqrt[3]{\#pr_p^3} \tag{8.3}$$

For the simulation of avascular growth the typical initial configuration will be a core of malignant cells (or just one cell) surrounded by a shell of benigm tissue.

8.4 Simulation algorithm in pseudocode

parameter	used in simulation	literature value	remark
G_1-phase τ_{G_1}	8 h	(6.0 ± 1.0) h	(1), type dependent
S-phase τ_S	6 h	(10 ± 2.0) h	(1), type dependent
G_2-phase τ_{G_2}	4.5 h	(2.0 ± 0) h	(1), type dependent
mitotic phase τ_M	1 h	(1.0 ± 0) h	(1), type dependent
G_0-phase τ_{G_0}	1.5 h	–	effective value
apoptosis duration τ_A	10 h	(10 ± 2) h	(1), type dependent
necrosis duration τ_N	24 h	(50 ± 2) h	(1), type dependent
initial cell size (radius) r_{ini}	7.94 μm	–	see table 3.2
target cell size (radius) r_{tar}	10 μm	–	see table 3.2
cell elastic modulus E	1000 Pa	1000 Pa	(2)
cell Poisson number ν	0.5	0.5	(3)
cell surface energy σ	0.1 nNμm^{-1}	–	
ECM viscosity η	$5 \cdot 10^{-3}$ kg μm^{-1}s^{-1}	$5 \cdot 10^{-3}$ kg μm^{-1}s^{-1}	(5)
contact inhibition crit. P_{crit}	500 Pa	600 Pa	(5), (13)
G_0 crit. nutrient conc. C_{G0}	0-12 mmol m^{-3}	–	highly variable
N crit. nutrient conc. C_N	0-2 mmol m^{-3}	–	highly variable
boundary pressure force F_{bound}	1 nN	–	effective value
oxygen diffusivity $D_{ox}^{H_20}$	2440.0 μm^{2}s^{-1}	2440.0 μm^{2}s^{-1}	(6)
oxygen diffusivity D_{ox}^{tiss}	1750.0 μm^{2}s^{-1}	1750.0 μm^{2}s^{-1}	(7), (8)
glucose diffusivity $D_{gl}^{H_2O}$	691.0 μm^{2}s^{-1}	691.0 μm^{2}s^{-1}	
glucose diffusivity D_{gl}^{tiss}	105.0 μm^{2}s^{-1}	105.0 μm^{2}s^{-1}	(9)
diffusion grid size x_{diff}	800 μm	–	cuboid volume
grid notes per dimension n_{diff}	40	–	${n_{diff}}^3$ nodes total
glucose boundary conc. C_{bgl}	16.5 mmol	–	Dirichlet boundary
oxygen boundary conc. C_{box}	0.28 mmol	–	Dirichlet boundary
overall oxygen uptake λ_{ox}	20.0 amol cell^{-1}s^{-1}	20.0 amol cell^{-1}s^{-1}	(12),(14)
overall glucose uptake λ_{gl}	95.0 amol cell^{-1}s^{-1}	95.0 amol cell^{-1}s^{-1}	(15),(12),(14)
default timestep Δt	5 min	–	adaptive stepsize
typ. global adaptive stepsize Δt_{ga}	1.5 min	–	typical value
displacement threshold Δx	0.25 μm	–	smaller than $0.1 r_{tar}$
diffusion rate update interval t_{diffup}	10 min	–	typical value
default diffusion timestep Δt_{diffev}	5 min	–	handled by solver

Table 8.1: Parameter table used for agent-based simulations of cell objects within this thesis. Cell phase durations in (1) are for EMT6/Ro spheroids and were altered in order to suit the cycle times of a more general cell type. Many parameters vary greatly depending on the type of system that is modelled - given values are exemplary in that cases. Stability of the application is independent of the choice of parameters. Compiled from sources: (1) *Zacharaki et al.* (2004), (2) *Guck et al.* (2001), (3) *Maniotis et al.* (1997), (4) *Chu et al.* (2004), (5) *Galle et al.* (2005c), (6) *Baranov et al.* (2000), (7) *Grote et al.* (1977), (8) *Rofstad et al.* (1996), (9) *Casciari et al.* (1988), (10) *Landry et al.* (1981), (11) *Freyer and Sutherland* (1986), (12) *Casciari et al.* (1992), (13) *Helmlinger et al.* (1997), (14) *Wehrle et al.* (2000), (15) *Kunz-Schughart et al.* (2000), *Schaller and Meyer-Hermann* (2005a), and *Schaller and Meyer-Hermann* (2005c).

Algorithm 1 (*Simulation overview in pseudocode*)

```
parsing of parameters
initialisation of random number generators
diffusion grids
triangulator
cell agent insertion into triangulation
for t ≤ t_end do
    force based cell interaction
    cell velocity calculation
    global adaptive timestep (Δt_ga = Δx / (v_ave f_ave))
    if v_cell ≥ v_ave f_ave then
        local adaptive timestep Δt_la = Δx / v_cell
    end if
    check phase
    if phaselength ≤ 0 then
        update phase
    end if
    synchronous displacement
    if t mod t_dif = 0 then
        diffusion grid update
    end if
    if t mod t_vis = 0 then
        output of visualisation and data
    end if
end for
output of simulation statistics
```

8.5 Simulation performance and scaling

Multiple sources contribute to the overall simulation runtime. The scaling of the triangulator in use is $n\log n$, close to linear behaviour (see *Beyer et al.* (2005a) for details). Initial exponential growth of the tumour as simulation object leads to an exponential rise in necessary computational effort. This contribution cannot be lowered but due to growth saturation its scaling is getting smaller with time. Solving the reaction diffusion grids takes up a fair amount of time in the beginning of the runtime depending on the precision aspired. The contribution from the diffusion solver loses importance with increasing runtime due to the exponential simulation scaling of the interaction part later on.

Runtime improvement such as the global and local adaptive stepsize and sophisticated cytokinesis algorithms greatly increase overall simulation performance (as shown in fig-

ures 4.4 and 6.5). The upper limit for simulations run on a single machine is about 10^6 cells. Growth of a tumour spheroid up to an amount of 200.000 cells over 20 days can be simulated within about 4 days on a single cpu of 3GHz (at high precision of about 1% cell's radius for Δx_{disp}). In order to be able to push the simulation size beyond this boundary further improvements on the simulation performance are necessary. Simple methods include asynchronous updates, in the sense that slow cells are not displaced until their displacement reaches the chosen simulation resolution Δx_{disp}. Sophisticated methods will treat simulation regions with slow dynamics as a single object in the process of coarse graining. However, such methods are beyond the scope of this thesis (see *Drasdo* (2005) for details on coarse graining in simulated cell systems). Due to the parallelisability of the problem (local interactions only) a significant performance increase can be expected from parallel execution. This possibility is already implemented in the triangulator class from *Beyer et al.* (2005a).

9 Simulation of cell and tumour dynamics

9.1 Cell motility

Typical velocity profile

As there is no active cell movement by default, the typical cell velocity profile is solely determined by cell-cell interactions and the pressure generated by mitotic cells. A major component in the velocity spectrum is the typical velocity of the mitotic daughter cells, which are pushed into equilibrium during mitosis. Cell velocity is increased in the intermediate region of the spheroid, which corresponds to the regime of high pressure (see figure 9.1 for details). If an active movement component is introduced, the velocity spectrum changes accordingly.

It is possible to calculate the typical cell velocities resulting from the displacement accuracy $\Delta x_{max} = 0.25\mu m$ which is used by the global adaptive timestep algorithm (see section 4.3) to determine the integration timestep. Displacement from the equilibrium position of two cells by Δx_{max} yields a JKR force of $\approx 2nN$, respectively $\approx 4nN$ in the worst case when both cells are displaced exactly against each other (assuming a cell size of 20μm). Using the equation for the cells' velocity (equation 4.8)

$$\dot{\boldsymbol{x}}_i(t) = \frac{1}{\gamma}\boldsymbol{F}_i^{total}(\boldsymbol{x}_i(t), \boldsymbol{x}_j(t)) \tag{9.1}$$

with the expression

$$\gamma = 6\pi\eta R_i \tag{9.2}$$

yields, for $R_i = 15.8\mu m$ and $\eta = 0.083\frac{nNmin}{\mu m^2}$, velocities of about $0.16\frac{\mu m}{min}$.

Displacement-velocity ratio

JKR-interaction between cells yields a force which leads to a distinct velocity depending on the cell radius. The displacement-velocity ratio for an exemplary cell size of $12.5\mu m$ is given in table 9.1, in order to illustrate typical cell velocities.

Initial cooldown of the spheroid

If the simulation is started with a high number of cells, the configuration can either be read in from a file or obtained via the insertion of cells according to the Monte Carlo

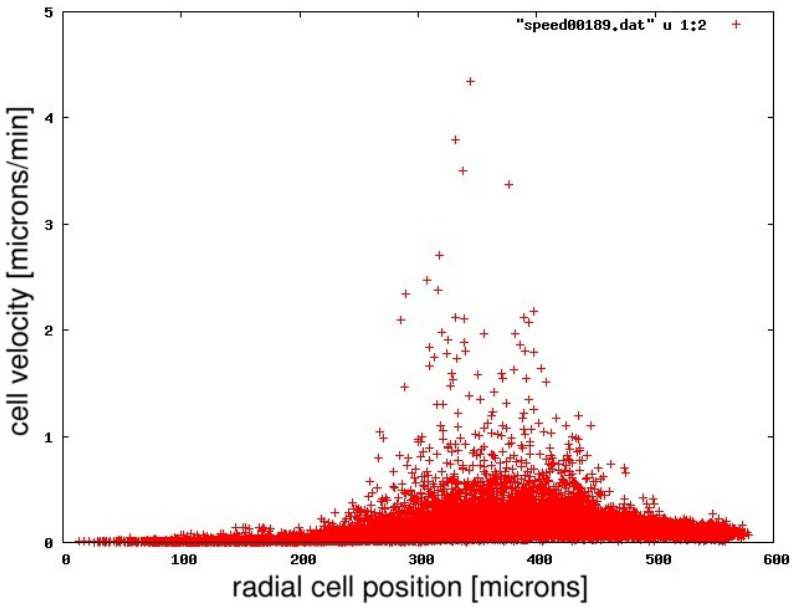

Figure 9.1: Typical velocity profile of a multicellular tumour spheroid in simulation. Cells in the necrotic core (0-150 μm) are almost motionless. The section between the inner quiescent cells and the proliferating boundary experiences the greatest pressure (300-400 μm). Accordingly, velocities in this region are high. In the outer proliferating rim of the tumour (500-600 μm) the velocity spectrum is dominated by the mitotic separation velocity of about $0.1\frac{\mu m}{min}$. See also the spectrum of this velocity distribution in figure 4.3.

cell displacement $[\mu m]$	JKR-force $[nN]$	resulting velocity $[\frac{\mu m}{min}]$
0.1	0.27	0.015
0.35	1	0.05
1	3.5	0.18
2	7.2	0.36
4	20	1
13.5	100	5

Table 9.1: Typical cell velocities for average cell radius of 12.5 μm, resulting out of a given cell displacement due to JKR-interaction. Frictional coefficient $\gamma \approx 20$, $\eta = 0.0833\frac{nNmin}{\mu m^2}$.

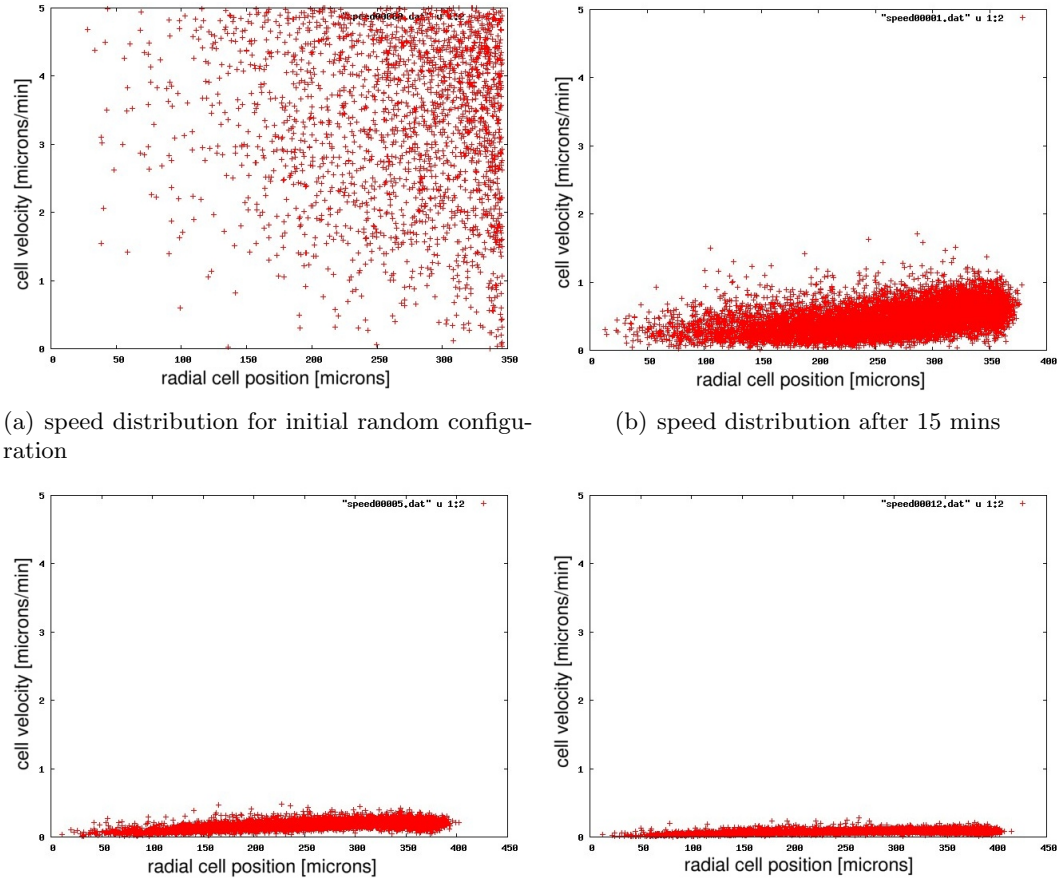

(a) speed distribution for initial random configuration

(b) speed distribution after 15 mins

(c) speed distribution after 75 mins

(d) speed distribution after 150 mins

Figure 9.2: Cooldown of a randomly initialised cell spheroid. Huge initial overlaps lead to arbitrary high velocities in the initial configuration **(a)**. These are handled by the global adaptive timestep algorithm **(b)**. Without proliferation, the corresponding velocities in the spheroid decrease **(c+d)**.

algorithm described in section 8.3. Since optimal packing of spheres in 3 dimensions is far from being a trivial task, the more suitable option of a Monte Carlo algorithm for initial cell insertion is used. This algorithm produces configurations with large overlaps. However, since the simulation comprises an adaptive timestep algorithm, the simulation stepsize is decreased until reasonable velocities are found and the initial configuration is equilibrated. An initial cooldown phase without cell cycle progression can be used at the start of each simulation to obtain the equilibrated system configuration. For an example of this cooldown see figure 9.2 for the velocity distribution or 9.3 for the visualisation.

9.2 Tissue sorting through cell interaction

Objects that show different interaction properties tend to separate when brought into a mixed state. This behaviour is also found on a larger scale, when considering mixtures of cells (see figure 7.5, which depicts the basic mechanisms at work). Cell separation has

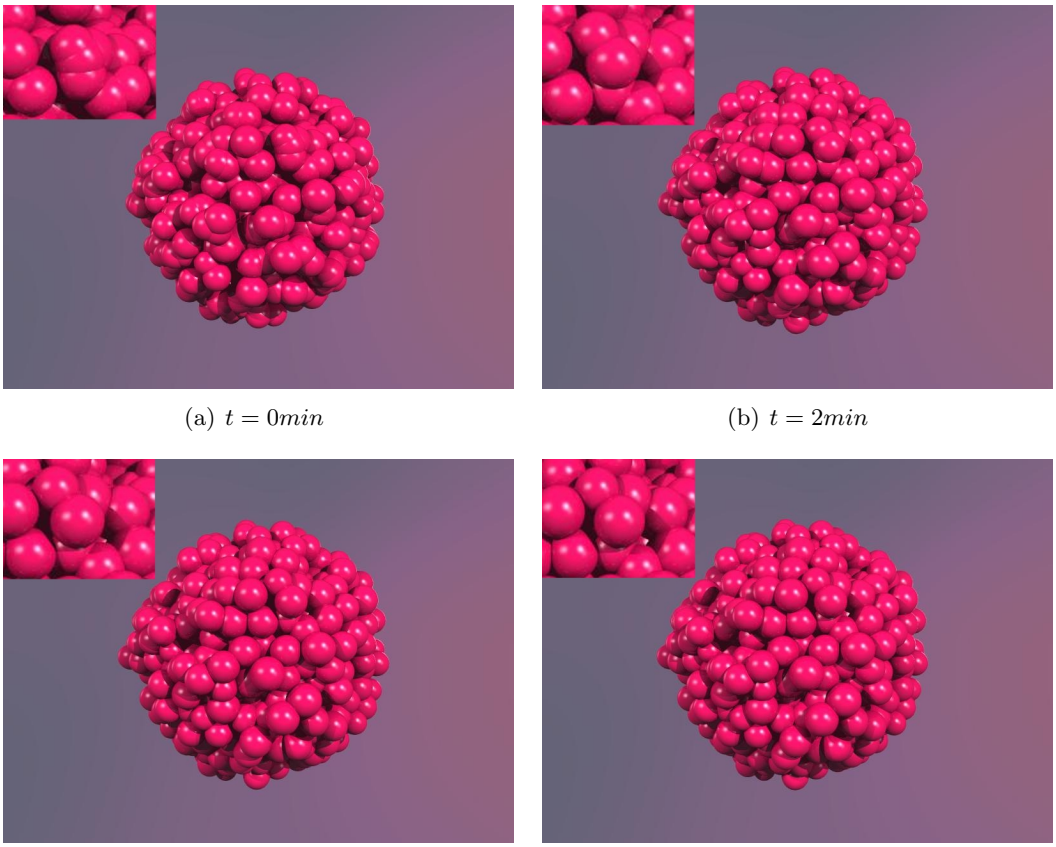

(a) $t = 0min$ (b) $t = 2min$

(c) $t = 4min$ (d) $t = 6min$

Figure 9.3: Cooldown of a randomly initialised cell spheroid seen in POV-Ray visualisation. Randomly inserted cells may show huge overlaps at $t = 0min$ in (a). Resulting dynamics are handled by the adaptive stepsize algorithms (global and local) which leads to a quick equilibration of the cell positions (b). After 4 minutes the spheroid is largely equilibrated, if cell growth and proliferation is neglected (c). Only small changes can be observed for the spheroid shown here at later time (d). Equilibration may take longer for larger systems, but the time is always negligible when compared to the typical overall simulation timescale.

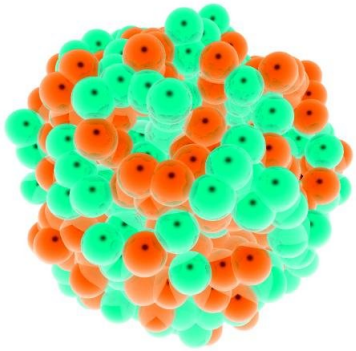

(a) initial random configuration after 15 minutes of interaction

(b) configuration after 735 mins - cluster formation starting

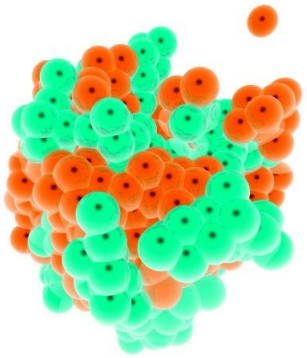

(c) configuration after 1485 mins - single cells might be separated temporarily from the population by their random walk

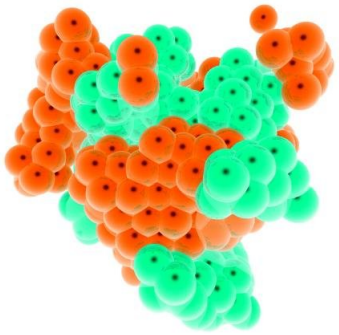

(d) configuration after 4485 minutes - dense cell packing with clusters moving as solid objects

Figure 9.4: Separation of cells with different surface energies including active cell movement. Interaction parameters between similar cells: $\nu = 0.5$; $E = 1Pa$; $\sigma = 0.5\text{nN}\mu\text{m}^{-1}$; between mixed cells: $\nu = 0.5$; $E = 1Pa$; $\sigma = 0.1\text{nN}\mu\text{m}^{-1}$. Cells repolarise (choose a new random movement direction) after 100 minutes - velocities for active movement are drawn from a random distribution with a maximum of $0.3\frac{\mu m}{min}$.

been modelled with great success using Potts model (*Graner and Glazier* (1992)). See figure 9.6 for a comparison of the Potts model results with results obtained within the agent-based approach of this thesis. Moreover, as described in section 7.2, the formation of organised tissue complexes during ontogenesis depends strongly on differential cell interactions. Therefore, cell separation is a suitable test system for the cellular interactions in the agent-based model.

Simulations show separation results in agreement with what is expected from real systems (see figures 9.4 and 9.5). Within the separation tests, cells are actively moving with a random velocity drawn from a distribution with a defined maximum. Upon contact between two cells of identical interaction properties, the cells form an aggregate due to coalescence. This is only mediated by the finite surface energy term, as depicted in equation 3.7. The aggregates grow with time and tend to become spherical to minimise

surface energy. Separation of cells from an aggregate is in principle possible, and can be observed in the simulation (see figure 9.5). The grade of de-mixing observed depends on the cells' temperature corresponding to the cells' velocity. Higher velocities lead to faster segregation into clusters of similar cells. However, overly high velocities lead to complete segregation of all cells, as the velocities get high enough for them to escape binding in a cluster.

The obtained results clearly show that the given simulation is able to capture the expected behaviour of a real interacting cell system. Differential adhesion and changes in connected cell parameters are of importance for the interaction of tumour tissue with its surroundings (in particular for invasion and metastasis; see *Conde-Ramis et al.* (2008) and *Anderson* (2005)), opening up the possibility to use the agent-based approach to examine these phenomena

.

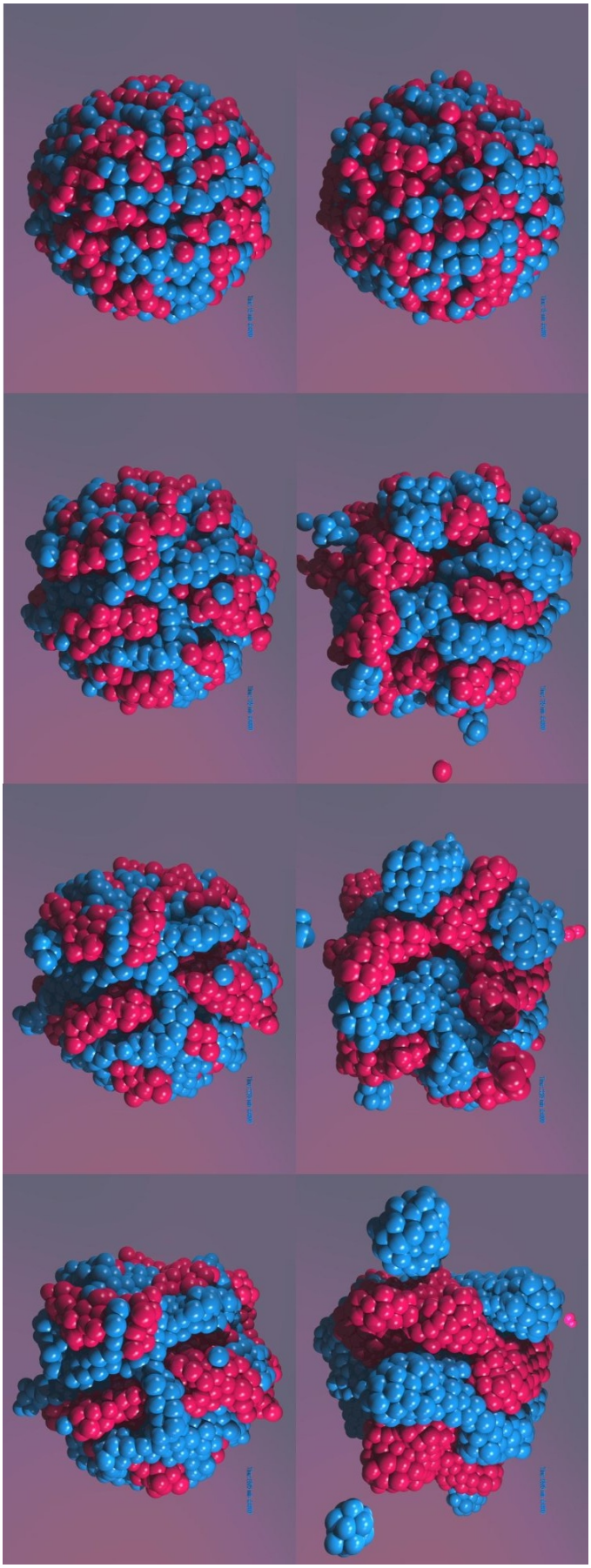

Figure 9.5: Cell separation due to different surface energies. JKR parameters for interaction between similar cells: $\nu = 0.5$; $E = 1\text{Pa}$; $\sigma = 0.5\frac{\text{nN}}{\mu\text{m}}$; between mixed cells: $\nu = 0.5$; $E = 1\text{Pa}$; $\sigma = 0.1\frac{\text{nN}}{\mu\text{m}}$. Visualisation after 30, 750, 2250 and 8520 min of dynamics (top to bottom). Two different cell "temperatures" were used, implemented through a random cell velocity drawn from a distribution with $|v_{max}| = 0.3\frac{\mu\text{m}}{\text{min}}$ for the left and $|v_{max}| = 1\frac{\mu\text{m}}{\text{min}}$ for the right series. The grade of de-mixing depends on the cell temperature. Higher velocities lead to faster segregation into clusters of similar cells.

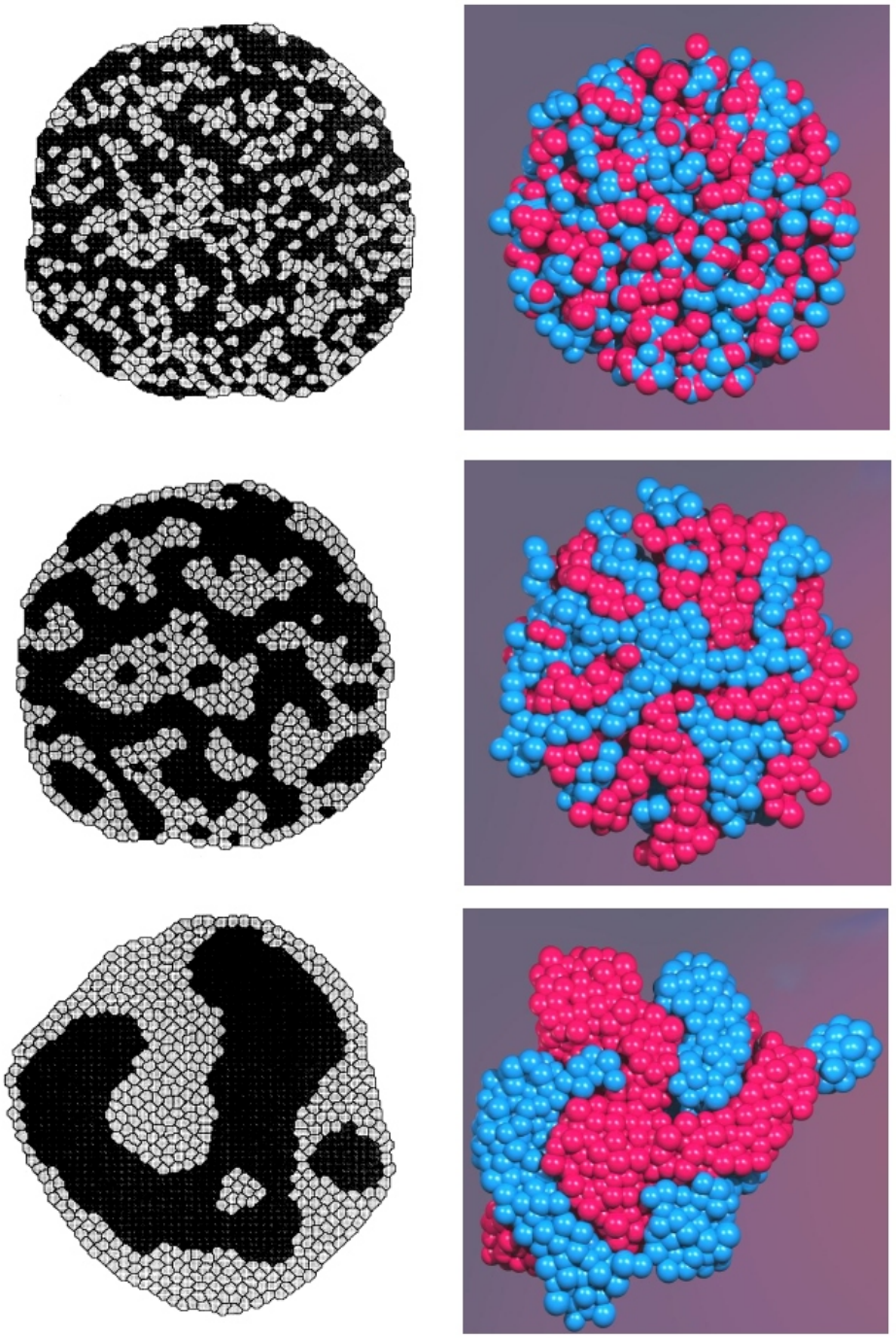

Figure 9.6: Cell separation within the current model compared to separation results obtained with the Potts model from *Graner and Glazier* (1992). Results from the agent-based simulation are given as lateral cuts through the cell cluster rearranging in 3D (right side; intial configuration on top, system after 330 min and 10000 min of dynamics below). Results from the Potts model are 2D (left side; initial configuration on top, system after 100 and 3000 Monte Carlo steps below).

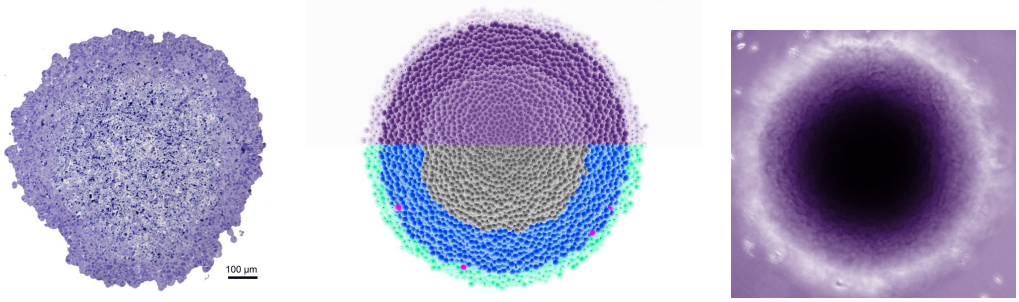

(a) (b) (c)

Figure 9.7: **(a)** Cross section of $1\mu m$ thickness through a tumour spheroid, showing the outer rim of viable cells and the necrotic core. **(b)** Cross section of a tumour spheroid simulation obtained with the application developed within this thesis. The Spheroid is comprised of about 100000 cells. The proliferating boundary, the necrotic core and the quiescent region in between are visible. Through agent-based modelling it is possible to stain the cells according to their actual cell cycle phase (lower half of the section). **(c)** Differential interference contrast picture of a tumour spheroid cross section. Images (a) and (c) taken from `http://www.vet.purdue.edu/cristal/oci-info.htm`

9.3 Avascular Tumour growth

MCTS growth

Multicellular tumour spheroids (MCTS) are three dimensional cultures of cancerous proliferating cells which can be studied as a model system of avascular tumour growth. The basic mechanisms which govern their growth were introduced in section 1.2. As MCTS show a distinct topology as a result of nutrient concentration and cell dynamics, this topology, shown in figure 1.2, should be reproducible by an agent-based model as a starting point for further investigation of tumour dynamics.

Simulations can start with a single cell entered into the system in a random cycle phase (of interphase). This cell will start to proliferate and eventually form cell colonies which comprise up to $\mathcal{O}(6)$ cells within a simulation run. Cells in the spheroid take up nutrients for biomass conversion in their metabolism. This is handled in the model via a reaction diffusion system, as described in section 5.4. Exemplary results for these nutrient dynamics are shown in figure 5.11. The core of the spheroids will usually consist of necrotic cells, due to extreme nutrient depletion in the inner tumour volume. An interlayer of quiescent cells is generated either through comparison of nutrient availability or pressure on a cell to the respective threshold value C_{G0} or P_{crit} at the restriction point (G_1/S-transition). Unless otherwise noted a nutrient-induced quiescence was used throughout the simulations.

Visualisations shown are generated with POV-ray and depict lateral cross sections of the spheroids. Cell properties such as cycle phase, pressure and mitotic status are stained in colour. The material presented here is exemplary, more data including videos of the tumour dynamics is available upon request.

The visualised results e.g. in figure 9.8 show a formation of the typical layered MCTS

morphology as seen in histological results (see figure 9.7).

The spheroid is growing uniformly up to a threshold of about 6000 cells. Cell cycle phase synchronisation is declining only slowly over time due to the low randomisation of the phaselengths (drawn form an uniform distribution with a width of 30% up and down). Only few cells re-entering the cycle from quiescence are observed in this run. Therefore their contribution to desynchronisation is small. If an uniform phaselength distribution with higher width is used, desynchronisation can be reached within few cell cycles.

Limited nutrient availability leads to the rise of a quiescent core shown in figure 9.8(b). From this point on the tumour is deviating from its projected exponential growth curve depicted by the dashed line in figure 9.9. This curve models the tumour growth assuming a simple exponential growth, also referred to as the Malthusian growth in population dynamics. It can be defined by

Equation 8 (*Malthusian growth model*)

$$X(t) = X(0)\mathrm{e}^{\mathrm{rt}} \tag{9.3}$$

where $X(t)$ is the population size at time t, $X(0)$ the initial population size and r the growth rate (corresponding to the inverse of the cell cycle time).

Of course this simple model cannot take into account effects of limited nutrient availability, but in the initial growth phase of the tumour such effects are not present. More sophisticated models, like the Gompertz model are well suited to model the advanced growth stages of a tumour (see *Lo* (2007), *Castorina et al.* (2007) and section 11.4 in the appendix).

Within the simulation, continued growth of the boundary layer of active cells eventually leads to the onset of necrosis. This happens when the nutrient concentration in the core drops below the defined threshold C_N for the induction of necrosis. From this point on the growth of the tumour spheroid might get close to a saturation, due to mitotic inactive cells in G_0 and dead cells in N balancing the mitotic activity of the outer tumour layer of dividing cells. The thickness of the different cell layers depends on the threshold values C_{G0}, C_N and P_{crit}.

The simulation run depicted in figure 9.8 used a critical nutrient threshold to send cells into quiescence at the restriction point. An alternative approach can be implemented via the cell pressure, as described in section 7.3. This was done for the simulation run shown in figure 9.11. Including this mechanism the growth is deviating from the simple projection done with the help of equation 9.3 right from the start. Onset of necrosis in this run was due to a combined critical nutrient threshold for glucose and oxygen ($C_{comb} = C_{gl}C_{ox}$) determined in *Schaller* (2006). However the critical nutrient threshold of $C_{comb} = 0.035 mmol^2$ was not undercut within the simulation run, therefore no necrosis was observed.

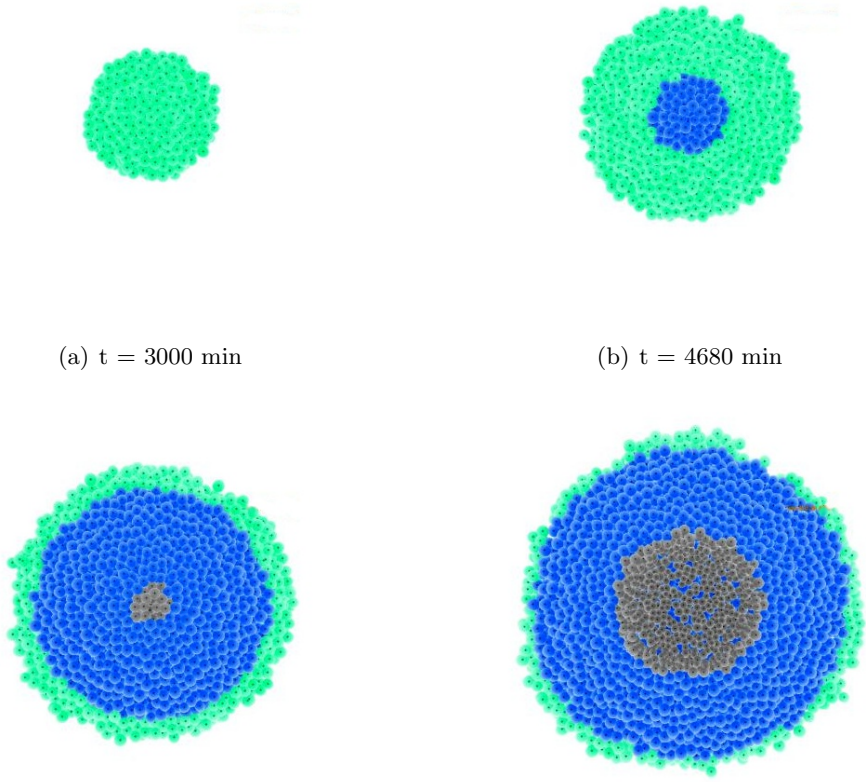

(a) t = 3000 min

(b) t = 4680 min

(c) t = 6030 min

(d) t = 8460 min

Figure 9.8: Growth of a multicellular tumour spheroid visualised with POV-ray. The growth curve associated with this run is depicted in figure 9.9. Spheroid is growing uniformly up to a threshold of about 6000 cells in **(a)**. Limited nutrient availability leads to the rise of a quiescent core shown in figure **(b)**. Continued growth of the boundary layer of active cells eventually leads to the onset of necrosis, due to nutrient depletion in the inner core, at a tumour size of about 14000 cells **(c)**. This leads to a final state of growth saturation where necrotic death in the tumour centre is balanced by mitotic activity of the boundary layer **(d)**. Colour code: quiescent cells (G_0) in blue, viable cells (G_1, S, G_2) in turquoise, necrotic cells (N) in grey.

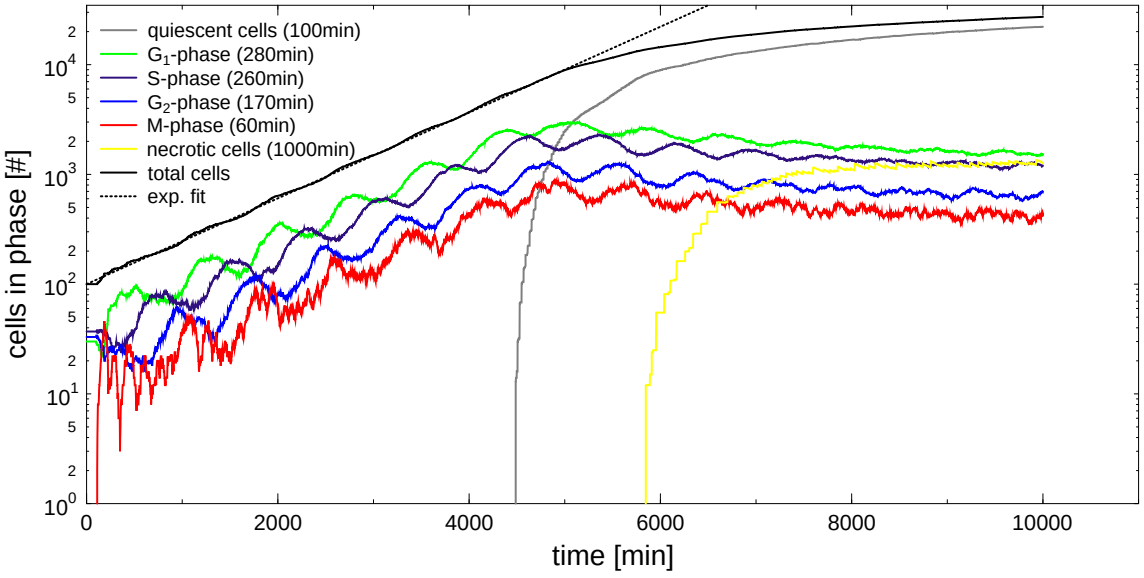

Figure 9.9: Growth curve for the multicellular tumour spheroid visualised in figure 9.8. Depending on the thresholds for the induction of quiescence (C_{G0}) and necrosis (C_N) the tumour is dominated by a large population of quiescent cells. Due to the composition of the tumour in spherical shells the amount of quiescent cells in the intermediary layer (with a larger radius) will always be bigger than the amount of necrotic cells.

According to the observed deviation from exponential growth pressure inhibition alone could suffice to reach a growth saturation within the tumour spheroid. However, this question is the target of further investigations.

Growth curves compared to experimental results

Data obtained within the simulation is compared to experimental growth curves in figure 9.12. Experimental data was taken from *Freyer and Sutherland* (1986): within these experiments the oxygen and glucose concentration on the system boudary was fixed during the cultivation of EMT6/Ro multicellular tumour spheroids. Dependence of growth saturation and onset of necrosis upon the nutrient concentrations were studied. Data in *Freyer and Sutherland* (1986) comprises tumour radius and cell number estimates for two different populations, therefore the error of the growth curves is supposed to be high. Extraction of the datapoints was done with the help of scah2.6 `http://th.physik.uni-frankfurt.de/~drescher/soft/scah2.6`.

The nutrient conditions were modelled to suit the ones used in the experiment of *Freyer and Sutherland* (1986), using Dirichlet type boundary conditions as described in section 5.4 (glucose concentration of 16.5 mMol, oxygen concentration 0.28 mMol). A quiescence threshold depending on a single nutrient concentration (glucose) was used in addition to the growth-induced quiescence depending on cell pressure. Necrose was induced upon undercut of a critical glucose threshold defined by C_N.

The simulation results correspond to the results obtained experimentally. However,

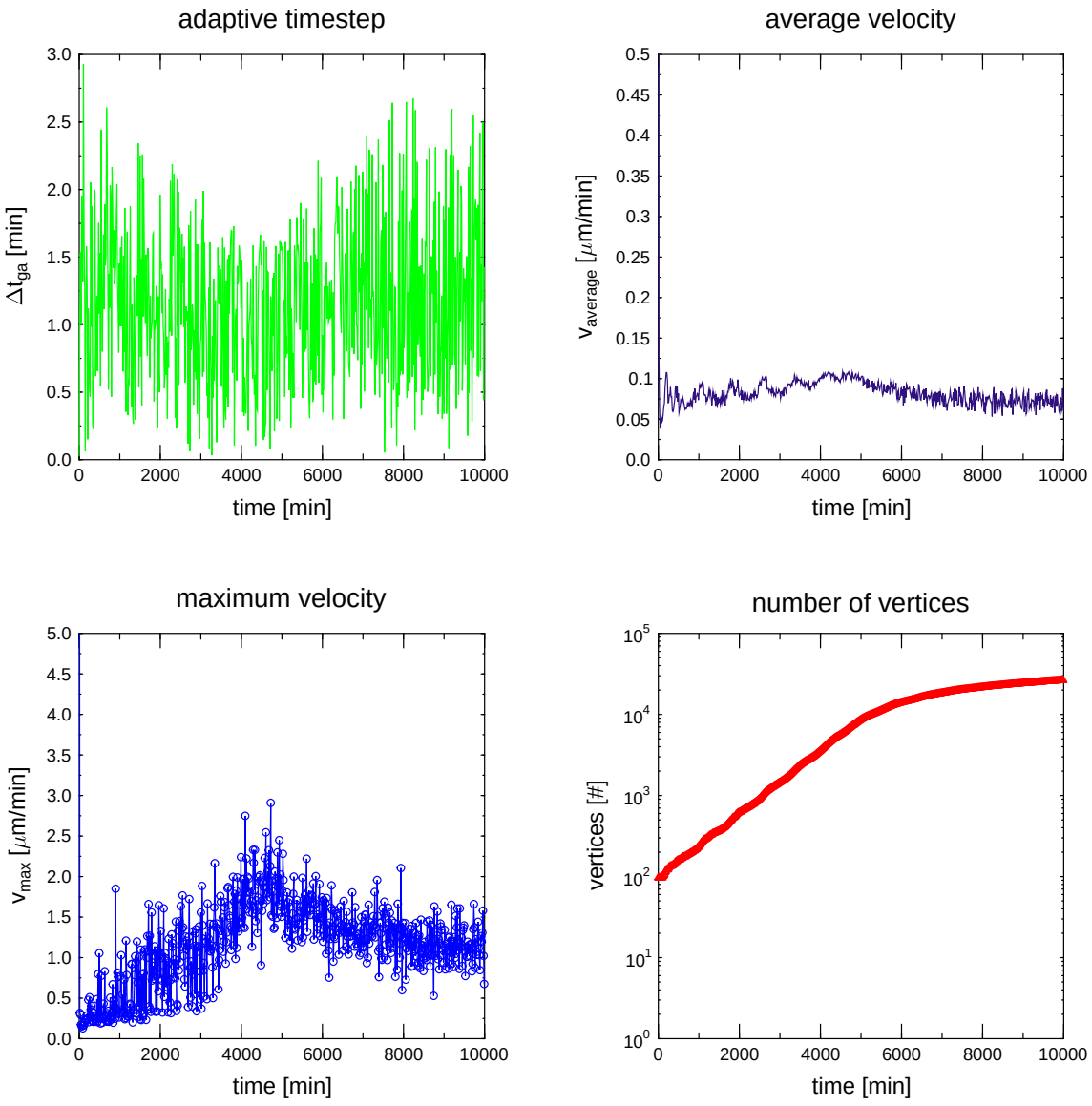

Figure 9.10: Runtime statistics for the simulation run of the multicellular tumour spheroid visualised in figure 9.8. Timestep for propagation of the system is controled by the global and local adaptive timestep algorithms described in section 4.3. Average cell velocity is dominated by velocities resulting from mitotic separation forces and cell growth. Maximum cell velocity v_{max} is rising with the pressure inside the tumour. Upon onset of quiescence v_{max} is falling again due to reduced growth inside the tumour volume.

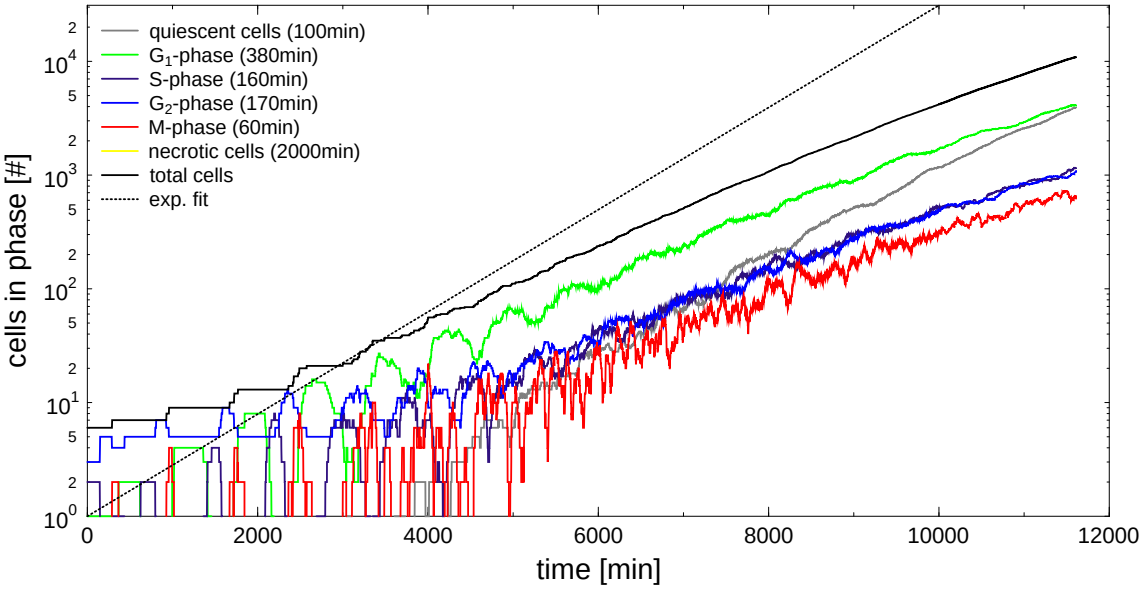

Figure 9.11: Growth curve for a multicellular tumour spheroid growing under the restriction of pressure-induced quiescence as described in section 7.3. Overall growth of the tumour is deviating from the simple exponential growth projection right from the start due to cells being sent to quiescence. Initial configuration consisted of one malignant and four quiescent cells, explaining the initial deviation from exponential growth (before 3000 min).

there are significant deviations which are to be discussed.

All simulation results shown are derived from agent-based models starting with a single malignant cell. Therefore the initial growth is exponential and following the projected growth (given by equation 9.3). Simulation I and II are growth curves obtained with the application developed within this thesis. Simulation III is a growth curve from the agent-based model of *Schaller* (2006), presented here for comparison of the used mechanisms.

When compared to growth curves obtained within this thesis (I+II), the growth curve of simulation III shows a qualitative different behaviour in respect to the curvature between 8 and 12 days. The correspondence of simulation III with the experimental data is higher, suggesting that the mechanism in use are better suited to model the tumour growth. The main difference between simulations I+II and simulation III is the cause of quiescence and necrose. Within the simulation III, quiescence is induced by overly cell pressure ($P_{crit} = 600Pa$; cell radius $r_{tar} = 5\mu m$). Although simulations I and II include an additional mechanism for the induction of quiescence in the form of a critical nutrient threshold C_{G0}, their growth exceeds the growth observed in simulation III. This might be a result of the different cell pressure threshold used ($P_{crit} = 300Pa$; cell radius $r_{tar} = 14\mu m$) or of the dependece of necrosis on a single nutrient (glucose) instead of a critical product of two nutrients.

However, the growth curves obtained within agent-based modelling approaches are in good correspondence to the experimental ones. This shows that the main mechanisms of tumour growth were successfully modelled. An enhanced derivation and implementation

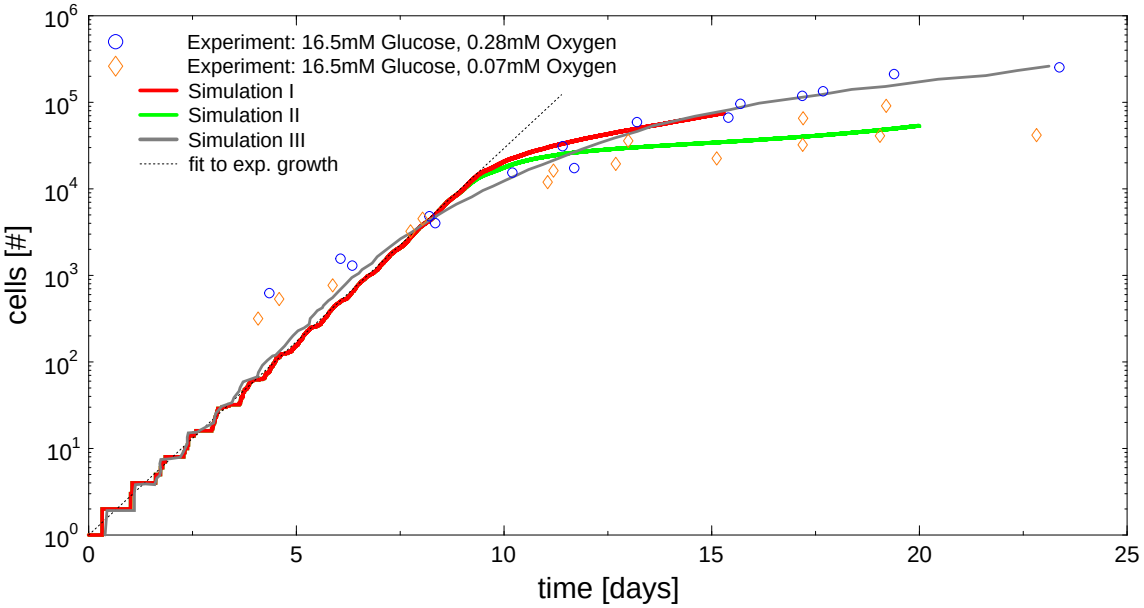

Figure 9.12: Comparison of growth curves from agent-based simulations within this thesis (Simulation I + II) and *Schaller* (2006) (Simulation III) to experimental results from *Freyer and Sutherland* (1986). Discussion of results within the text. Values extracted from *Freyer and Sutherland* (1986) with the help of scah2.6 `http://th.physik.uni-frankfurt.de/~drescher/soft/scah2.6`.

of growth parameters from experimental results would further improve this correspondence (see section 11.2).

9.4 Fingering of tumours

Tumour spheroids may show a certain degree of irregular growth. This phenomenon, called fingering, is discussed in the literature (see *Anderson et al.* (2006) and *Macklin and Lowengrub* (2007)). If the growth of the spheroid is affected by a deviation from spherical symmetry, this protuberance finds perfect nutrient conditions outside of the spheroid. This adds a bias to the global growth of the spheroid and leads to the formation of a "finger" on the tumour surface.

This phenomenon is also visible in agent-based simulations of tumour growth, as depicted in figure 9.13. The driving mechanisms behind the formation of the finger are the same as in vivo. Cells leaving the boundary surface of the tumour are always subject to optimal nutrient conditions and experience only small pressure forces from few neighbouring cells (according to equation 7.7) at the same time. The fingering occurs even though the mechanism for boundary pressure, described in section 7.2, is in use. Within this approach every cell on the boundary layer of the spheroid (a situation which can be easily detected with the help of the triangulation) is affected by a small force of 1nN towards the origin (corresponding to the spheroid centre). This imposes a penalty on the formation

of protrusions, but they nevertheless can be observed in the simulation. Fingering results are reproducible, as shown in figure 9.14.

Proliferating cell fronts of the fingers consume a high amount of nutrients, reducing the concentration below the threshold necessary in order to re-enter the cycle from quiescence. Therefore, cells within the indentations stay in quiescence.

Parameters leading to an increased development of protrusions throughout the tumour growth are of great interest, since they are of importance for invasion and separation of parts from the tumour in metastasis (see also figure 9.15).

The main difference between the runs showing distinctive fingering and the ones with low levels of fingering was the usage of a prolonged phase-synchronisation of cells within the former ones. Increased synchronisation lead to a growth of the tumour in spurts. Cycle phaselengths were not drawn from a random distribution, but rather used as given in the parameter file. Therefore, the only mechanism leading to desynchronisation of cell growth is found in quiescent cells which re-enter the active cycle phases. While these cells are present within the simulation runs under consideration, their number remains extremely small compared to the overall cell count.

The effects of cell cycle synchronisation on the dynamics of the tumour development are therefore of interest for further investigations.

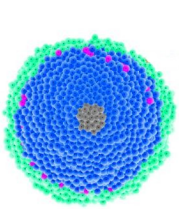

(a) Spherical tumour symmetry after t = 6000 min.

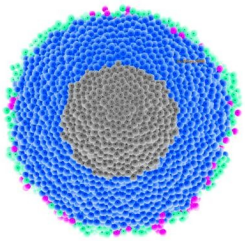

(b) Random development of a irregularity after t = 9250 min.

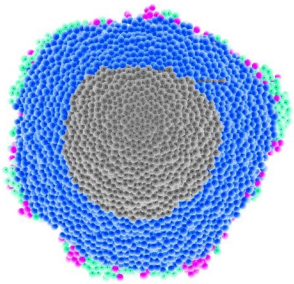

(c) Continued growth of the protuberance after t = 12300 min.

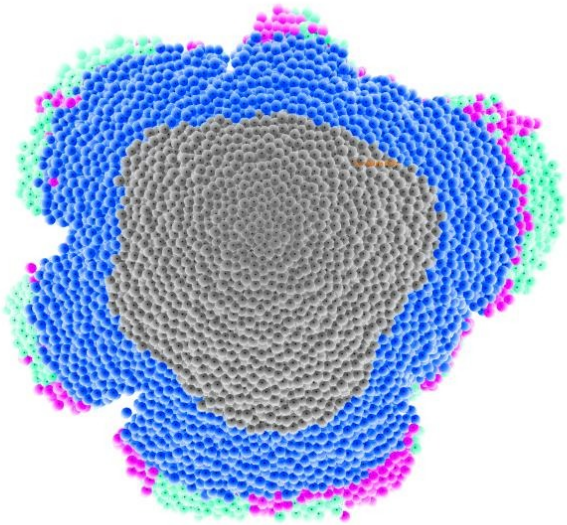

(d) Fingering of the tumour after t = 15700 min.

Figure 9.13: Tumour spheroids may show a certain degree of irregular growth (described as "fingering" in the literature). If the growth of the spheroid is affected by a deviation from spherical symmetry this protuberance finds perfect nutrient conditions outside of the spheroid. This adds a bias to the global growth of the spheroid and leads to the formation of a "finger" on the tumour surface. Final spheroid shown comprises about 150000 cells. Cell colour: green (G_1,S,G_2), red (re-entered from G_0), blue (G_0), grey (N). Cells send into G_0 due to a critical nutrient threshold.

(a) Spherical tumour symmetry after t = 5800 min.

(b) Random development of a irregularity after t = 8500 min.

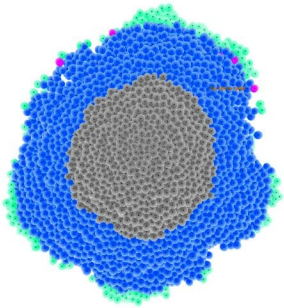

(c) Continued growth of the protuberance after t = 12000 min.

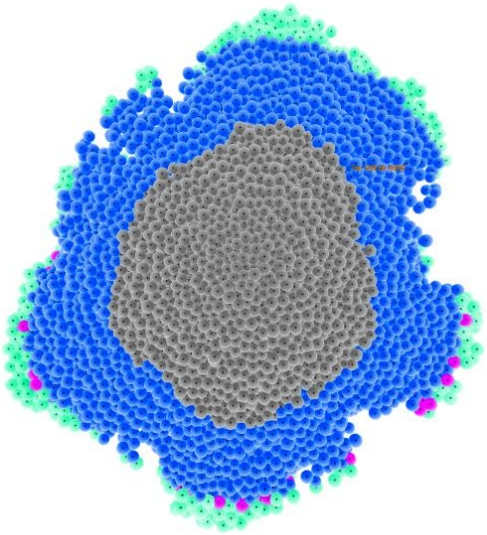

(d) Fingering of the tumour after t = 14250 min.

Figure 9.14: Reproducability of irregular growth (fingering) in tumour spheroids within a agent-based model. Derivation from spherical symmetry may lead to a protuberance that tend to grow due to better nutrient conditions outside of the tumour volume (shown in figure 9.13). This penomenon is reproducible for different parameter sets. Final spheroid shown comprises about 51000 cells. Cell colour: green (G_1,S,G_2), red (re-entered from G_0), blue (G_0), grey (N). Cells send into G_0 due to a critical nutrient threshold.

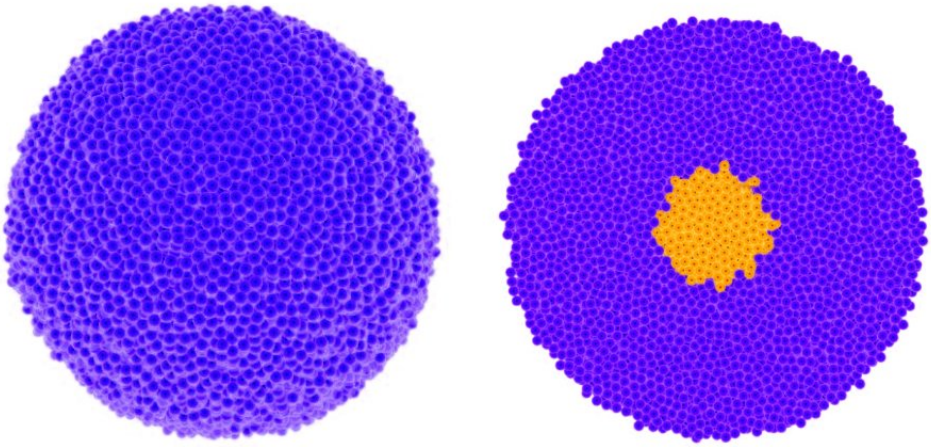

Figure 9.15: Simulation of the initial stage of an avascular tumour spheroid surrounded by healthy tissue (about 41.000 cells in total). Malignant core started with a single cell and shows an invasive mixing with the surrounding benign tissue upon proliferation.

10 Modelling tumour therapy with hadrons

Particle therapy is a form of external beam radiotherapy that uses beams of protons, neutrons, or atomic nuclei. In order to distinguish the therapeutical use of these particles from the use of photons and electrons, particle therapy is also referred to as hadron therapy (if it makes use of protons and neutrons) or heavy ion therapy (if it makes use of more massive particles, such as carbon nuclei). There are few cases where conservative methods of radiation treatment with photons and electrons are preferable, for example tumours of the eye or tumours with low penetration depths in general. Conservative methods are also available at lower costs, and require less technical equipment, as usually no linear accelerator or synchrotron is needed. However, in the majority of cases, heavy ion radiation is superior to conservative treatments, due to the many advantages that will be discussed throughout this chapter. As treatment costs are decreasing its general availability is rising, with heavy ion therapy centres under construction throughout the world (e.g. the HIT, Heidelberg [1] going online in fall 2008).

Investigation and realistic modelling of the processes involved is therefore of high interest. The important mechanisms for therapeutical success are discussed within this chapter.

A very wide variety of tumours can be effectively treated with hadron therapy, including all solid tumours (e.g. in the brain, lung, skin or stomach). Due to the fact that, in hadron therapy, the radiation dose can be deposited very precisely with only limited effects on the surrounding tissue, it is also suited to be used in treatment of tumours which are located next to vulnerable regions, such as the CNS.

Treatment of tumours with heavy ions (such as carbon) has shown to be a promising therapy for inoperable tumours. First trials started in 1997 at the GSI, Darmstadt[2] and the success rate was outstanding, with tumour growth stopped in 75-90% of all cases.

Heavy ions exhibit a multitude of advantages and characteristics favourable to radiation therapy, such as:

- Preferable dose distribution
- High Relative Biological Effectiveness (RBE) because of high linear energy transfer (LET)
- Smaller dependence on oxygen concentration

[1] `http://www.klinikum.uni-heidelberg.de/Heidelberger-Ionenstrahlen-Therapie-HIT.1165.0.html`

[2] `http://www.gsi.de/portrait/Broschueren/ionenstrahlen_e.html`

Radiation type	Interaction mechanism	Comment
γ	Photoelectric effect	Low energy ($E \leq 0.1MeV$)
	Compton effect	Mid-energy ($0.05MeV \leq E \leq 1MeV$)
	Pair production	High energy ($1MeV \leq E \leq 6MeV$)
β	Ionisation	
	Bremsstrahlung	
	δ-electron production	
Charged particles	Ionisation	
	Nuclear interaction	

Table 10.1: Important interaction mechanisms of radiation (not exhaustive).

- Reduction of cell repair due to cluster damage
- Less variation in radiosensitivity throughout the cell cycle

These advantages will be explained in the following chapter.

10.1 Properties of particle radiation

Heavy-ion beams offer favourable properties for treatment, especially for deep-seated local tumours. In contrast to photon beams, they have an inverted depth-dose profile (Bragg curve) and the narrow Bragg peak can be adjusted precisely to the desired depth by variation of the beam energy. In addition, ions heavier than protons offer an enhanced biological effectiveness in the Bragg peak region, which can be explained by the very dense ionisation towards the end of the particle track. In order to understand the special properties of particle radiation, the interaction mechanisms of radiation with matter have to be introduced briefly.

Interaction of radiation with matter

Radiation can interact with matter in a multitude of ways, with some of the important ones for hadron therapy depicted in table 10.1.

Ionisation is one of the most important mechanisms for the interaction of radiation with a cancerous cell. In the most common case, a positively charged ion is produced when an electron bonded to an atom absorbs enough energy to escape from the electric potential barrier that originally confined it. The energy required for this process is called the ionisation potential. In order for a particle to be ionising, it must both have a high enough energy and interact with an atom of the target. Photons and charged particles such as electrons, positrons, and alpha particles interact strongly with atoms and molecules, so they can be ionising. An ionisation event normally produces a positive atomic ion and an electron.

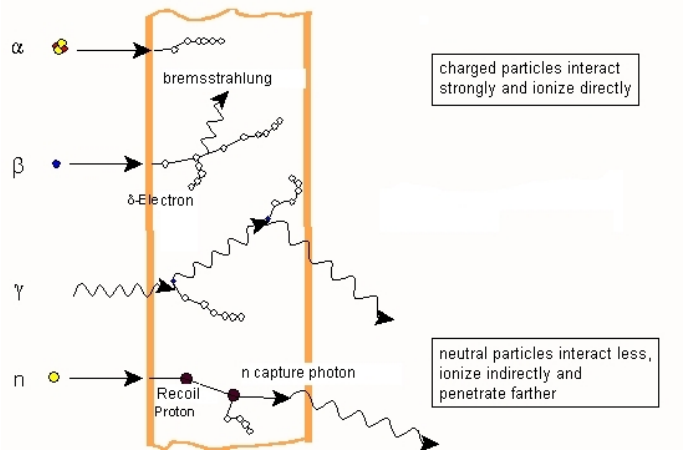

Figure 10.1: Interaction mechanisms for α (nuclei), β (electron), γ (photon) and neutron particles with matter as explained in section 10.1. Image is in open domain under terms 2.

Neutrons do not interact strongly and therefore do not cause ionisation directly. However, neutrons may collide with protons of the target material, which then turn into fast and ionising recoil protons. Eventually neutrons may be captured by a nucleus in a (n,γ)-reaction, leading to a neutron capture photon being released.

High-energy beta particles may produce bremsstrahlung, or secondary electrons (delta-electrons) when passing through matter; both can ionise and thus broaden the ion track in tissue.

Gamma rays do not ionise all along their path, but rather interact with matter in one of three ways: the photoelectric effect, the Compton effect, and pair production (see table 10.1). Through the photoelectric effect electrons are emitted from matter after the absorption of energy from electromagnetic radiation such as gamma rays. In a Compton scattering event, the gamma ray transfers energy to an electron, and it continues on its path in a different direction with reduced energy. Pair production is the creation of an elementary particle and its antiparticle. This is allowed provided that there is enough energy available to create the pair and that both energy and momentum can be conserved (e.g. when a nucleus is present).

If radiation consisting of nuclei is interacting with matter, nuclear reactions along the penetration path lead to a fragmentation of the initial nucleus and a build-up of lower-Z fragments with increasing penetration depth. These fragments are responsible for the tail distribution seen in figure 10.2. This tail develops due to the fact that the range of the particles scales with Z^2 according to the Bethe-Bloch formula (equation 10.1). However, this tail distribution is relatively small for the common case of carbon ions. Furthermore, the fragmentation can be used in Positron emission tomography-techniques (PET) for in-vivo location of the Bragg peak as described later on.

Obviously there is a multitude of possible mechanisms which mediate the interaction between heavy ions and tissue. However, since it will only be possible to model a simplified system of interactions, within this thesis most mechanisms were not implemented directly.

Energy deposition profile and LET

In contrast to photons, charged particles deposit most of their energy at a specific depth inside the tissue depending on their energy. This region at the end of their track is the so called Bragg peak. The phenomenon can be understood with the help of the Bethe-Bloch formula, which describes the energy-loss by ionisation of swift charged particles (protons, alpha particles, atomic ions, but not electrons) traversing matter.

Charged particles moving through matter interact with atomic electrons in the material. These interactions may lead to excitation or ionisation of the atoms. The Bethe formula, found by Hans Bethe in 1930 (see *Bethe* (1930)), describes the energy loss per distance traveled:

Equation 9 (*Bethe-Bloch formula*)

$$-\frac{dE}{dx} = \frac{4\pi}{m_e c^2} \cdot \frac{nZ^2}{\beta^2} \cdot \left(\frac{e^2}{4\pi\varepsilon_0}\right)^2 \cdot \left[\ln\left(\frac{2m_e c^2 \beta^2}{I \cdot (1-\beta^2)}\right) - \beta^2\right] \tag{10.1}$$

with $\beta = v/c$, v *velocity of the particle,* E *energy of the particle,* x *penetration depths,* c *speed of light,* $Z\,e$ *particle charge,* e *electron charge,* m_e *rest mass of the electron,* n *electron density of the target,* I *mean excitation potential of the target, and* ε_0 *permittivity of free space.*

The electron density of the material can be calculated by $n = \frac{N_A \cdot Z \cdot \rho}{A}$, where ρ is the density of the material, Z, A the atomic number and mass number, and N_A the Avogadro number.

A depth-dose profile (Bragg curve) resulting from equation 10.1 exhibits a flat plateau region in the entrance channel and a distinct peak near the end of the particles' range (depicted in figure 10.2 and 10.3). This dose deposition behaviour of heavy ions is one of their major advantages in radiotherapy.

In photon radiotherapy, on the other hand, the dose is deposited in stochastical interactions along the whole path of the radiation, which confers a high dose to healthy tissue in the entrance channel (compare figure 10.4).

Low lateral scattering of heavy ions allows for an improved dose conformity inside the tumour. This again results in a lower integral dose deposited in the healthy tissue surrounding the tumour, tremendously reducing the probability of developing secondary cancer. Heavy ion therapy is thus favourable for tumours in the vicinity of sensitive or vital organs.

Linear energy transfer (LET)

The linear energy transfer (LET) is a measure of the energy transferred to material as an ionising particle travels through it. According to the behaviour of heavy ions, the LET is greatly increased at the end of the ion's track. The LET is usually expressed in units of $keV/\mu m$.

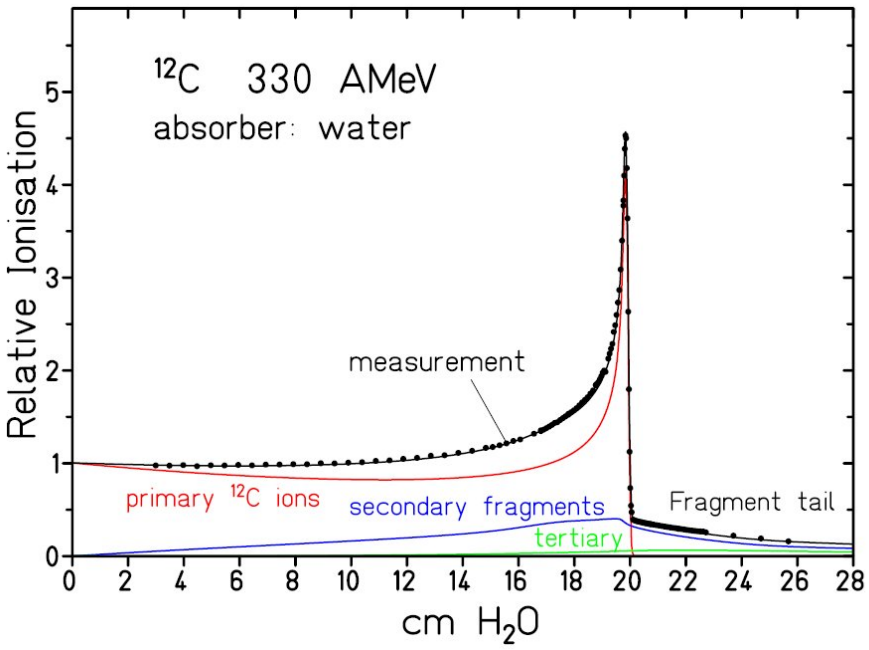

Figure 10.2: Deposition profile for a carbon beam in water measured at GSI, Darmstadt. Deposition follows a Bragg curve as defined by the Bethe-Bloch formula (equation 10.1). Fragmentation of the ion projectile is visible through the generation of secondary and tertiary fragments. The data points are compared to a model calculation (solid lines). From *Schardt and The Heavy-Ion Therapy Collaboration* (2007).

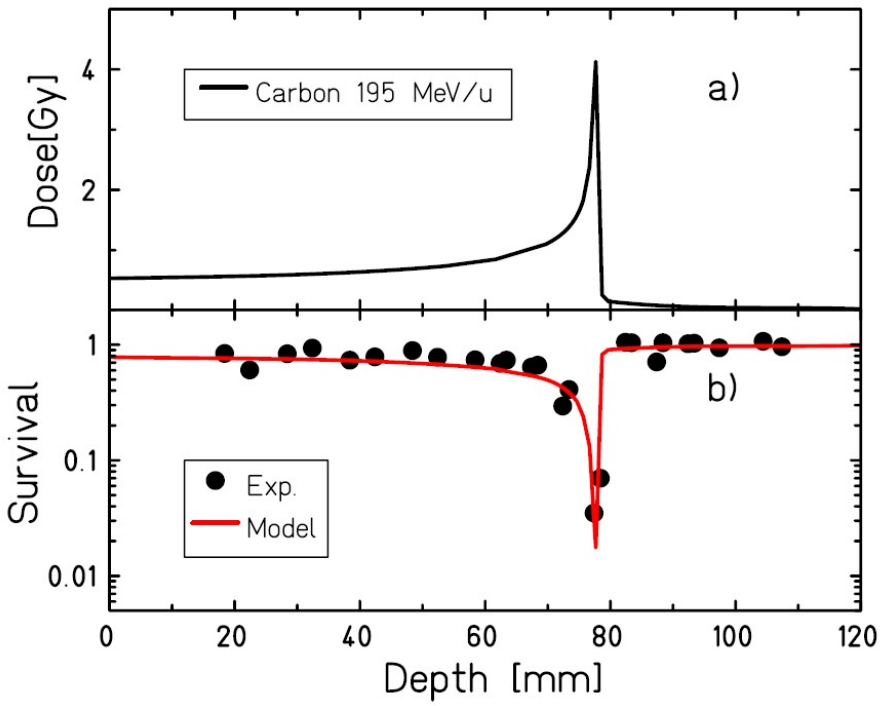

Figure 10.3: (a) Calculated depth-dose profile for a $195 MeV/u$ ^{12}C beam. (b) Survival of Chinese Hamster Ovary cells (CHO) as function of depth in water. From *Schardt and The Heavy-Ion Therapy Collaboration* (2007).

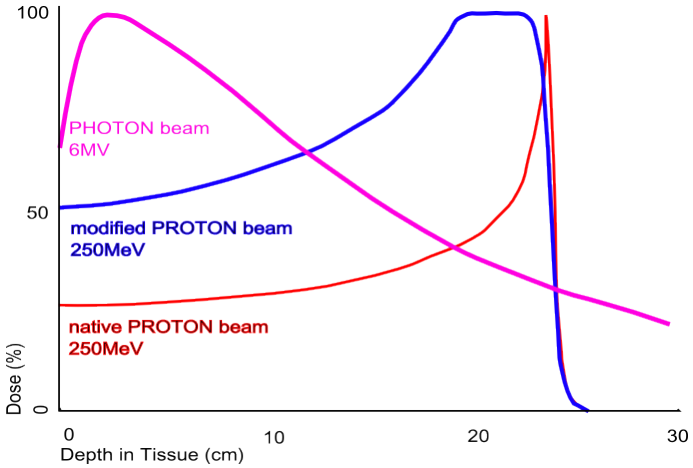

Figure 10.4: Dose deposition curves for different types of radiation. Note that photons deposit their energy in a multitude of stochastic interaction processes yielding a exponentially decaying profile. Within hadron therapy particles such as protons show an inverse deposition profile with a distinct Bragg peak according to equation 10.1. This behaviour results in a great advantage for therapeutical use of hadrons.

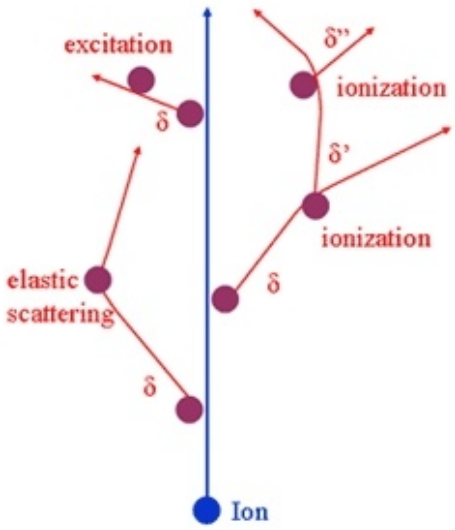

Figure 10.5: Ion track structure showing the generation of δ-electrons and ionisation events. Figure from `http://www.gsi.de/forschung/bio/delta_electron_e.html`.

Ion track and secondary particle production

An accelerated heavy ion penetrating tissue usually triggers a cascade of events (shown in figure 10.5). About two thirds of the dissipated energy is transformed into kinetic energy of δ-electrons (see *Surdutovich et al.* (2008)). These then produce secondary and tertiary ionisation processes around the ion's trajectory, which form the ion track. The energy spectrum of the emitted delta-electrons determines the diameter and the local dose inside the track. This cascade is the main reason for the great difference in biological effect when comparing e.g. photons and ions in radiation treatment (see *Kraft et al.* (1999)). According to the energy deposition profile of heavy ions, the majority of energy loss occurs at the end of the ion's track. This means that most of the events are also triggered at large penetration depths.

A multitude of Monte Carlo methods (SHIELD-HIT, FLUKA, GEANT, PHITS) are in use for transport calculations in human tissues. Therefore, the energy deposition in heavy ion irradiation can be studied with the help of sophisticated model kits for particle interaction such as GEANT4 (as it is done e.g. in *Pshenichnov et al.* (2005)).

From LET to Relative biological effectiveness of radiation

The relative biological effectiveness (RBE), that describes the impact of radiation on tissue, is drastically increased for ions with $Z \geq 2$ as compared to protons. That is why ions heavier than protons are called "heavy ions" in radiobiology, although they are light compared to those referred to by the same terminology in nuclear physics.

The main reason for an elevated RBE is the increase in ionisation density in the individual tracks of the heavy particles, where DNA damage becomes clustered (see *Kraft et al.* (1999)). For carbon ions the strongly elevated RBE region is restricted to the end of the particle range, while in the entrance channel DNA damage that can be repaired predominates. The basis for the increased RBE of heavy ions is the localised dose deposition, that

leads to the production of clustered DNA lesions which are difficult to repair (visualised in figure 10.6). They can be indirectly visualised in nuclei of mammalian cells by microscopy of immuno-stained repair proteins recruited to the damaged sites (see figure 10.7).

Because RBE depends on the possibility to repair the damage produced in the DNA, the repair capacity of the irradiated tissue becomes relevant. In general, slowly growing tumours have a great repair capacity and are normally very radioresistant. For ion treatment they show the greatest increase in RBE. This is why these tumours are most appropriate for a therapy with carbon ions.

During treatments the actual physical dose has to be adjusted to the RBE by an iterative procedure, in order to achieve a homogeneous biological effect.

10.2 Effects of heavy ion radiation on the cell

As introduced in the previous section, there exists a multitude of interaction mechanisms on the sub-nuclear and nuclear level for heavy ions and matter, either for the primary nucleus, its fragmentation parts or secondary particles. This spectrum results in multiple ways how irradiation with heavy ions can affect a cell.

The main mechanism of action is the irreparable damage of DNA in cells that lie within the treated area. As in chemotherapy, the ability of healthy cells to repair DNA damage is superior to cancerous cells, further limiting the effects of radiation treatment on surrounding tissue. For this reason radiation therapy is usually given in fractions, allowing healthy tissue to recover between the treatments.

If the dose of irradiation is very high, the effect of irradiation on tissue may be seen immediately, in the form of radiation poisoning. Lower doses, as applied in therapeutical irradiation, have more subtle effects.

DNA damage

The radiobiological efficiency of charged particles is mainly characterised by their local ionisation density, which can directly be correlated to the local density of DNA damage.

Heavy ions (especially carbon) at high energies have a sufficiently low ionisation density in the entrance region, and act mainly like photons, i.e. producing mostly repairable DNA damage. Due to the particles slowing down towards the Bragg peak the ionisation density increases significantly, resulting in severe cluster damage to the DNA (see figure 10.3 for actual survival rates and *Scholz and Kraft* (1996) for detailed description of the underlying mechanisms).

DNA damage may come in various degrees, ranging from single strand breaks (SSB) over double strand breaks (DSB) to severe cluster damage (CD). In general, SSBs can be repaired by the cell without problems due to the redundancy of the genetic code. DSBs are usually more severe events for the cell. They may result in wrong recombinations of the DNA or even complete inability of the cell to repair the damage. In that case, the cell

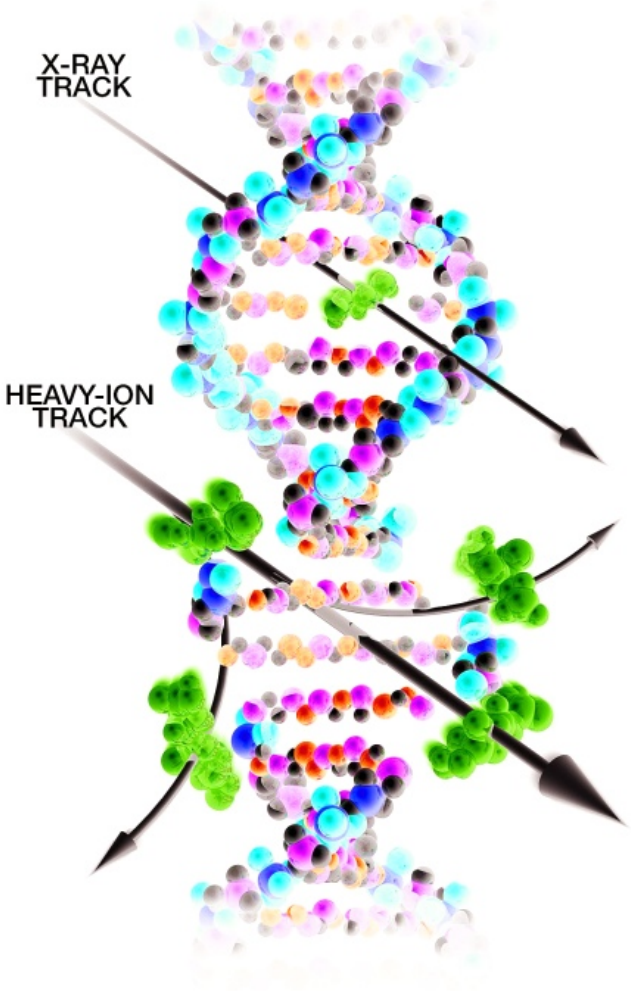

Figure 10.6: Damage to a DNA helix due to different types of radiation. While X-rays inflict only limited damage on the strands a hit with heavy ion radiation generates severe cluster damage. This is partially a result of the generation of secondary particles. Due to the fact that heavy ion radiation can be delivered very accurately this effect can be applied to fray the DNA of cancerous cell beyond repair. Source image from `http://www.nasa.gov/centers/marshall/images/content/98984main_1025SR.jpg`

might use the apoptotic pathway to eliminate the potential genetic damage from the larger tissue, or it will most likely die because of damage to its protein synthesis system. If DNA damage is non-lethal for the cell, it may be passed on to the next cell generation which might eventually lead to the onset of cancer (as it is often seen in the form of secondary cancer in irradiation entry channels). Cluster damage to the DNA is most often so severe that it leads to the "immediate" death of the cell (or at least clonogenic death, through the end of mitotic activity).

.

Other impact mechanisms on the cell

Besides the mechanisms for interaction of radiation with the tissue described in the previous sections there are even more ways for the radiation to affect the tissue dynamics. The energy deposited in a tissue by irradiation leads to an increase in the tissues temperature. This effect can be used within a water calorimeter to determine the absorbed dose within experiments. However, this effect does also affect the cells, since on a local scale the in-

crease in temperature can be quite high. Within normal tissue, heating will lead to an increase in blood flow through the tissue in order to cause cooling. The increased blood flow will also deliver oxygen into the affected area. Since the blood supply in avascular tumours is poor, the usage of blood flow to cool down the tissue is limited. This fact can be used within hyperthermia-treatment to slow down the tumour growth. In combination with sophisticated heat-delivery methods, as i.e. tumour-targeting gold-nanoparticles and microwave-heating, this approach can even destroy parts of tumours.

Another secondary effect of radiation is the production of free radicals through water radioloysis. The ionisation of water molecules leads to the creation of for example hydrogen $H\cdot$ and hydroxy $OH\cdot$ free radicals (and many others such as reactive oxygen species (ROS)). These radicals are highly reactive as they attempt to form a covalent bond. That is, they can break an existing bond within another molecule and thus destroy organic components of the cell.

Equation 10 (*Reaction of a free radical*)

$$RH + OH\cdot \rightarrow R\cdot + H_2O \tag{10.2}$$

where R can be an arbitrary organic molecule.

Free radicals are cancerogenetic, but, within the context of radiation treatment, play an important part in the damaging of cancerous cells (see *Dewhirst et al.* (2008) and *Anderson et al.* (2006)).

Lack of tumour oxygenation has long been recognized as a significant factor causing resistance to radiotherapy. This decreased radiosensibility complicates the treatment with conventional radiation. Heavy ion radiation has an greatly increased effect on hypoxic tissues when compared to conventional radiation treatment, as it does not depend on radiolysis to an large extent (*Krämer et al.* (2003)). Its high LET is a possible strategy to overcome hypoxia-induced radioresistance as it is known to be less dependent on tissue pO_2.

Effect on mitochondrial DNA

As it was briefly mentioned in chapter 2, the mitochondria within the cell carry a set of genetic code called mitochondrial DNA (mtDNA) on their own (see *Nass and Nass* (1963)). Irradiation of cells will also affect the mtDNA with the same mechanisms that were described in the previous section.

Even though the vast majority of proteins present in the mitochondria are coded for by the nuclear DNA, this might have effects on the protein production in the mitochondria. Effects on the mitochondria will eventually lead to defects in the cell metabolism. The effect of mtDNA-damage might be even quite pronounced, as it is known that mtDNA is particularly susceptible to oxidative damage, as mediated by free radicals. However, since

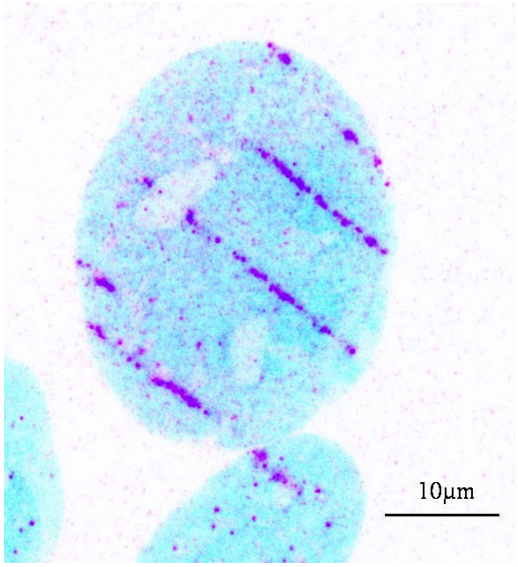

Figure 10.7: Microscopic visualisation of the extremely localised DNA damage induced in nuclei of mammalian cells following irradiation with accelerated ions. Immuno-fluorescence stained repair proteins accumulate at the lesions along the individual ion tracks traversing the nucleus of a human cell, appearing as parallel streaks. DNA counterstain (Propidium Iodide) in blue, repair protein (Mre11) in purple. Source image from `www.gsi.de/forschung/bio/dna_damage_repair.html`

each mitochondrion is estimated to contain up to 10 mtDNA copies (see *Wiesner et al.* (1992)), this effect might depend on multiple hits.

10.3 Beam generation and delivery methods

Production of heavy ion beams

Modern radiation therapy makes use of linear accelerators (linacs) to generate high quality radiation for treatment. A typical linear particle accelerator comprises multiple important parts (see figure 10.8). The source provides the particles for acceleration, which might be electrons (for e.g. from a cathode), protons or ions (from specialised ion sources). The design of the source depends on the particle that is being accelerated. The initial injection is usually done with a high voltage source that shoots the particles into an evacuated cylindrical cavity. Lengths of this tube vary greatly, from about half a meter for x-ray acceleration to several kilometres as primary accelerator for a synchrotron. The cavity contains cylindrical electrodes which get longer from the injection point towards the end of the cavity. The length of each electrode is determined by the frequency and power of the driving power source and the nature of the particle to be accelerated, with shorter segments near the source and longer segments near the target. A source of radio frequency energy is used to energise the cylindrical electrodes. Accelerators of high power use one source for each electrode. Acceleration is achieved through precise switching of the field so that particles are always attracted by the next electrode and repulsed by the last electrode. This requires power, frequency and phase to be exactly regulated. Accelerated particles are either extracted to a target, stored in a ring with the help of magnetic fields, or injected into another accelerator (e.g. a synchrotron).

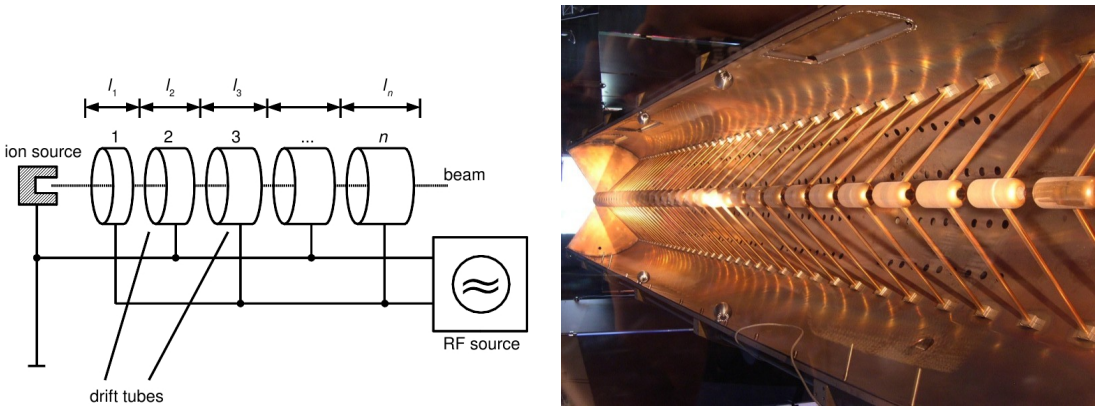

(a) Linac construction principle (b) Section through a linac

Figure 10.8: **(a):** A linear accelerator in principle **(b):** Picture of a cut through a linac. Note the growing size of the drift tubes. Image (a) is in open domain under terms 2, (b) from `http://pfzema.cs.infn.it/pfzema/photos/CERN-03summer/Microcosm/html/Microcosm_-_Linac.html`

Beam application methods

Conventional external beam radiotherapy (2DXRT)

The most basic delivery method is the 2DXRT method, in which the radiation beam from a linac is delivered to the patient from several directions. Radiation planning is done on a x-ray based simulator. 2DXRT is cheap and reliable, but not applicable in most sensitive treatment areas. As an outdated treatment method, 2DXRT is being increasingly replaced by 3DCRT.

3-dimensional conformal radiotherapy (3DCRT)

Through the availability of new imaging methods, such as CT and MRI, treatment planing was greatly improved, as the tumour can now be delimited precisely from the surrounding healthy tissue.

An enhancement of virtual simulation is called 3-Dimensional Conformal Radiotherapy (3DCRT), in which the profile of each radiation beam is shaped to fit the profile of the target from a beam's eye view (BEV), using a multi-leaf collimator (MLC) and a variable number of beams. As a result of the treatment volume conforming to the shape of the tumour, the relative toxicity of radiation to the surrounding normal tissues is reduced, allowing a higher dose of radiation to be delivered to the tumour in comparison with conventional techniques.

A typical MLC consists of 2 sets of 20-40 leaves, each around 5 mm thick and several cm in the other two dimensions. Newer MLCs now have up to 120 leaves. Each leaf in the MLC is aligned parallel to the radiation field and can be moved independently to block part of the field. This allows the dosimetrist to match the radiation field to the shape of the tumour, thus minimising the amount of healthy tissue being exposed to radiation. On

a machine without an MLC this must be accomplished using several hand-crafted blocks.

Using a MLC to shape the beam, however, imposes serious disadvantages on the beam quality due to fragmentation and diffraction of the beam. Furthermore, beam losses and contamination by nuclear fragmentation in passive beam shaping elements in front of the patient are likely.

Intensity-modulated radiotherapy (IMRT)

The next step in beam delivery is the IMRT, an advancement of 3DCRT. IMRT also improves the ability to conform the treatment volume to concave tumour shapes, for example when the tumour is wrapped around a vulnerable structure, such as the spinal cord or a major organ or blood vessel.

Computer-controlled x-ray accelerators distribute precise radiation doses to malignant tumours or specific areas within the tumour. The pattern of radiation delivery is determined using highly-tailored computer applications to perform optimisation and treatment simulation (Treatment Planning). The radiation dose is made consistent with the 3-D shape of the tumour by modulating the radiation beam's intensity. In some systems this intensity modulation is achieved by moving the leaves in the MLC during the course of treatment, thereby delivering a radiation field with a non-uniform, modulated intensity. IMRT is especially useful when treating tumours near complicated body sites such as CNS, head and neck, prostate, breast and lung. Unfortunately, IMRT is limited by its need of additional time from experienced medical personnel in order to design an individual treatment plan.

Image-guided radiation therapy (IGRT) / 4DXRT

IGRT augments radiotherapy with imaging in order to increase the accuracy and precision of target localisation, thereby reducing the amount of healthy tissue in the treatment field. Real-time imaging is combined with real-time adjustment of the therapeutic beams. This new technology is called image-guided radiation therapy (IGRT) or four-dimensional radiotherapy.

IGRT makes use of a fully-active intensity-controlled beam delivery system, in which the particle beam is scanned across the target volume by horizontal and vertical scanning magnets. This is done in multiple slices, in order to irradiate a target volume exactly equal to the tumour. The underlying principle is analogue to the generation of an image on a TV screen by the scanning of an electron beam. Penetration depths for the slices can be regulated through the synchrotron control system, which provides a pre-defined set of beam energies corresponding to different positions of the Bragg peak. Beam intensity and focussing may be changed from pulse to pulse by the therapy control system.

The treatment is done in a 3D irradiation matrix, which typically consists of about 20.000 raster points. In order to ensure that each voxel receives exactly the planned dose, the scanning system has to be intensity-controlled and needs a feedback from a fast beam monitor. This has the clear advantage that any prescribed 3-dimensional dose distribution can in principle be generated. Therefore, also tumours near critical structures

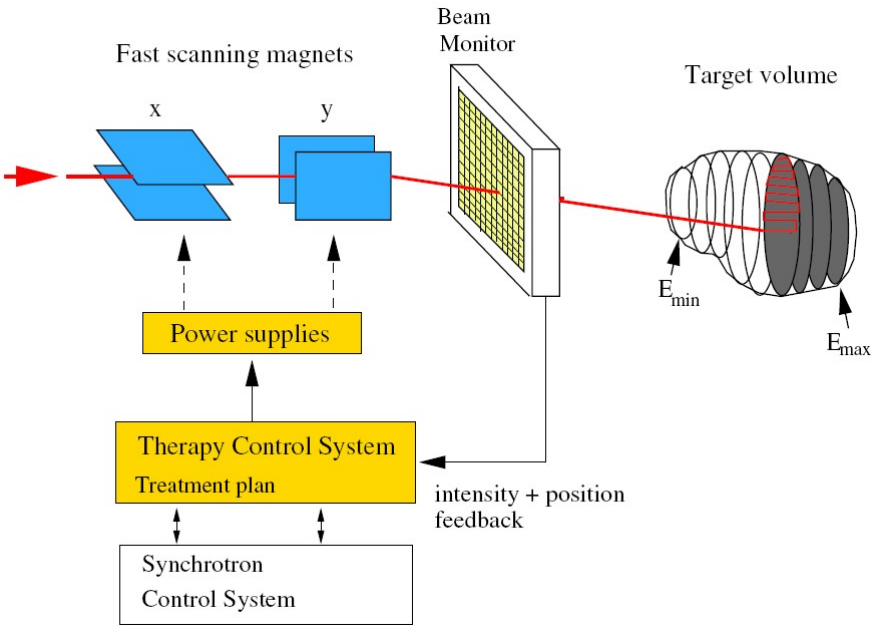

Figure 10.9: Principle of the magnetic scanning system at GSI. The target volume is irradiated by moving the ion beam (80-430 MeV/u 12C) with fast magnets over each slice. The required beam energies - corresponding to the depth of the Bragg peak for each slice - are supplied on a pulse-to-pulse operation by the synchrotron (SIS) control system. From *Schardt and The Heavy-Ion Therapy Collaboration* (2007).

like the brain stem and optical nerves can be treated with maximum efficiency. With the present system the dose can be deposited with millimetre precision, but this implies that it must be possible to immobilise the patient with about the same precision.

The irradiation of moving targets (such as the lung) demands new strategies, like for example the development of a real-time motion-compensating system.

PET-techniques for in-situ range verification

Another plus of the carbon ions is the small amount of nuclear fragmentation of the projectile ion. This is frequently seen as a drawback compared to proton irradiation, because it produces a small tail of dose beyond the Bragg maximum consisting of protons and other light ions, as shown in the previous section.

However, through the production of positron-emitting carbon isotopes 10C and 11C, it becomes possible to measure the actual beam position by the coincident registration of the annihilation quanta. As the isotope undergoes positron-emission decay it emits a positron, which, after travelling up to a few millimetres, encounters and annihilates with an electron. This produces a pair of annihilation photons of discrete energy moving in opposite directions. Coincident recording of the annihilation radiation in two opposite detector heads and applying tomographic reconstruction algorithms opens up the possibility to calculate their origin (see figure 10.10 for a sketch of the method).

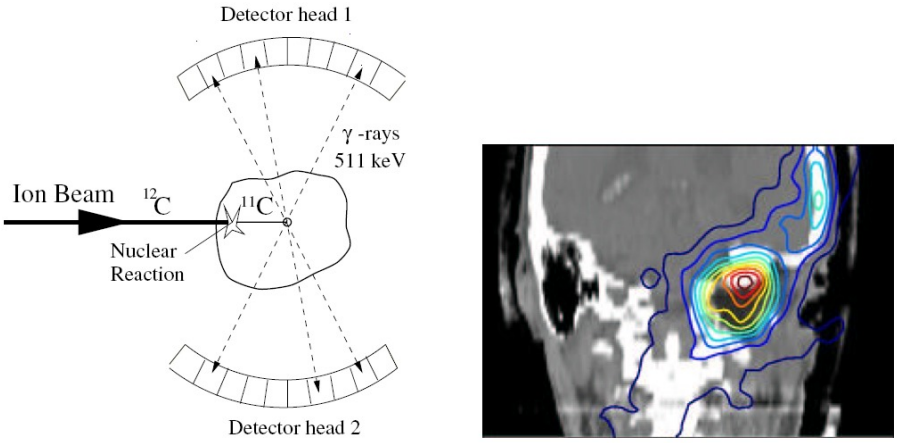

Figure 10.10: `Left:` Principle of the in-situ range verification by PET techniques. `Right:` Superposition of a measured β+-activity distribution (contour lines) and the corresponding frontal slice of patient CT data. The carbon beam entered from top right, the PET-detector heads were located vertically above and below the patient table. From *Schardt and The Heavy-Ion Therapy Collaboration* (2007).

According to this PET-data it is possible to adjust the beam position in real-time, in order to correct deviations from the planed target position. This confers an advantage to carbon ion irradiation comparable to actually seeing a target while shooting at it instead of firing blindly. A comprehensive overview of the positron-emission in heavy ion-treatment can be found in *Pshenichnov et al.* (2006) and *Pshenichnov et al.* (2007).

Clinical results

Since December 1997 more than 300 patients were treated at the GSI, Darmstadt, most of them within clinical phase I/II trials. Standard treatment procedure encompased a fractionated carbon ion irradiation in 20 consecutive days with a median total dose of 60 Gy, which was well tolerated without severe side effects. Three-year local control rates of 81% for chordomas, 100% for chondrosarcomas and 62% for adenoid cystic carcinomas were reported (for detailed statistics see *Schulz-Ertner* (2004)).

Especially treatment of inoperable tumours in the skull-base region was of high success (see *Schulz-Ertner* (2007) and figure 10.11 for an example for tumour regression after carbon ion treatment).

Due to the overall positive clinical results obtained in the GSI pilot project, a dedicated hospital-based ion treatment facility is under construction in Heidelberg, Germany. The facility will have a planned capacity of 1000 patients per year. The accelerator will consist of a rf-linac and a synchrotron, providing beams of protons, helium-, carbon- and oxygen-ions.

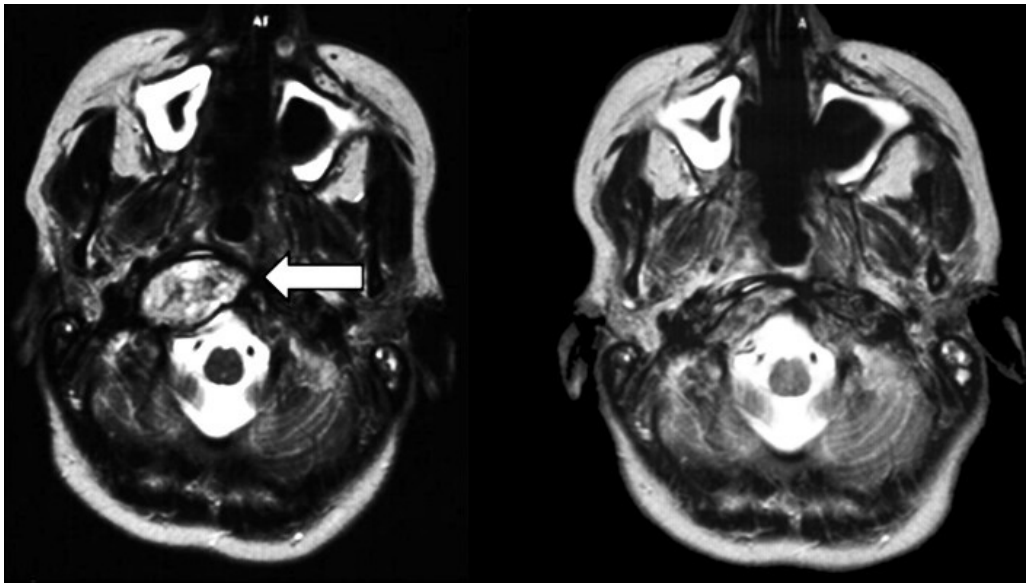

Figure 10.11: Regression of a chordoma. Left: before treatment. Right: 6 weeks after carbon ion radiotherapy. Source picture from *Schardt and The Heavy-Ion Therapy Collaboration* (2007).

10.4 Mechanism of irradiation simulation

A variety of models for the complex effects of radiation therapy on tissue exists (see e.g *Dionysiou et al.* (2004), *Ribba et al.* (2006) and *Zhang et al.* (2007)). However, these models are often limited, in a sense that they are specialised to suit a specific treatment situation. Most of them rely on an abstract implementation of processes which can be modeled for themselves (such as mitosis or necrosis). Although these models can be used to investigate certain parts of the irradiation process, most of them are lacking spatial resolution and cannot integrate experimental parameters, as it is possible in a force-based model.

The basis for an realistic model of irradiation simulation will be a detailed dose deposition profile from an advanced simulation environment for particle interaction such as GEANT4. It is possible to calculate the deposited dose for a distinct position e.g. every cell's nucleus within this approach. Furthermore, even the type of radiation acting on a cell can be determined in the simulation, and therefore the activation of very distinct and realistic mechanisms becomes posible.

However, to develop this model of extremely complex processes, which are at the base of a tumour's reaction to irradiation, is beyond the scope of this thesis. It is the target of continued work within the CARADI project mentioned in section . However, to demonstrate the principal feasibility to model these effects within an agent-based approach, a simplified system of irradiation was implemented and tested within this thesis.

Neglecting the details of the multitude of available mechanisms for the impact of radiation on a cell leads to an effective summation of these mechanism's effects (as depicted in figure 10.12). These effects include:

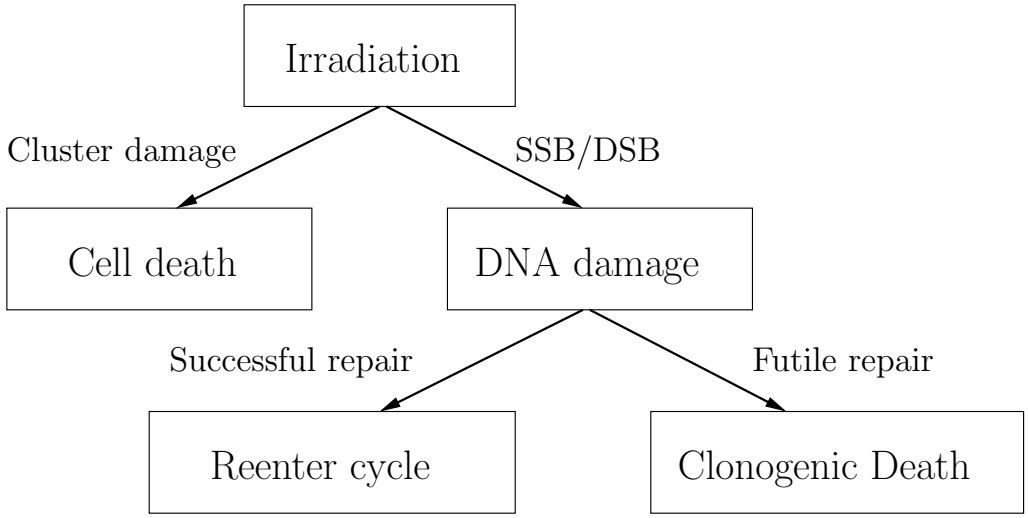

Figure 10.12: Sketch of the implemented mechanism for tumour irradiation. A defined tumour volume can be treated with the `irradiate`-function. Each cell within the volume is affected in a way that either results in interphasic death (i.e. through cluster damage), or simple DNA damage (single strand breaks or double strand breaks) with a defined probability. DNA damage may be repaired re-entering the cell into the cycle or, after a distinct threshold of futile repair tries, the cell undergoes clonogenic death through senescence in G_0.

- interphasic death: cells are sent into necrosis straight away due to severe damage
- DNA damage: cells not dying of interphasic death are marked as DNA-damaged and cannot pass the G_2 checkpoint until repair
  - at G_2-checkpoint cells are marked as repaired with a distinct probability
  - otherwise the repair-trial count is increased
  - upon a too high trial-count cells are sent into senescence (clonogenic death; permanent G_0)
- mitotic death: cells can only undergo a distinct number of further mitotic events before being sent into senescence
- accelerated differentiation: cells go into terminal differentiation (clonogenic death)

Irradiation in this simplified application is handled in the following way by the `irradiate` function. A treatment centre and radius is passed to the `irradiate`-function which then brings cells which lie within this volume into necrosis with a predefined probability (interphasic death). Possible modifications and extensions include necrosis-probability dependency upon the distance to the irradiation centre or on the RBE of the used radiation. Alternatively, the whole tumour may be treated. Cells which are not sent into direct necrosis are marked as DNA-damaged. This prohibits cells from passing the G_2/M checkpoint until the damage is repaired. Again this is handled via a stochastic process, giving the cell a repair chance within distinct timesteps. If this chance is missed multiple times, the cell is finally sent into senescence (clonogenic death). Mitotic death and accelerated

differentiation are not accounted for in the model directly. Cells may have a probability of being unaffected by the irradiation.

An improved approach would be to model the deposited radiation type and energy with the GEANT4 toolkit, according to the current tumour morphology (see *Pshenichnov et al.* (2005)). As a result of the calculated dose deposition, necrosis probabilities or other effects (such as arrest of the cell in G_2 due to severe DNA damage) could be calculated.

10.5 Results of modelling

Cell cycle arrest in G2 after irradiation

Upon irradiation cells are likely to acquire severe DNA damage as described in section 10.2. Since cells possess multiple mechanisms which are used to assure the fidelity of the DNA passed on to offsprings, this DNA damage can have severe effects on a cell's cycle progression. A prominent effect of this is mediated by the G_2/M-checkpoint as introduced in section 5.1. Thus, upon the detection of damage, the cell cycle is arrested via inactivation of the Cdc25 phosphatase, in order to prevent transmission of damage to daughter cells. Repair mechanisms are activated, but as they are working the progress of the cell from G_2-phase to M-phase is prohibited. This leads to an accumulation of cells in G_2 phase. This effect can be quantified with the help of cell cycle analysis tools (as done in *Bohl* (2006)). As described in section 5, cells double their DNA content during S-phase while keeping the DNA's ploidy constant. This leads to the fact that cells in $G2$- and M-phase have about the double amount of DNA content compared to cells in G_0 or G_1. DNA content of cells in the process of DNA duplication during S-phase lies between these values. Experimental results of this pheonomenon are shown in figures 10.13(a) and 10.13(b). Within the experiments, glioblastoma cells cultured in vitro were exposed to 8 Gy irradiation and a DNA content analysis was performed 12 hours later for an irradiation sample and a control sample. The cell phase distribution changed drastically in response to the radiation treatment. Progression of damaged cells from the G_2 to the M phase was limited, therefore a shift in the cell phase distribution was observed. In normal cell colonies the relative amount of cells within a phase resembles its relative length according to the overall cell cycle. As observed in figure 10.13(a) the majority of cells are in G_0 or G_1 phase and accordingly have single DNA content. Only about 20% of cells reside in the G_2 or M phase. After irradiation this distribution was shifted to about 62% of the cells residing in G_2 or M phase.

This process of G_2-arrest is also found within the simulation of tumour irradiation. Cells damaged by irradiation cannot pass the G_2/M-checkpoint until repairs of their DNA were successful according to the minimal irradiation model (see figure 10.12). Although the DNA content of the cell is not quantitised within the cell implementation, statistics comparable to the experimentally obtained results are available through the discrete cell cycle phases of the cell agents. Upon irradiation of the full tumour volume, cells were

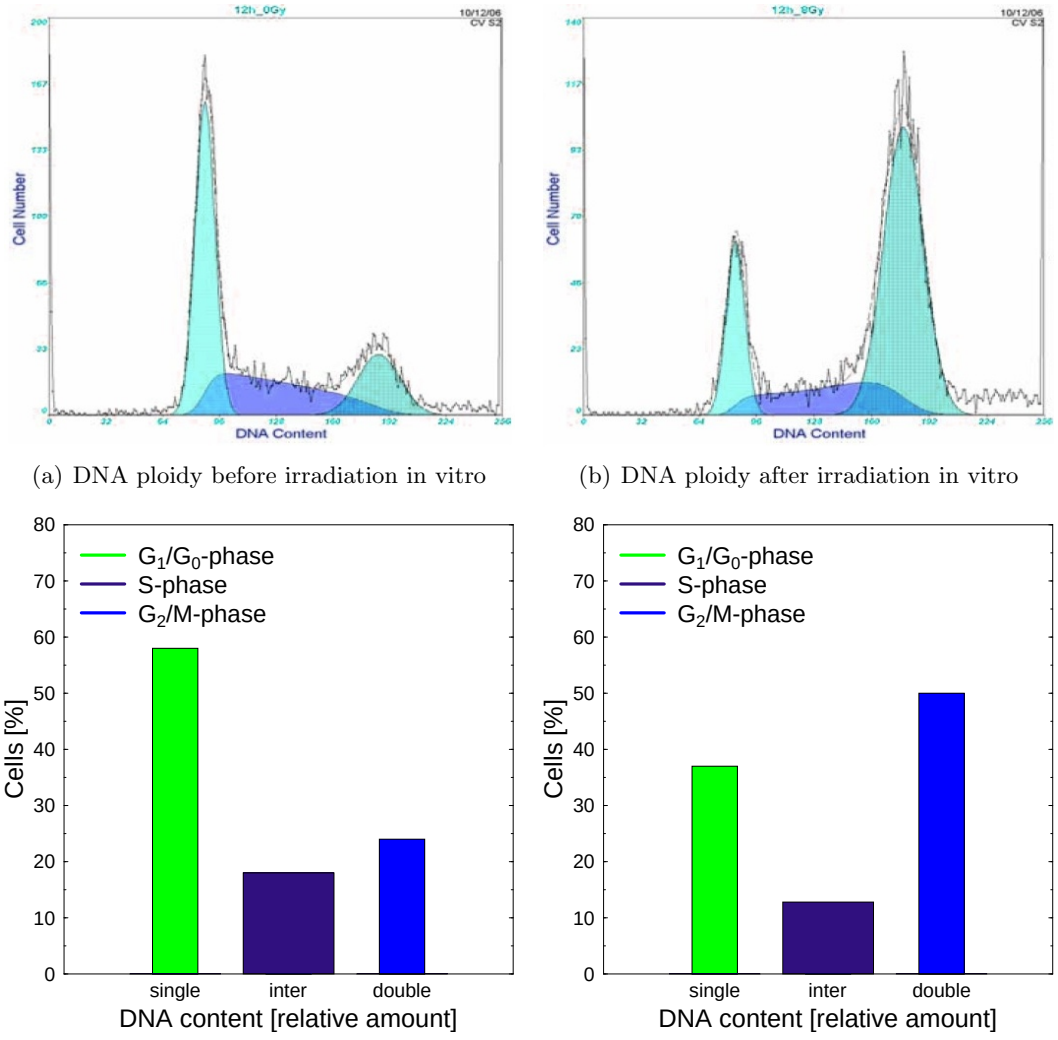

(a) DNA ploidy before irradiation in vitro

(b) DNA ploidy after irradiation in vitro

(c) DNA ploidy before irradiation in silico

(d) DNA ploidy after irradiation in silico

Figure 10.13: **(a+b):** Cell cycle arrest at the G_2/M-checkpoint due to DNA damage after heavy ion irradiation, from *Bohl* (2006). Cells were irradiated with a dose of 8 Gy and cell cycle analysis performed for an irradiated and a control sample after 12 hours. Amount of cells in G_2/M rises from 20% to 62% after irradiation. **(c+d):** Simulation results of cell cycle distribution without and with irradiation of cells. The minimum irradiation model as described in section 10.4 was used. Cells show a shift of the cell cycle distribution after 12 hours as in the experimental results (a+b).

either sent into necrosis (interphasic death) with a probability of 33%, damaged with a probability of 62% or remained unaffected with a probability of 5%. Damaged cells were allowed 5 repair tries at the G_2/M checkpoint, each possibly successful with a probability of $p_{rep} = 20\%$. Upon an unsuccessful repair try cells were prohibited for the length of the G_2 phase τ_{G_2} to try again. Cells not repaired after 5 tries were sent into senescence (clonogenic death) with an corresponding probability of $(1 - p_{rep})^5 \approx 33\%$.

The according results from the simulation are shown in figure 10.13(c) and 10.13(d). A shift in the relative amount of cells residing in G_2 or M from 24% to 50% is visible 12 hours after irradiation. This result corresponds to the experimental data. This agreement suggests that it is, in general, feasible to implement radiation damage mechanisms within an approach similar to the minimal model. Derivation of realistic probabilities for this model from experiments which are dealing with cell cycle responses to irradiation (such as *Hanin et al.* (2006)) will be the next step towards an realistic irradiation model.

Total tumour irradiation

Irradiation of the total volume is comparable to a treatment with image-guided radiation therapy scanning-techniques. Every cell inside the tumour spheroid will be affected with a given probability according to the mechanisms discussed in section 10.4. According to the chosen probabilities cells will be sent into necrosis or marked as DNA-damaged, prohibiting the passage of the $G2/M$-checkpoint.

Effects of treatment are best visualised within a tumour mass curve over time as depicted in figure 10.14. Determining parameters for the irradiation are the probabilities p_{nec} and p_{dna}. For the run in figure 10.14 these were set to $p_{nec} = 33\%$, $p_{dna} = 62\%$ leaving a 5% chance for cells to remain completely unaffected by the treatment. As seen in the simulation, this choice of probabilities is not suited to result in a reduction of tumour mass. Even if the tumour growth is stalled immediately after irradiation, it resumes as soon as the effects of the G_2-arrest are overcome. Cells have a repair probability of $p_{rep} = 20\%$ at the G_2/M-checkpoint if marked as damaged according to the mechanisms described in section 10.5.

An actual regression of tumour mass can be achieved if the parameters for the minimal irradiation model are changed. A higher probability for interphasic death $p_{nec} = 65\%$ is to be used. Accordingly, the probability for DNA damage must be decreased to $p_{dna} = 35\%$ leaving no cell unaffected by the treatment. Additionally, the repair probability can be decreased to $p_{rep} = 10\%$, resulting in an overall probability of cell death by DNA damage of $(1 - p_{rep})^5 \approx 0.60\%$, or even to $p_{rep} = 5\%$ (yielding an overall probability of cell death by DNA damage of $(1 - p_{rep})^5 \approx 0.77\%$).

Further mechanisms governing the dynamics of tumour spheroids under irradiation will be studied within a partial irradiation model.

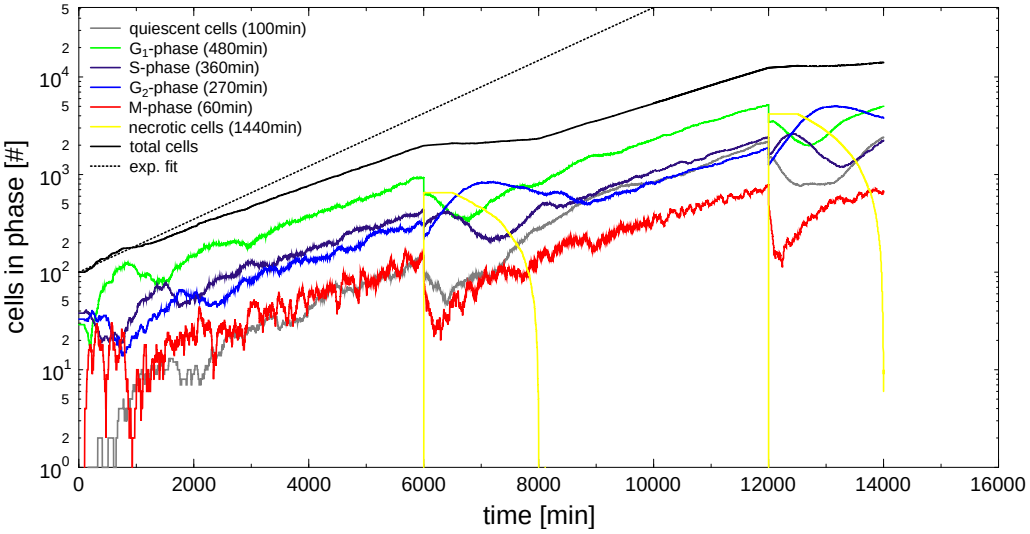

Figure 10.14: Cell phase distribution in response to irradiation of the total tumour volume. Depending on the probabilities used in the minimal irradiation model (see section 10.4) growth stagnation of the tumour after irradiation can be observed. Cell cycle arrest at the G_2/M-checkpoint is visible with a peak approx. 9 hours after irradiation.

Partial tumour irradiation

The general idea of modelling the partial irradiation of tumours is to study the dynamic effects which rise in the tumour system upon elimination of a population part.
The results of partial tumour irradiation are obtained using the minimum irradiation model, as described in section 10.4. However, emphasis was put on interphasic death through severe cluster damage, not on the mechanisms resulting from SSBs or DSBs.

Starting point of the irradiation simulation is a dynamic tumour spheroid which developed from a single malignant cell. Simulation can also be performed on predefined tumour spheroids, skipping the initial growth phase, as the tumour configuration can be saved in any intermediate step. Realisation of clinical tumour cases is in principle posible on a basis of imaging techniques providing details of the tumour composition. This, however, assumes that suitable coarse graining mechanism are available to handle the extreme high number of cells.

A sample run illustrating the dynamics of the tumour system is shown in figures 10.17 and 10.18. Results shown within this section are exemplary, more data is available upon request. The absolute and relative cell phase distributions for this run are given in figures 10.16 and 10.15.

Irradiation of tumour spheroids leads to a temporary increase in the amount of actively dividing cells, visible in figure 10.15. Since the majority of the spheroid is comprised of cells in quiescence, irradiation of a larger volume has a severe impact particularly on the cells in G_0 (compare figures 10.17(a) and 10.17(b)). However, as the quiescent cells were not contributing to the tumour growth, eradication of a large number of them does not have a distinctive impact on the tumour size (see figure 10.16). Instead, the sudden

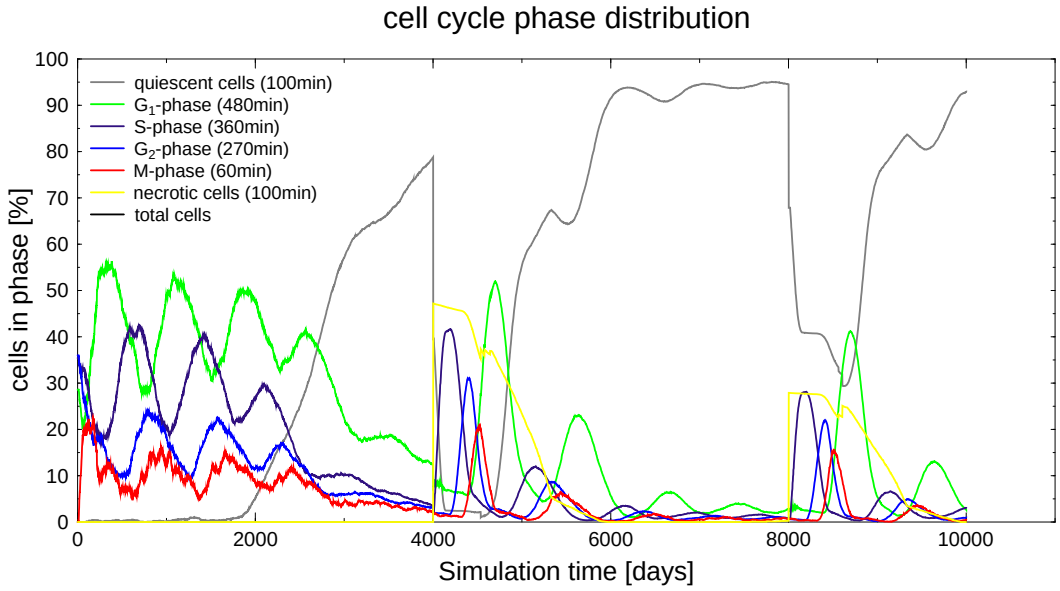

Figure 10.15: Cell cycle distribution of a tumour spheroid under partial irradiation. Notice the sudden rise of actively proliferating cells (in interphase) upon irradiation at 4000 and 8000 minutes. This is due to the fact that irradiation kills mostly quiescent cells and leads to a sudden rise in nutrient availability for the remaining cells. Simulation started with 500 malignant cells - spheroid comprises 14.000 cells at the end of simulation.

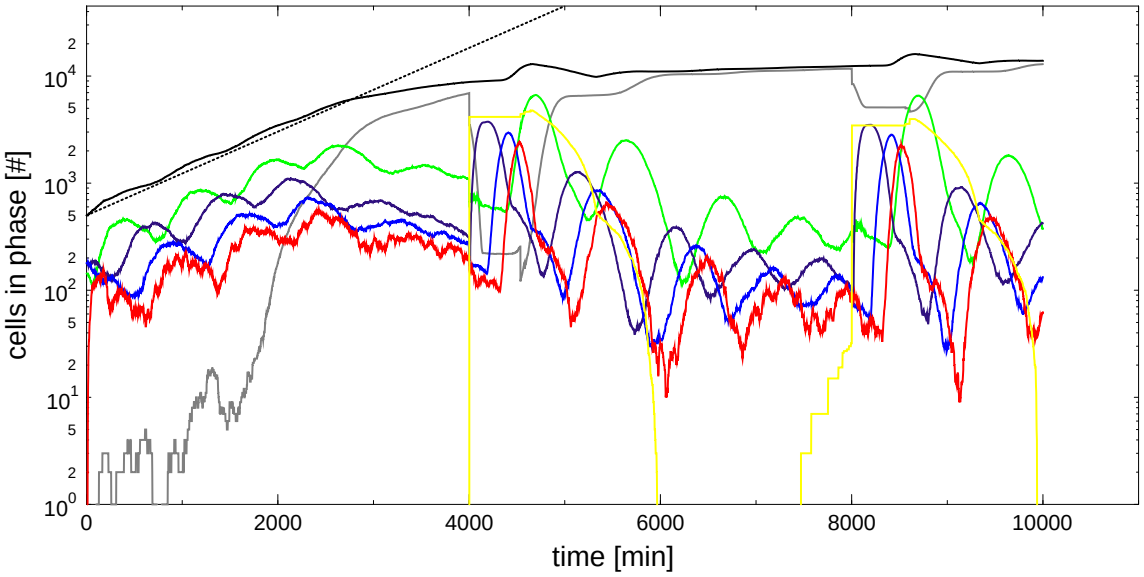

Figure 10.16: Cell cycle distribution of a tumour spheroid under partial irradiation. Notice the sudden rise of actively proliferating cells (synchronised in interphase) upon irradiation at 4000 and 8000 minutes. This is due to the fact that irradiation kills mostly quiescent cells and leads to a sudden rise in nutrient availability for the remaining cells. Note also the excessive regrowth of the tumour in response to irradiation that leads to necrosis of quiescent cells (visible within the bumps in the according curves of necrotic and quiescent cells at the end of the "irradiation plateau"). Simulation started with 500 malignant cells - spheroid comprises 14.000 cells at the end of simulation.

necrosis of cells leads to an increase in the availability of nutrients and to a decrease in the overall pressure inside the tumour. This yields a rise in the number of cells in the interphase, since a large number of cells are now able to pass the restriction point.

Figuratively speaking this is due to the fact that, through partial irradiation, the tumour surface is effectively increased so that it can support a larger number of actively dividing cells in the surface layer. In addition, the nutrient consumption is decreased due to necrosis of irradiated cells, which leads to an overall rise in nutrient availability. A possible channeling of nutrient diffusion through the spongy tissue cannot be observed within the simulation due to limited resolution of the diffusion grid. Therefore, modelling a small test system with superior resolution of the diffusion grid is of interest for further investigations.

The re-entry of large amounts of previously quiescent cells into the cell cycle leads to regrowth of the tumour volume (see figure 10.17(c)). As a result, reformation of a quiescent core due to rising cell pressure is seen. Furthermore, nutrients are even depleted inside the tumour core, what leads to the rise of necrosis in the tumour centre (visible in figure 10.17(d)). As necrotic cells are shrinked and removed from the simulation, the tumour reaches a state where only few cells are undergoing necrosis in the centre as it grows on the surface (see figure 10.18(a)). Upon repeated irradiation the effect of pressure-reduction is responsible for the re-entry of a major part of quiescent cells into the cell cycle. The reduced pressure is visible within figure 10.18(b), with cells bleached out according to their to their pressure (low pressure cells bleached). The second irradiation is applied to the same position and, therefore, affects less cells due to the new tumour shape in response to the prior irradiation. Rising pressure through the rise in mitotic activity eventually leads to necrose in the tumour core, as observed in figures 10.18(c) and 10.18(d), as it was seen in the first irradiation.

Throughout the corresponding growth curves (figures 10.15 and 10.16) a fast relapse after irradiation is visible. Even though a significant amount of cells suffers interphasic death, necrosis removal and re-growth of the tumour are balanced to keep the overall size constant (counting necrotic, but not removed cells, as part of the total cell number).

Partial irradiation is not sufficient to reduce the tumour spheroid in size. It even leads to an excessive growth of the tumour above the threshold that is supported within the shell of viable nutrient and pressure conditions. This relapse leads to the induction of necrosis within the population of still quiescent cells. This effect is visible in figures 10.15 and 10.16 as a small bump in the amount of necrotic cells at the end of the "irradiation-plateau" and the corresponding defect in the curve depicting the amount of quiescent cells (or in the corresponding visualisation in figures 10.18(b) and 10.18(c) through the rise of a distinct necrotic core). Another example of this re-entry effect is depicted in figure 10.19. The relapse effects should be more pronounced with rising tumour size as the number of quiescent cells rises drastically.

Another effect of partial irradiation is the resynchronisation of cell cycle progression. This happens due to the passage of foremost quiesent cells at the restricition point upon irradiation. Entry from G_0 into S happens within a short timespan of τ_{G0} which corre-

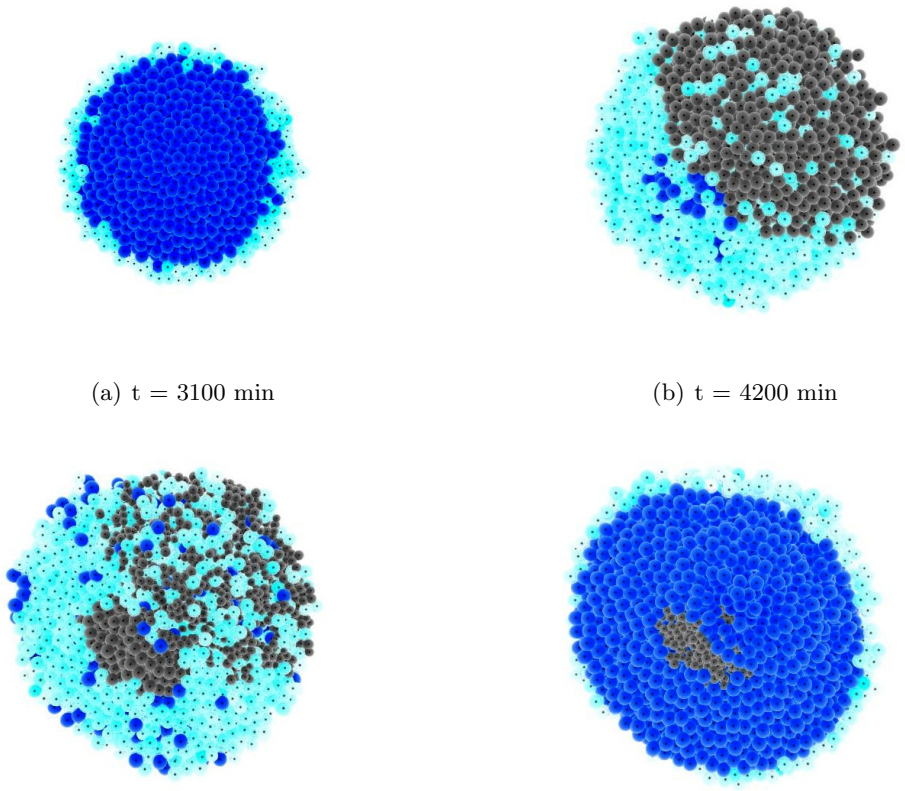

(a) t = 3100 min

(b) t = 4200 min

(c) t = 4800 min

(d) t = 5400 min

Figure 10.17: Visualisation of partial tumour irradiation. Relative and absolute cell phase distributions for this run are given in figures 10.15 and 10.16. Figure **(a)** shows the tumour spheroid with a developed quiescent core due to pressure inhibition. Upon irradiation this pressure decreases immediately (see figure **(b)**), what reduces the level of quiescent cells significantly. Formation of a small necrotic core due to a shortage of nutrients is visible in **(c)**. Pressure inside the spheroid is rising again fast due to the growth of cells re-entered into the cycle. This leads to a reformation of the quiescent layer in **(d)**. Colour code: quiescent cells in blue, viable cells in turquoise, necrotic cells in grey. Cells under low pressure bleached out.

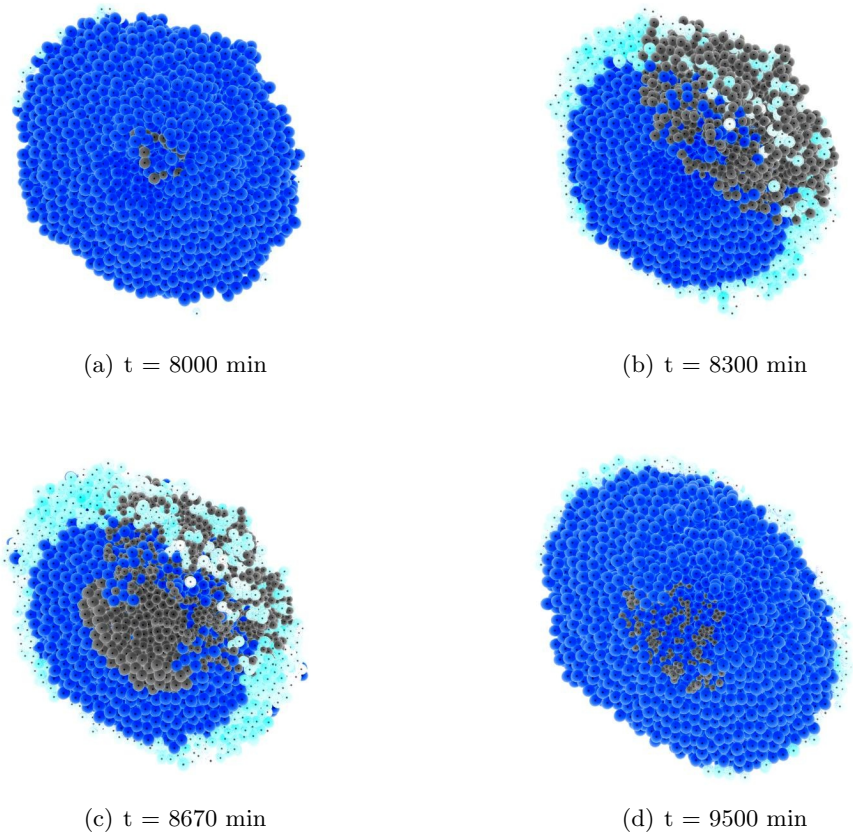

(a) t = 8000 min

(b) t = 8300 min

(c) t = 8670 min

(d) t = 9500 min

Figure 10.18: Visualisation of partial tumour irradiation continued from figure 10.17. Relative and absolute cell phase distributions for this run are given in figures 10.15 and 10.16. Tumour spheroid prior to second irradiation shown in **(a)**. Small necrotic core and quiescent layer visible, boundary layer of viable cells is partially bleached out in the visualisation according to their reduced pressure (see figures 10.16 for the total number of viable cells). Irradiation in **(b)** leads to a decrease in pressure and an increase in nutrient concentration, followed by an re-entry of quiescent cells into the cycle. Shrinkage and removal of necrotic cells lead to a further decrease in pressure on the irradiation site in **(c)** (visible through the bleaching of cells). Necrotic core is forming again due to shortage of nutrients. A rise in pressure due to cell growth and mitosis leads to the final, largely quiescent, configuration shown in **(d)**. Colour code: quiescent cells in blue, viable cells in turquoise, necrotic cells in grey. Cells under low pressure bleached out.

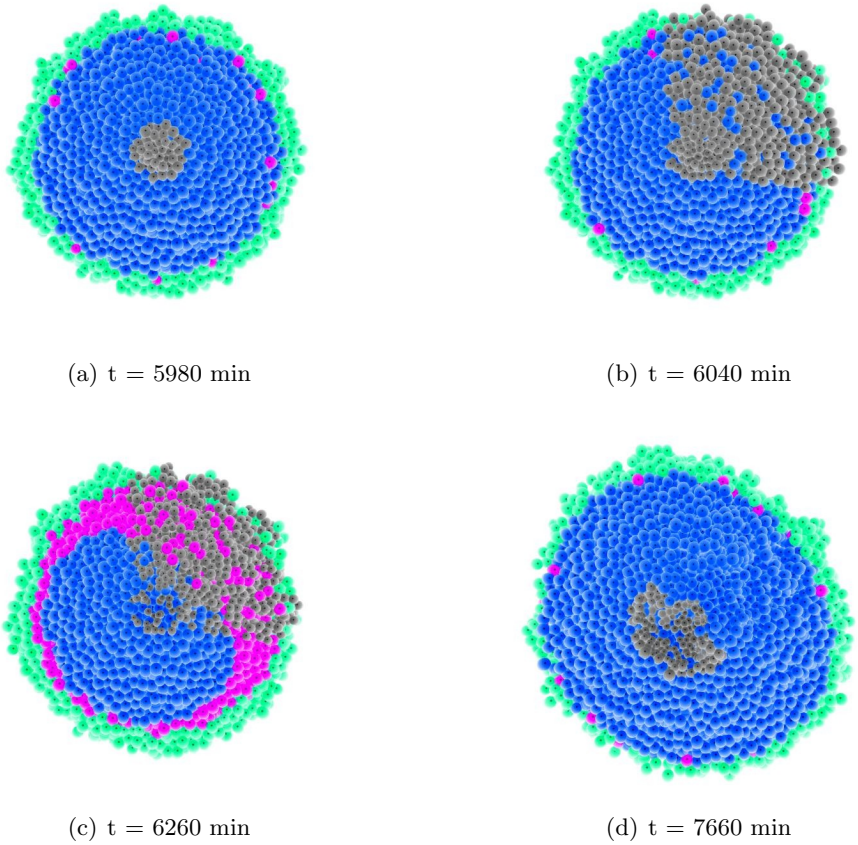

(a) t = 5980 min

(b) t = 6040 min

(c) t = 6260 min

(d) t = 7660 min

Figure 10.19: Visualisation of cell re-entry after partial tumour irradiation. A section of a fully developed tumour spheroid shown in **(a)** is irradiated at 6000 minutes runtime in figure **(b)**. Interphasic death of cells in the irradiation volume leads to fast re-entry of cell on the outer layer of quiescence, especially in the region of irradiation (as shown in **(c)**). Fast regrowth of the tumour leads to re-entry of the cells into quiescence and to the development of a necrotic core due to nutrient depletion in the centre (visible in **(d)**). Colour code: quiescent cells in blue, viable cells in turquoise, necrotic cells in grey, cells re-entered from quiescence in red.

sponds to the responsiveness of quiescent cells to the newly rising suitable environmental conditions. The degree of resynchronisation observed therefore depends directly on τ_{G0} and is of interest for further investigation.

11 Discussion and outlook

11.1 Goals achieved and significance of the results

Within this thesis multiple goals were achieved during the process of obtaining the final simulation application. These comprise:

Abstraction of relevant cell characteristics The relevant properties for the modelling of cells within the scope of this thesis were successfully abstracted, both into basic mathematical models and into an agent-based class. The chosen implementation is highly flexible and can be extended to include every cell attribute of interest in further investigations.

Realistic cell interactions Contact models such as the JKR-model were used to capture the cell interactions, including differential cell-cell adhesion. The interaction model was able to reproduce cell sorting as it is observed in experiments.

Cell cycle regulation and metabolism An extendable model of the cell cycle and its regulation was implemented, together with the handling of cell nutrients in a reaction-diffusion system.

Implementation of realistic cell dynamics The forces resulting from the contact interaction were integrated using adaptive stepsize algorithms allowing the simulation of bigger cell systems in a reasonable amount of time.

Adaptive stepsize algorithms Global and local criteria were developed to ensure system integration within given accuracy which at the same time yield a significant improvement in simulation runtime.

Development of advanced cytokinesis algorithm A sophisticated method for the handling of cytokinesis was developed, which is able to model the process of cytokinesis close to its dynamics in vivo. Artificial velocities rising in regions of high mitotic activity were thus diminished, further improving the simulation performance.

Simulation of tumour growth Spatio-temporal dynamics of tumour spheroids were modelled, yielding the commonly accepted layered morphology of MCTS. Tumour Growth curves in correspondence to experimental results could be obtained with the final application. Through comparison of different simulation models to the experimental data it was possible to draw conclusions about their level of correspondence to

the modelled cell properties. A comparison between nutrient- and pressure-based mechanism for contact inhibition could be performed.

Simulation of tumour irradiation First results were obtained and compared to experimental visible effects (cell cycle arrest). Multiple effects in the tumour dynamics were observed which were caused by irradiation and are of interest for further modelling (resynchronisation, excessive growth).

Qualitative correspondence to experimental results was obtained, however further improvements to the model are eligible in order to capture the growth behaviour of larger cell systems.

Overall the model could benefit from a better combination of its implemented mechanisms for cell cycle regulation in response to environmental parameters (such as nutrient concentration or cell pressure). The question, wheter quiescence is primarily induced by contact inhibition or nutrient scarceness, should be investigated in experiments. The experementally observed reactions of cells could be used in order to gauge the cell agents' response within the model. In general, improvements could be achieved through extraction and itegration of more parameters from experiments. This cooperation could lead to a synergy effect from which theory and experiment could benefit likewise.

Another mechanism that needs further investigation is the modelling of cell starvation. This, however, suffers from the lack of cell nutrient uptake rates discussed in the literature. Consumption rates are usually averaged over large cell populations, which differ in their phase distribution, resulting in a limited usability within an agent-based implementation. A simple experimental approach would be, to halt a cell population in distinct phases of the cycle, e.g. through the inhibition of the corresponding cyclin dynamics, and then measure the nutrient consumption rates associated with the according cycle phase.

Some model mechanisms which are already implemented within this thesis need an extension, including more details of the process. This is especially the case for the minimal irradiation model, that can just be considered a demonstration of feasibility and has to be extended to capture the full scale of cell reactions to radiation with respect to extern parameters (such as nutrient concentration, hypoxia). Implementation of genetic networks for the cell agents could also benefit the simulation through availability of new interaction mechanisms, particularly for the effects of radiation on the cell.

A question which needs further attention is the handling of necrotic and apoptotic cells. It is not clear if their removal from the simulation represents a good approximation of the in vivo process. Removal eventually leads to the re-filling of parts of the tumour core through an inwards drift of the surrounding cells. Even though this intermixing is observed in other models, the process is in contradiction to the experimental finding that tumours have a hollow core under high pressure. Further investigation of the process is necessary to develop a more realistic model.

Although adaptive stepsize algorithms yield an immense performance increase, the simulation is still limited to low cell numbers compared to sizes of many tumours found in

vivo. This deficiency has to be overruled by the development of efficient coarse graining mechanisms, enabling systems greater than $\mathcal{O}(6)$ cells to be modelled.

The model is of great applicability when cellular processes like mitosis and phase synchronisation are of importance, since effects of mitosis, necrosis and apoptosis can be modelled in detail within the agent-based approach. This distinguishes the model from a great many of alternative models for tissue dynamics. Spatial resolution benefits the modelling process and extension to a combined modelling of the sub-cellular level could even extend this advantage. Therefore, a further suitable field for application of the system is the modelling of processes which happen on a small scale, such as the effects of mitosis on cell systems or even the process of mitosis itself. Within the field of small systems the agent-based approach is unparalleled in respect to its applicability. Inclusion of intracellular dynamics or even usage of an deformable model for the cell would be possible within these smaller systems.

Application of the model to a fixed cell type (e.g. glioblastoma cells) could include unique mechanisms and parameters in the process of tailoring the code to the cells under consideration. However, generalisability of the code is an advantage that should not be easily abandoned, as it opens up the possiblity to model quite different systems with the application.

11.2 Further mechanisms

The developed application can be extended with various mechanisms that would lead to a more realistic model of tumour dynamics. A first approach would be the inclusion of pressure repulsion, depending on the cell pressure defined in equation 7.7. Pressure between interacting cells can be compared, yielding a repulsion force in the direction of the pressure gradient:

Equation 11 (*Pressure force*)

$$\boldsymbol{F}_{ij}^{pres} = f_{pres}(p_i - p_j)\boldsymbol{e}_{ij} \tag{11.1}$$

f_{pres} being a scaling factor, p_i and p_j the pressure on cell i and j. $\boldsymbol{e}_{ij}$ is defined by $\frac{x_i - x_j}{|x_i - x_j|}$ with $p(i) > p(j)$.

Another mechanism which could be added to the cell dynamics is differential adhesion to the ECM. This can be implemented straightforward via a dependency of the cell-ECM friction on e.g. the cell cycle phase. A common assumption would be to "anchor" cells in certain phases in the ECM, restricting their motility. Intercellular shear forces could be implemented following the approach used in *Schaller* (2006).

Possible mechanisms which could increase the magnitude of the cell systems which can be modelled are of special interest. Coarse graining approaches may be implemented based on a "core freeze-out", reducing dynamics in the necrotic and quiescent regions

of the tumour. This is possible by making cells in long-time quiescence immovable, or through the introduction of a force threshold for movement of those cells. The Voronoi tessellation might offer further starting points for coarse graining. Freezing out whole regions of low dynamic, by keeping the corresponding voronoi boundary to tissue on a higher dynamic scale constant, could be a suitable approach.

The dynamics resulting from the modelling of cytotoxic substances from necrosis will also be of interest as a further mechanism, adding a new layer of self-interacting dynamics to the system. Cells surrouding necrotic regions are subject to die in an inflammation or due to cell lysis driven by the necrosis of their neighbours.

Furthermore, the diffusion coefficient should be made dependent on the spatial position to yield a more realistic diffusion of the solubles under consideration . Improvements in the simulation of surrounding tissue will also be of great interest, particularly in respect to the modelling of tumour invasion and metastasis.

11.3 Further investigations

The results within this thesis open up the possibility for a multitude of further investigations, including:

Invasion and metastasis Changed adhesion properties and other parameters such as synchronisation of the cell cycle progression have effects on the proliferation of the tumour. Furthermore the importance of the mechanism of tumour-fingering for invasion and metastasis should be investigated (see *Conde-Ramis et al.* (2008)).

Interaction with surrounding tissue The effects of pressure, and the surrounding tissue in general, on the tumour development should be studied in more detail (see *Anderson et al.* (2006), *Macklin and Lowengrub* (2007)).

Response to unfavourable conditions The combination of mechanisms which are responsible for induction of quiescence at the restriction point should be investigated. Are nutrient conditions or pressure-mediated contact inhibition the main reason for the rise of quiescence?

Importance of intracellular genetic networks Tumour suppressor genes (TSGs) and oncogenes have tremendous effects on the mechanisms available within cancerous cells (e.g. the blockage of the apoptotic pathway). With genetic networks the genetic characteristics of each tumour cell (e.g. its p53-gene-status) could be taken into consideration (see *Zhang et al.* (2007)).

Cell cycle re-synchronisation The influence of cell cycle re-synchronisation observed in response to irradiation has to be determined, which is related to the responsiveness of quiescent cells to changes in their environment. What is the general response of the cell cycle to irradiation (see *Hanin et al.* (2006))?

Relapse and excessive growth Tumour relapse upon irradiation could have effects on the optimal treatment procedures (see *Luk et al.* (1986)). A possible increase of nutrient diffusion through spongy tumour tissue should also be a target of further investigation.

Parameters for radiosusceptibility Cell response to irradiation depends on parameters such as the oxygen concentration within the tissue. The mechanisms involved should be implemented and analysed within the model system (see *Dewhirst et al.* (2008)).

This list of possible further investigations is not exhaustive. Taking into account that the layout of the developed code is, due to its generality, usable for the simulation of a wide variety of problems, further fields of investigation could be:

Human space exploration Astronauts are subject to high doses of cosmic background radiation (CBR) which involves high energy heavy ions, eventually leading to cancerogenesis. Shielding is partialy inefficient since it generates showers of slower carcenogenic particles. This process could be simulated with the help of GEANT4 (showering of CRB after passage through a compact shielding layer) with the aim of minimising the risk of cancer.

Acidity in tumour surroundings The cell metabolism is partialy variable due to the posibility of anaerobic combustion. This however may lead to the rise of a self-generated acidic surrounding of the tumour. Such a change in the environment will have effects on benigm tissue next to the tumour.

Effects of irradiation on the mitochondrial DNA (mtDNA) Damage to the mitochondrial DNA might have grave effects on the cell metabolism. This effects could open up new approaches to improve the efficiency of therapeutic irradiation.

Interaction with the immune system The complex interplay between the tumour and the immune system was neglected so far. However, the immune system might provide possible mechanisms for the tumour's destruction. Immuno-agents and the according interaction with cancerous cells could be integrated into the simulation.

Possible role for cancer stem cells The question whether or not cancer is a regulatory stem cell disease remains a hot topic in the scientific community. Malignant stem cells might play an important role in the development and treatment of cancer. Agent-based models can investigate the effect of a limited stem cell pool on the growth and treatment of the tumour.

Tumour vascularisation Attachment of the tumour to the blood and lymph system is a key in advanced tumour growth and metastasis. The induction of vascularisation through e.g. the VGEF-generation of tumour cells could be investigatied within the model.

Furthermore, the modelling of other tumour treatment approaches such as virotherapy or immunotherapy is feasible within the developed application. An interesting field might also be the modelling of combined therapies for cancer, provided the mechanism for both therapies are well understood within the model.

11.4 Onwards to irradiation modelling

Statistically, one person in two will get cancer throughout its life and one person in five will eventually die of cancer (see *Jemal et al.* (2007)). About half of all cancer patients receive radiation therapy at some point as a part of their treatment, with the cancer being curable in about half of these patients.

Therefore, radiation therapy (especially with heavy ions) should be the main target of further investigations, as any improvement to radiotherapy, even a small contribution, will benefit a great many people.

Acknowledgements

Numerous people have made this thesis possible and it is therefore impossible to mention them all. Nevertheless I will give it a try, starting with those people who contributed particularly to the scientific success.

First of all I would like to thank my advisors Dr. Michael Meyer-Hermann, for entrusting me with an important piece of research, and Prof. Dr. habil. Marcus Bleicher, for making a Diploma thesis inside an extern institution as FIAS possible without any problems. Both were excellent sources of advice in my hours of scientific need. My gratitude to Dr. Marc Thilo Figge for his introduction into the field of mathematical modelling of complex biological systems, which eventually lead me to work on this thesis.

Many thanks to Graziela Grise and Sophie Nahrwold for being brilliant office mates, and having the patience to do the painstaking proofreading of the thesis draft, thereby providing me with countless corrections and improvements.

Furthermore I would like to thank:

- The whole Systems Immunology Group at FIAS.
- Dr. Tilo Beyer for his advice on any programming problem at nearly all hours.
- Countless people at FIAS for their interest in my research and the arrising discussions which, quite often, enabled me to understand previously overlooked facts concerning my own research.
- FIAS itself for providing me with a great environment to do research and a nice corner office.
- The Center for Scientific Computing and the IT administration at FIAS for providing the computing power necessary for my simulations and solving all computer-related problems on short notice.
- All those people whom I forgot to mention.

Furthermore I would like to thank my family for their continuous support throughout my studies. Finally my apology and gratitude to all friends and loved ones who were uncared-for during the time I was occupied by the work on my thesis.

Abbreviations

Abbreviations and technical terms used within this thesis (not exhaustive)

MCTS	multicellular tumour spheroid
senecent	cell terminally in quiescence
quiescent	cell removed from the active cell cycle in a phase of “stasis”
oncogene	gene which can cause cancer upon deragulation
TSG	tumour suppressor gene
linac	linear accelerator
CT	computed tomography
MRI	magnetic resonance imaging
PET	positron emission tomography
XRT	external radiation therapy
BEV	beam’s eye view
MLC	multileaf collimator
3DCRT	3-Dimensional Conformal Radiotherapy
IMRT	Intensity-Modulated Radiation Therapy
IGRT	image-guided radiation therapy
ROS	reactive oxygen species
DNA	deoxyribonucleic acid
CDK	cyclin-dependent kinase
CDKC	cyclin-dependent kinase complex
MPF	mitosis promoting factor
TNF	tumour necrosis factor
TNFR	TNF receptor
CAC	Citric acid cycle
ATP	Adenosine triphosphate
ER	Endoplasmatic reticulum
ODE	ordinary differential equation
PDE	partial differential equation

Appendix

Mathematical model of tumour growth with the Gompertz function

The Gompertz function is a sigmoid function, where growth is slowest at the start and end of a time period. It can be used to model the growth of populations under bounded resources and has the typical form:

$$y(t) = ae^{be^{ct}} \tag{11.2}$$

where a is the upper asymptote, c is the growth rate, b, c are negative numbers, e is the Euler's Number. As its description suggests the Gompertz curve can be used to model the growth of tumours which was done first by A.K. Laird (see *Laird* (1964)).

Interestingly, the Gompertz model fits the growth processes of many populations, individuals, and even the growth of many avascular tumours remarkably well (see *Araujo and McElwain* (2004)).

Denoting the tumor size as $X(t)$ the Gompertz function can be written as:

Equation 12 (*Gompertz equation*)

$$X(t) = K \exp\left(\log\left(\frac{X(0)}{K}\right)\exp\left(-\alpha t\right)\right) \tag{11.3}$$

with $X(0)$ beeing the tumor size at the starting observation time, K is the carrying capacity, α is a constant related to the proliferative ability of the cells.

K denotes the maximum size that can be reached with the available nutrients. In fact it is:

$$\lim_{t\to+\infty} X(t) = K \tag{11.4}$$

independently on $X(0) \geq 0$. Note that, in absence of therapies, it is usually $X(0) \leq K$, whereas, in presence of therapies, it may be $X(0) \geq K$.

Even if mathematical modelling of growth curves is possible with certain success this does not enable the researcher to gain information about the spatial position of certain cells in the tumour. It remains a phenomenological approach to the problem under con-

sideration. There is a variety of processes inside of growing tumour which may only be captured correctly within an agent-based modelling approach.

Compton scattering

Compton scattering or the Compton effect is the decrease in energy (increase in wavelength) of an X-ray or gamma ray photon, when it interacts with matter. Inverse Compton scattering also exists, where the photon gains energy (decreasing in wavelength) upon interaction with matter. The amount the wavelength increases by is called the Compton shift.

The interaction between electrons and high energy photons results in the electron being given part of the energy (making it recoil), and a photon containing the remaining energy being emitted in a different direction from the original, so that the overall momentum of the system is conserved.

Equation 13 (*Compton scattering equation*)

$$\lambda' - \lambda = \frac{h}{m_e c}(1 - \cos\theta) \tag{11.5}$$

where λ is the wavelength of the photon before scattering, λ' is the wavelength of the photon after scattering, me is the mass of the electron, θ is the angle by which the photon's heading changes, h is Planck's constant, and c is the speed of light.

$\frac{h}{m_e c} = 2.43 \times 10^{-12}\, m$ is known as the Compton wavelength.

Amdahl's law

Amdahl's law, also known as Amdahl's argument, is named after computer architect Gene Amdahl, and is used to find the maximum expected improvement to an overall system when only part of the system is improved. It is often used in parallel computing to predict the theoretical maximum speedup using multiple processors.

In the case of parallelisation, Amdahl's law states that if P is the proportion of a program that can be made parallel (i.e. benefit from parallelization), and $(1 - P)$ is the proportion that cannot be parallelized (remains serial), then the maximum speedup that can be achieved by using N processors is

Definition 18 (*Amdahl's law*)

$$\frac{1}{(1 - P) + \frac{P}{N}} \tag{11.6}$$

In the limit, as N tends to infinity, the maximum speedup tends to $\frac{1}{(1-P)}$. In practice, performance per price falls rapidly as N is increased once there is even a small component of $(1 - P)$.

As an example, if P is 90%, then $(1 - P)$ is 10%, and the problem can be sped up by a maximum of a factor of 10, no matter how large the value of N used. For this reason, parallel computing is only useful for either small numbers of processors, or problems with very high values of P: so-called embarrassingly parallel problems. A great part of the craft of parallel programming consists of attempting to reduce $(1 - P)$ to the smallest possible value.

Triangulation of a vertex system and local interaction of according cell-agents is a good example of an embarrassingly parallel problem and can therefore benefit greatly from parallelisation

Copyright terms

Bibliography

Agarwal, M. L., Agarwal, A., Taylor, W. R., and Stark, G. R., 1995. p53 controls both the g2/m and the g1 cell cycle checkpoints and mediates reversible growth arrest in human fibroblasts. *Proc Natl Acad Sci U S A*, **92**(18):8493–8497.

Alberts, B., Johnson, A., Lewis, J., Raff, M., Roberts, K., and Walter, P. *Molecular Biology of the Cell, Fourth Edition*. Garland. URL `http://www.amazon.ca/exec/obidos/redirect?tag=citeulike09-20%&path=ASIN/0815332181`.

Anderson, A. R. A., 2005. A hybrid mathematical model of solid tumour invasion: the importance of cell adhesion. *Math Med Biol*, **22**(2):163–186. URL `http://imammb.oxfordjournals.org/cgi/content/abstract/22/2/163`.

Anderson, A. R. A., Weaver, A. M., Cummings, P. T., and Quaranta, V., 2006. Tumor morphology and phenotypic evolution driven by selective pressure from the microenvironment. *Cell*, **127**(5):905–915. doi:10.1016/j.cell.2006.09.042. URL `http://dx.doi.org/10.1016/j.cell.2006.09.042`.

Araujo, R. P. and McElwain, D. L. S., 2004. A history of the study of solid tumour growth: The contribution of mathematical modelling. *Bulletin of Mathematical Biology*, **66**:1039–1091.

Aurenhammer, F., 1987. Power diagram: properties, algorithms and applications. *SIAM J.*, **16**(1):78–96.

Baranov, V. I., Belichenko, V. M., and Shoshenko, C. A., 2000. Oxygen diffusion coefficient in isolated chicken red and white skeletal muscle fibers in ontogenesis. *Microvascular Research*, **60**(2):168–176.

Bauer, T., Motosugi, N., Miura, K., Sabe, H., and Hiiragi, T., 2008. Dynamic rearrangement of surface proteins is essential for cytokinesis. *Genesis*, **46**(3):152–162. doi:10.1002/dvg.20377. URL `http://dx.doi.org/10.1002/dvg.20377`.

Bausch, A. R., Moller, W., and Sackmann, E., 1999. Measurement of local viscoelasticity and forces in living cells by magnetic tweezers. *Biophys. J.*, **76**(1 Pt 1):573–9.

Bausch, A. R., Ziemann, F., Boulbitch, A. A., Jacobson, K., and Sackmann, E., 1998. Local measurements of viscoelastic parameters of adherent cell surfaces by magnetic bead microrheometry. *Biophys. J.*, **75**(4):2038–49.

Bell, H. S., Whittle, I. R., Walker, M., Leaver, H. A., and Wharton, S. B., 2001. The development of necrosis and apoptosis in glioma: Experimental findings using spheroid culture systems. *Neuropathology and Applied Neurobiology*, **27**:291–304.

Bethe, H., 1930. Zur theorie des durchgangs schneller korpuskularstrahlen durch materie. *Annalen der Physik*, **397**(3):325–400. URL `http://dx.doi.org/10.1002/andp.19303970303`.

Beyer, T., 2007. *Spatio-Temporal Dynamics of Primary Lymphoid Follicles During Organogenesis and Lymphneogenesis*. Ph.D. thesis, Johann Wolfgang Goethe-Universität, Frankfurt am Main.

Beyer, T. and Meyer-Hermann, M., 2007. Modeling emergent tissue organization involving high-speed migrating cells in a flow equilibrium. *preprint at http://arxiv.org/q-bio/0611057*.

Beyer, T., Meyer-Hermann, M., and Soff, G., 2002. A possible role of chemotaxis in germinal center formation. *Inter. Immunol.*, **14**(12):1369–81.

Beyer, T., Schaller, G., Deutsch, A., and Meyer-Hermann, M., 2005a. Parallel dynamic and kinetic regular triangulation in three dimensions. *Computer Physics Communications*, **172**(3):86–108.

Beyer, T., Schaller, G., Deutsch, A., and Meyer-Hermann, M., 2005b. Parallel dynamic and kinetic regular triangulation in three dimensions. *Comput. Phys. Commun.*, **172**(2):86–108.

Blakely, E. A., 1992. Cell inactivation by heavy charged particles. *Radiation and Environmental Biophysics*, **31**(3):181–196. URL `http://dx.doi.org/10.1007/BF01214826`.

Bohl, J., 2006. *Charakterisierung von zwei Glioblastomzelllinien zur Vorbereitung für die Tumortherapie mit schweren Ionen in Kombination mit Chemotherapie*. Master's thesis, Hochschule Darmstadt Fachbereich Chemie- und Biotechnologie.

Bronstein, I. N., Semendjajew, K. A., Musiol, G., and Mühlig, H., 1997. *Taschenbuch der Mathematik*. Harri Deutsch, Frankfurt am Main, Thun, 3rd edition.

Brown, J. M. and Attardi, L. D., 2005. The role of apoptosis in cancer development and treatment response. *Nat Rev Cancer*, **5**(3):231–237. doi:10.1038/nrc1560. URL `http://dx.doi.org/10.1038/nrc1560`.

Canadas, P., Laurent, V. M., Oddou, C., Isabey, D., and Wendling, S., 2002. A cellular tensegrity model to analyse the structural viscoelasticity of the cytoskeleton. *J. Theor. Biol.*, **218**(2):155–73.

Casciari, J. J., Sotirchos, S. V., and Sutherland, R. M., 1988. Glucose Diffusivity in Multicellular Tumor Spheroids. *Cancer Research*, **48**(14):3905–3909.

Casciari, J. J., Sotirchos, S. V., and Sutherland, R. M., 1992. Variations in tumor cell growth rates and metabolism with oxygen concentration, glucose concentration, and extracellular ph. *Journal of Cellular Physiology*, **151**(2):386–394. URL `http://dx.doi.org/10.1002/jcp.1041510220`.

Castorina, P., Deisboeck, T. S., Gabriele, P., and Guiot, C., 2007. Growth laws in cancer: implications for radiotherapy. *Radiat Res*, **168**(3):349–356. doi:10.1667/RR0787.1. URL `http://dx.doi.org/10.1667/RR0787.1`.

Chu, Y. S., Dufour, S., Thiery, J. P., Perez, E., and Pincet, F., 2005. Johnson-Kendall-Roberts theory applied to living cells. *Phys. Rev. Lett.*, **94**(2):028102.

Chu, Y.-S., Thomas, W. A., Eder, O., Pincet, F., Perez, E., Thiery, J. P., and Dufour, S., 2004. Force measurements in e-cadherin-mediated cell doublets reveal rapid adhesion strenghtened by actin cytoskeleton remodeling through rac and cdc42. *Journal of Cell Biology*, **167**(6):1183–1194.

Cinoni, P., Montani, C., Pereo, R., and Scopino, R. Parallel 3d delaunay triangulation. *citeseer.ist.psu.edu/512459.html*.

Conde-Ramis, I., Drasdo, D., Anderson, A. R., and Chaplain, M. A., 2008. Modelling the influence of the e-cadherin - beta-catenin pathway in cancer cell invasion: A multi-scale approach. *Biophys. J.*, p. biophysj.107.114678. URL k.

Cotran, R. S., K. V. and Robbins, S. L., 1994. *Pathologic Basis of Disease*. Saunders, Philadelphia, 5th ed. edition.

Dallon, J. C. and Othmer, H. G., 2004. How cellular movement determines the collective force generated by the Dictyostelium discoideum slug. *J. Theor. Biol.*, **231**(2):203–22.

Deutsch, A. and Dormann, S., 2003. *Cellular Automaton Modeling of Biological Pattern Formation*. Birkhäuser, Basel, 1st edition.

Dewhirst, M. W., Cao, Y., and Moeller, B., 2008. Cycling hypoxia and free radicals regulate angiogenesis and radiotherapy response. *Nat Rev Cancer*, **8**(6):425–437. URL http://dx.doi.org/10.1038/nrc2397.

Dingli, D. and Michor, F., 2006. Successful therapy must eradicate cancer stem cells. *Stem Cells*, **24**(12):2603–2610. doi:10.1634/stemcells.2006-0136. URL http://dx.doi.org/10.1634/stemcells.2006-0136.

Dingli, D., Traulsen, A., and Michor, F., 2007. (a)symmetric stem cell replication and cancer. *PLoS Comput Biol*, **3**(3):e53. doi:10.1371/journal.pcbi.0030053. URL http://dx.doi.org/10.1371%2Fjournal.pcbi.0030053.

Dionysiou, D. D., Stamatakos, G. S., Uzunoglu, N. K., Nikita, K. S., and Marioli, A., 2004. A four-dimensional simulation model of tumour response to radiotherapy in vivo: parametric validation considering radiosensitivity, genetic profile and fractionation. *J Theor Biol*, **230**(1):1–20. doi:10.1016/j.jtbi.2004.03.024. URL http://dx.doi.org/10.1016/j.jtbi.2004.03.024.

Dormann, S. and Deutsch, A., 2002. Modeling of self-organized avascular tumor growth with a hybrid cellular automaton. *In Silico Biology*, **2**(3):393–406.

Drasdo, D., 2003. *Polymer and cell dynamics: multiscale modeling and numerical simulations*, chapter On selected individual-based approaches to the dynamics in multicellular systems, pp. 169–204. Birkhäuser, Basel.

Drasdo, D., 2005. Coarse graining in simulated cell populations. *Advances in Complex Systems (ACS)*, **8**:319 – 363.

Drasdo, D. and Hohme, S., 2005. A single-cell-based model of tumor growth in vitro: monolayers and spheroids. *Physical Biology*, **2**(3):133–147. URL http://stacks.iop.org/1478-3975/2/133.

Drasdo, D., Kree, R., and McCaskill, J. S., 1995. Monte carlo approach to tissue-cell populations. *Phys. Rev. E*, **52**(6):6635–57.

Edelsbrunner, H. and Shah, N. R., 1996. Incremental topological flipping works for regular triangulations. *Algorithmica*, **15**(3):223–41.

Espey, D. K., Wu, X.-C., Swan, J., Wiggins, C., Jim, M. A., Ward, E., Wingo, P. A., Howe, H. L., Ries, L. A. G., Miller, B. A., Jemal, A., Ahmed, F., Cobb, N., Kaur, J. S., and Edwards, B. K., 2007. Annual report to the nation on the status of cancer, 1975-2004, featuring cancer in american indians and alaska natives. *Cancer*, **110**(10):2119–2152. URL `http://dx.doi.org/10.1002/cncr.23044`.

Ferrez, J.-A., 2001. *Dynamic triangulations for efficient 3D simulation of granular materials*. Ph.D. thesis, Ecole Polytechnique Federal de Lausanne.

Fletcher, D. A. and Theriot, J. A., 2004. An introduction to cell motility for the physical scientist. *Physical Biology*, **1**:T1–T10.

Forgacs, G., Foty, R. A., Shafrir, Y., and Steinberg, M. S., 1998. Viscoelastic properties of living embryonic tissues: a quantitative study. *Biophys. J.*, **74**(5):2227–34.

Freyer, J. P., 1998. Decreased mitochondrial function in quiescent cells isolated from multicellular tumor spheroids. *Journal of Cellular Physiology*, **176**(1):138–149. URL `http://dx.doi.org/10.1002/(SICI)1097-4652(199807)176:1<138::AID-JCP16>3.0.CO;2-3`.

Freyer, J. P. and Sutherland, R. M., 1985. A reduction in the in situ rates of oxygen and glucose consumption of cells in emt6/ro spheroids during growth. *J Cell Physiol*, **124**(3):516–524. doi: 10.1002/jcp.1041240323. URL `http://dx.doi.org/10.1002/jcp.1041240323`.

Freyer, J. P. and Sutherland, R. M., 1986. Regulation of growth saturation and development of necrosis in EMT6/Ro Multicellular Spheroids by the Glucose and Oxygen Supply. *Cancer Research*, **46**(7):3504–3512.

Galle, J., Aust, G., Schaller, G., Beyer, T., and Drasdo, D., 2005a. Individual cell-based models of the spatio-temporal organisation of multicellular systems – achievements and limitations. *submitted*.

Galle, J., Aust, G., Schaller, G., Beyer, T., and Drasdo, D., 2006. Individual cell-based models. *Cytometry Part A*, **69A**(7):704–710. URL `http://dx.doi.org/10.1002/cyto.a.20287`.

Galle, J., Loeffler, M., and Drasdo, D., 2005b. Modeling the Effect of Deregulated Proliferation and Apoptosis on the Growth Dynamics of Epithelial Cell Populations In Vitro. *Biophys. J.*, **88**(1):62–75. doi:10.1529/biophysj.104.041459. URL `http://www.biophysj.org/cgi/content/abstract/88/1/62`.

Galle, J., Loeffler, M., and Drasdo, D., 2005c. Modeling the effect of deregulated proliferation and apoptosis on the growth dynamics of epithelial cell populations in vitro. *Biophysical Journal*, **88**:62–75.

Gevertz, J. and Torquato, S., 2006. Modeling the effects of vasculature evolution on early brain tumor growth. *Journal of Theoretical Biology*, **243**(4):517–531.

Graner, F. and Glazier, J. A., 1992. Simulation of biological cell sorting using a two-dimensional extended potts model. *Phys. Rev. Lett.*, **69**(13):2013–. URL `http://link.aps.org/abstract/PRL/v69/p2013`.

Greenwade, G. D., 1993. The Comprehensive Tex Archive Network (CTAN). *TUGBoat*, **14**(3):342–351.

Grote, J., Susskind, R., and Vaupel, P., 1977. Oxygen diffusivity in tumor tissue (DS-carcinosarcoma) under temperature conditions within the range of 20–40 degrees C. *Pflugers Archiv - European Journal of Physiology*, **372**(1):37–42.

Grupen, C., 2000. Tumour Therapy with Particle Beams.

Guck, J., Ananthakrishnan, R., Mahmood, H., Moon, T. J., Cunningham, C. C., and Käs, J., 2001. The optical stretcher: A novel laser tool to micromanipulate cells. *Biophysical Journal*, **81**:767–784.

Hanahan, D. and Weinberg, R. A., 2000. The hallmarks of cancer. *Cell*, **100**(1):57–70.

Hanin, L., Hyrien, O., Bedford, J., and Yakovlev, A., 2006. A comprehensive stochastic model of irradiated cell populations in culture. *J Theor Biol*, **239**(4):401–416. doi:10.1016/j.jtbi.2005.08.006. URL `http://dx.doi.org/10.1016/j.jtbi.2005.08.006`.

Hategan, A., Law, R., Kahn, S., and Discher, D. E., 2003. Adhesively-tensed cell membranes: lysis kinetics and atomic force microscopy probing. *Biophys. J.*, **85**(4):2746–59.

Heidemann, S. R., Kaech, S., Buxbaum, R. E., and Matus, A., 1999. Direct observations of the mechanical behaviors of the cytoskeleton in living fibroblasts. *J. Cell Biol.*, **145**(1):109–22.

Helmlinger, G., Netti, P. A., Lichtenbeld, H. C., Melder, R. J., and Jain, R. K., 1997. Solid stress inhibits the growth of multicellular tumor spheroids. *Nature Biotechnology*, **15**:778–783.

Herbst, R. S., 2004. Review of epidermal growth factor receptor biology. *Int J Radiat Oncol Biol Phys*, **59**(2 Suppl):21–26. doi:10.1016/j.ijrobp.2003.11.041. URL `http://dx.doi.org/10.1016/j.ijrobp.2003.11.041`.

Hertz, H., 1882. Über die Berührung fester elastischer Körper. *Journal für die reine und angewandte Mathematik*, **92**:156–171.

Hilakivi-Clarke, L., Wang, C., Kalil, M., Riggins, R., and Pestell, R. G., 2004. Nutritional modulation of the cell cycle and breast cancer. *Endocr Relat Cancer*, **11**(4):603–622. doi:10.1677/erc.1.00665. URL `http://erc.endocrinology-journals.org/cgi/content/abstract/11/4/603`.

Hoffman, B. D., Massiera, G., Citters, K. M. V., and Crocker, J. C., 2006. The consensus mechanics of cultured mammalian cells. *Proc Natl Acad Sci U S A*, **103**(27):10259–10264. doi:10.1073/pnas.0510348103. URL `http://dx.doi.org/10.1073/pnas.0510348103`.

Honda, H., Tanemura, M., and Nagai, T., 2004. A three-dimensional vertex dynamics cell model of space-filling polyhedra simulating cell behavior in a cell aggregate. *J. Theor. Biol.*, **226**(4):439–53.

Huntly, B. J. P. and Gilliland, D. G., 2005. Cancer biology: Summing up cancer stem cells. *Nature*, **435**(7046):1169–1170. URL `http://dx.doi.org/10.1038/4351169a`.

Iozzo, R. V., 1998. Matrix proteoglycans: From molecular design to cellular function. *Annual Review of Biochemistry*, **67**(1):609–652. URL `http://arjournals.annualreviews.org/doi/abs/10.1146/annurev.biochem.67.1.609`.

Jemal, A., Murray, T., Ward, E., Samuels, A., Tiwari, R. C., Ghafoor, A., Feuer, E. J., and Thun, M. J., 2005. Cancer statistics, 2005. *CA Cancer J Clin*, **55**(1):10–30. URL `http://caonline.amcancersoc.org/cgi/content/abstract/55/1/10`.

Jemal, A., Siegel, R., Ward, E., Hao, Y., Xu, J., Murray, T., and Thun, M. J., 2008. Cancer Statistics, 2008. *CA Cancer J Clin*, **58**(2):71–96. doi:10.3322/CA.2007.0010. URL `http://caonline.amcancersoc.org/cgi/content/abstract/58/2/71`.

Jemal, A., Siegel, R., Ward, E., Murray, T., Xu, J., and Thun, M. J., 2007. Cancer Statistics, 2007. *CA Cancer J Clin*, **57**(1):43–66. doi:10.3322/canjclin.57.1.43. URL `http://caonline.amcancersoc.org/cgi/content/abstract/57/1/43`.

Jiang, Y., Pjesivac-Grbovic, J., Cantrell, C., and Freyer, J. P., 2005. A multiscale model for avascular tumor growth. *Biophys. J.*, **89**(6):3884–3894. URL `http://www.biophysj.org/cgi/content/abstract/89/6/3884`.

Johnson, K. L., Kendall, K., and Roberts, A. D., 1971. Surface energy and the contact of elastic solids. *Proceedings of the Royal Society of London A*, **324**(1558):301–313.

Kansal, A. R., Torquato, S., Harsh GR, I. V., Chiocca, E. A., and Deisboeck, T. S., 2000. Simulated brain tumor growth dynamics using a three-dimensional cellular automaton. *J. Theor. Biol.*, **203**(4):367–82.

Kirkpatrick, J. P., Brizel, D. M., and Dewhirst, M. W., 2003. A mathematical model of tumor oxygen and glucose mass transport and metabolism with complex reaction kinetics. *Radiation Research*, **159**(3):336–344. URL `http://dx.doi.org/10.1667%2F0033-7587%282003%29159%5B0336%3AAMMOTO%5D2.0.CO%3B2`.

Knuth, A., Jäger, D., and Jäger, E., 2000. Cancer immunotherapy in clinical oncology. *Cancer Chemotherapy and Pharmacology*, **46**(7):S46–S51. URL `http://www.springerlink.com/content/epfeg97uwutalh9l`.

Koo, Y.-E. L., Reddy, G. R., Bhojani, M., Schneider, R., Philbert, M. A., Rehemtulla, A., Ross, B. D., and Kopelman, R., 2006. Brain cancer diagnosis and therapy with nanoplatforms. *Advanced Drug Delivery Reviews*, **58**(14):1556–1577. URL `http://www.sciencedirect.com/science/article/B6T3R-4M0H8CB-3/2/e24994019269fafbe0545eb23f7088cf`.

Kraft, G., 2000. Tumor therapy with heavy charged particles. *Progress in Particle and Nuclear Physics*, **45**(Supplement 2):S473–S544. URL `http://www.sciencedirect.com/science/article/B6TJC-424M60R-5/1/06f1edadb024a49384bd5a90a8bb57ca`.

Kraft, G., Scholz, M., and Bechthold, U., 1999. Tumor therapy and track structure. *Radiation and Environmental Biophysics*, **38**(4):229–237. URL `http://dx.doi.org/10.1007/s004110050163`.

Krämer, M., Weyrather, W. K., and Scholz, M., 2003. The increased biological effectiveness of heavy charged particles: from radiobiology to treatment planning. *Technol Cancer Res Treat*, **2**(5):427–436.

Kunz-Schughart, L. A., Doetsch, J., Mueller-Klieser, W., and Groebe, K., 2000. Proliferative activity and tumorigenic conversion: Impact on cellular metabolism in 3-d culture. *American Journal of Physiology: Cell Physiology*, **278**:765–780.

Laird, A. K., 1964. Dynamics of tumor growth. *Br J Cancer*, **13**:490–502.

Landau, L. D. and Lifshitz, E. M., 1959. *Theory of Elasticity*. Pergamon Press, London.

Landry, J., Freyer, J. P., and Sutherland, R. M., 1981. Shedding of mitotic cells from the surface of multicell spheroids during growth. *Journal of Cellular Physiology*, **106**(1):23–32.

Landry, J., Freyer, J. P., and Sutherland, R. M., 1982. A model for the growth of multicellular spheroids. *Cell Tissue Kinetics*, **15**(6):585–594.

Lecuit, T. and Lenne, P.-F., 2007. Cell surface mechanics and the control of cell shape, tissue patterns and morphogenesis. *Nat Rev Mol Cell Biol*, **8**(8):633–644. URL `http://dx.doi.org/10.1038/nrm2222`.

Lo, C. F., 2007. Stochastic gompertz model of tumour cell growth. *J Theor Biol*, **248**(2):317–321. doi:10.1016/j.jtbi.2007.04.024. URL `http://dx.doi.org/10.1016/j.jtbi.2007.04.024`.

Luk, C. K., Keng, P. C., and Sutherland, R. M., 1986. Radiation response of proliferating and quiescent subpopulations isolated from multicellular spheroids. *Br J Cancer*, **54**(1):25–32.

Macklin, P. and Lowengrub, J., 2007. Nonlinear simulation of the effect of microenvironment on tumor growth. *J Theor Biol*, **245**(4):677–704. doi:10.1016/j.jtbi.2006.12.004. URL `http://dx.doi.org/10.1016/j.jtbi.2006.12.004`.

Mallet, D. and De Pillis, L., 2006. A cellular automata model of tumor-immune system interactions. *Journal of Theoretical Biology*, **239**(3):334–350. URL `http://www.sciencedirect.com/science/article/B6WMD-4H40J47-1/1/d2b9e49799a9a8b0a2aac8ad77ffb79a`.

Maniotis, A. J., Chen, C. S., and Ingber, D. E., 1997. Demonstration of mechanical connections between integrins, cytoskeletal filaments, and nucleoplasm that stabilize nuclear structure. *Proceedings of the National Academy of Sciences USA*, **94**:849–854.

Meineke, F. A., Potten, C. S., and Loeffler, M., 2001. Cell migration and organization in the intestinal crypt using a lattice-free model. *Cell Prolif.*, **34**(4):253–66.

Michor, F., Iwasa, Y., and Nowak, M. A., 2004. Dynamics of cancer progression. *Nat Rev Cancer*, **4**(3):197–205. URL `http://dx.doi.org/10.1038/nrc1295`.

Mielke, M. E., Rosen, H., Brocke, S., Peters, C., and Hahn, H., 1992. Protective immunity and granuloma formation are mediated by two distinct tumor necrosis factor alpha- and gamma interferon-dependent t cell-phagocyte interactions in murine listeriosis: dissociation on the basis of phagocyte adhesion mechanisms. *Infect Immun*, **60**(5):1875–1882.

Morgan, D., 2007. *The Cell Cycle: Principles of Control*. New Science Press: London.

Mücke, E. P., 1998. A Robust Implementation for three-dimensional Delaunay Triangulations. *International Journal of Computational Geometry and Applications*, **8**(2):255–76.

Murphy, K., 2007. *IMMUNOBIOLOGY 7 PB (Janeway's Immunobiology) (Immunobiology: The Immune System (Janeway))*. Garland Science. URL `http://www.amazon.ca/exec/obidos/redirect?tag=citeulike09-20%&path=ASIN/0815341237`.

Murray, J. D., 2002a. *Mathematical Biology I*, volume 17 of *Interdisciplinary Applied Mathematics*. Springer, Berlin Heidelberg, 3rd edition.

Murray, J. D., 2002b. *Mathematical Biology II*, volume 17 of *Interdisciplinary Applied Mathematics*. Springer, Berlin Heidelberg, 3rd edition.

Nass, M. M. and Nass, S., 1963. Intramitochondrial fibers with dna characteristics. i. fixation and electron staining reactions. *J Cell Biol*, **19**:593–611.

Neto, J. C., Agero, U., Gazzinelli, R. T., and Mesquita, O. N., 2006. Measuring optical and mechanical properties of a living cell with defocusing microscopy. *Biophys J*, **91**(3):1108–1115. doi:10.1529/biophysj.105.073783. URL `http://dx.doi.org/10.1529/biophysj.105.073783`.

Okabe, A., Boots, B., Sugihara, K., and Chiu, S. N., 2000. *Spatial tessellations: Concepts and applications of Voronoi diagrams*. Probability and Statistics. Wiley, NYC, $2^n d$ edition.

Palsson, E., 2001. A three-dimensional model of cell movement in multicellular systems. *Future Gen. Comp. Sys.*, **17**:835–852.

Press, W. H., Teukolsky, S. A., Vetterling, W. T., and Flannery, B. P., 1994. *Numerical Recipes in C*. Cambridge University Press, 2nd edition.

Pshenichnov, I., Larionov, A., Mishustin, I., and Greiner, W., 2007. Pet monitoring of cancer therapy with 3he and 12c beams: a study with the geant4 toolkit. *Phys Med Biol*, **52**(24):7295–7312. doi:10.1088/0031-9155/52/24/007. URL `http://dx.doi.org/10.1088/0031-9155/52/24/007`.

Pshenichnov, I., Mishustin, I., and Greiner, W., 2005. Neutrons from fragmentation of light nuclei in tissue-like media: a study with the geant4 toolkit. *Physics in Medicine and Biology*, (23):5493. URL `http://stacks.iop.org/0031-9155/50/5493`.

Pshenichnov, I., Mishustin, I., and Greiner, W., 2006. Distributions of positron-emitting nuclei in proton and carbon-ion therapy studied with geant4. *Physics in Medicine and Biology*, (23):6099. URL `http://stacks.iop.org/0031-9155/51/6099`.

Ribba, B., Saut, O., Colin, T., Bresch, D., Grenier, E., and Boissel, J. P., 2006. A multiscale mathematical model of avascular tumor growth to investigate the therapeutic benefit of anti-invasive agents. *J Theor Biol*, **243**(4):532–541. doi:10.1016/j.jtbi.2006.07.013. URL `http://dx.doi.org/10.1016/j.jtbi.2006.07.013`.

Rofstad, E. K., Eide, K., Skøyum, R., Hystad, M. E., and Lyng, H., 1996. Apoptosis, energy metabolism, and fraction of radiobiologically hypoxic cells: A study of human melanoma multicellular spheroids. *International Journal of Radiation Biology*, **70**(3):241–249.

Roose, T., Chapman, S. J., and Maini, P. K., 2007. Mathematical models of avascular tumor growth. *SIAM Rev.*, **49**(2):179–208.

Schaller, G., 2006. *On selected numerical approaches to Cellular Tissue*. Ph.D. thesis, Johann Wolfgang Goethe-University Frankfurt Main.

Schaller, G. and Meyer-Hermann, M., 2004. Kinetic and dynamic delaunay tetrahedralizations in three dimensions. *Computer Physics Communications*, **162**:9–23.

Schaller, G. and Meyer-Hermann, M., 2005a. Continuum versus Discrete model: A comparison for multicellular tumour spheroids. *to appear in Philosophical Transactions of the Royal Society Series A*.

Schaller, G. and Meyer-Hermann, M., 2005b. Epidermal homeostasis control in an off-lattice agent-based model. *arXiv*, p. physics/0507059.

Schaller, G. and Meyer-Hermann, M., 2005c. Multicellular tumor spheroid in an off-lattice Voronoi/Delaunay cell model. *Physical Review E*, **71**:051910–16.

Schardt, D. and The Heavy-Ion Therapy Collaboration, 2007. Tumor therapy with high-energy carbon ion beams. *Nuclear Physics A*, **787**:633–641. doi:10.1016/j.nuclphysa.2006.12.097.

Scholz, M. and Kraft, G., 1996. Track structure and the calculation of biological effects of heavy charged particles. *Adv Space Res*, **18**(1-2):5–14.

Schulz-Ertner, D., A. . N. C. . T. T. . H. O. . J. C. . K. G. . K. M. . W. J. . D., 2004. Results of carbon ion radiotherapy in 152 patients. *International Journal of Radiation OncologyBiologyPhysics*, **58**:631 – 640.

Schulz-Ertner, D. A . Nikoghosyan, H. . H. B. . D. S. . C. O. . J. C. . K. L. . E. J. . D., 2007. Carbon ion radiotherapy of skull base chondrosarcomas. *International Journal of Radiation OncologyBiologyPhysics*, **67**:171 – 177.

Stamatakos, G. S., Antipas, V. P., Uzunoglu, N. K., and Dale, R. G., 2006. A four-dimensional computer simulation model of the in vivo response to radiotherapy of glioblastoma multiforme: studies on the effect of clonogenic cell density. *Br J Radiol*, **79**(941):389–400. doi:10.1259/bjr/30604050. URL `http://dx.doi.org/10.1259/bjr/30604050`.

Sulić, S., Panić, L., Dikić, I., and Volarević, S., 2005. Deregulation of cell growth and malignant transformation. *Croat Med J*, **46**(4):622–638.

Surdutovich, E., Obolensky, O. I., Scifoni, E., Pshenichnov, I., Mishustin, I., Solov'yov, A. V., and Greiner, W., 2008. Ion-induced electron production in tissue-like media and dna damage mechanisms. URL `http://www.citebase.org/abstract?id=oai:arXiv.org:0807.0786`.

Taylor, W. R., DePrimo, S. E., Agarwal, A., Agarwal, M. L., Schönthal, A. H., Katula, K. S., and Stark, G. R., 1999. Mechanisms of g2 arrest in response to overexpression of p53. *Mol Biol Cell*, **10**(11):3607–3622.

Townes, P. L. and Holtfreter, J., 1955. Directed movements and selective adhesion of embryonic amphibian cells. *Journal of Experimental Zoology*, **128**(1):53–120. URL `http://dx.doi.org/10.1002/jez.1401280105`.

Turner, S., 2005. Using cell potential energy to model the dynamics of adhesive biological cells. *Phys. Rev. E*, **71**(4):041903–12. URL `http://link.aps.org/abstract/PRE/v71/e041903`.

Turner, S., Sherratt, J. A., Painter, K. J., and Savill, N. J., 2004. From a discrete to a continuous model of biological cell movement. *Phys. Rev. E*, **69**(2):021910–. URL `http://link.aps.org/abstract/PRE/v69/e021910`.

Wakeford, R., 2004. The cancer epidemiology of radiation. *Oncogene*, **23**(38):6404–6428. doi: 10.1038/sj.onc.1207896. URL http://dx.doi.org/10.1038/sj.onc.1207896.

Ward, J. P. and King, J. R., 1997. Mathematical modelling of avascular-tumour growth. *Math Med Biol*, **14**(1):39–69. URL http://imammb.oxfordjournals.org/cgi/content/abstract/14/1/39.

Ward, J. P. and King, J. R., 1999. Mathematical modelling of avascular-tumour growth ii: Modelling growth saturation. *Math Med Biol*, **16**(2):171–211. URL http://imammb.oxfordjournals.org/cgi/content/abstract/16/2/171.

Wehrle, J. P., Ng, C. E., McGovern, K. A., Aiken, N. R., Shungu, D. C., Chance, E. M., and Glickson, J. D., 2000. Metabolism of alternative substrates and the bioenergetic status of emt6 tumor cell spheroids. *NMR in Biomedicine*, **13**(6):349–360. URL http://dx.doi.org/10.1002/1099-1492(200010)13:6<349::AID-NBM652>3.0.CO;2-X.

Wiesner, R. J., Rüegg, J. C., and Morano, I., 1992. Counting target molecules by exponential polymerase chain reaction: copy number of mitochondrial dna in rat tissues. *Biochem Biophys Res Commun*, **183**(2):553–559.

Wright, W. E. and Shay, J. W., 2000. Telomere dynamics in cancer progression and prevention: fundamental differences in human and mouse telomere biology. *Nat Med*, **6**(8):849–851. URL http://dx.doi.org/10.1038/78592.

Yang, F., 2003. Load-displacement relation in adhesion measurement. *J. Phys. D*, **36**(19):2417–20.

Zacharaki, E. I., Stamatakos, G. S., Nikita, K. S., and Uzunoglu, N. K., 2004. Simulating growth dynamics and radiation response of avascular tumour spheroids – model validation in the case of an EMT6/Ro multicellular spheroid. *Computer Methods and Programs in Biomedicine*, **76**:193–206.

Zhang, H. and Liu, K.-K., 2008. Optical tweezers for single cells. *J R Soc Interface*, **5**(24):671–690. doi:10.1098/rsif.2008.0052. URL http://dx.doi.org/10.1098/rsif.2008.0052.

Zhang, L., Athale, C. A., and Deisboeck, T. S., 2007. Development of a three-dimensional multiscale agent-based tumor model: simulating gene-protein interaction profiles, cell phenotypes and multicellular patterns in brain cancer. *J Theor Biol*, **244**(1):96–107. doi:10.1016/j.jtbi.2006.06.034. URL http://dx.doi.org/10.1016/j.jtbi.2006.06.034.